Tuning Thiol-Functionalized Nanosized Metal–Organic Frameworks for Applications in Ophthalmic Drug Delivery

Samantha Prelaz

A Thesis in

The Department of

Chemistry and Biochemistry

Presented in Partial Fulfillment of the Requirements for

The Degree of Master of Science (Chemistry) at

Concordia University

Montréal, Quebec, Canada

August 2023

CONCORDIA UNIVERSITY

SCHOOL OF GRADUATE STUDIES

This is to certify that the thesis prepared

By: Samantha Prelaz

Entitled: Tuning Thiol-Functionalized Nanosized Metal–Organic Frameworks for Applications in Ophthalmic Drug Delivery

and submitted in partial fulfillment of the requirements for the degree of

Master of Science (Chemistry)

complies with the regulations of the University and meets the accepted standards with respect to originality and quality.

Signed by the final Examining Committee:

Dr. Brandon Findlay_____Chair

Dr. Marek B. Majewski_____Examiner

Dr. Rafik Naccache_____Examiner

Dr. Ashlee J. Howarth_____Supervisor

Approved by _____

Dr. Louis Cuccia, Graduate Program Director, Chemistry and Biochemistry 2023

_____2023 _____

Dr. Pascale Sicotte, Dean, Faculty of Arts and Science

Abstract

Tuning Thiol-Functionalized Nanosized Metal–Organic Frameworks for Applications in Ophthalmic Drug Delivery

Samantha Prelaz

The work described herein explores the synthesis and characterization of porous, crystalline materials known as metal–organic frameworks (MOFs) – comprised of metal nodes bridged by multitopic organic linkers. Owing to their high modularity, tunable pore shapes and sizes, and high surface areas, they are promising drug vectors for applications in drug delivery. Chapters 2 and 3 delve into the different approaches for applying MOFs in ophthalmic drug delivery applications.

Chapter 2 explores the design and synthesis of nanosized MOFs including MOF-808, UiO-66, and UiO-67. The synthesis and characterization of the nanoMOFs is described and the nanoMOFs are subject to post-synthetic modification with thiolated ligands to study the potential for mucoadhesive properties in these materials towards drug delivery applications. A series of characterization techniques, including probing the mucoadhesion, are presented with the goal of understanding how the nanoscale size and thiol-functionalization can affect the mucoadhesive properties of MOFs.

Chapter 3 looks into the synthesis and characterization of a series of nanosized thiol-functionalized MOFs with mixed linkers. A series of UiO-66 analogues comprised of increasing concentrations of 2,5-dimercaptoterepthalic acid (BDC-$(SH)_2$) is synthesized mixed with the standard UiO-66 linker, 1,4-benzenedicarboxylic acid (BDC). The mixed-linker MOFs are characterized with the goal of understanding how increasing incorporation of BDC-$(SH)_2$ affects the surface area, mucoadhesive properties and potential drug delivery capacity of these materials.

Acknowledgements

I would like to start off by thanking my supervisor, Dr. Ashlee Howarth, for giving me this opportunity to learn, grow and fulfill all my science achievements. Thank you for being patient, dedicated and knowledgeable in the field of MOFs. From the first ever time I attended your Inorganic I course during undergrad, I knew that I wanted to continue my science studies alongside you as my mentor. I appreciate all your positivity and constructive feedback on both my projects and it truly reflects how much I've become more confident and skilled. I can't thank you enough for this amazing experience I will cherish.

To my committee members, Dr. Marek Majewski and Dr Rafik Naccache, I would like to thank you both for your support and guidance during my studies. I appreciate all our fruitful discussions and insight on topics regarding my project. You have both made me realize and learn so many new concepts, theories and applications – thank you!

To my lab colleagues in the Howarth group, I am grateful for our friendships, collaborations, and amazing times experienced together – thank you for making my years in the Howarth group so enjoyable and memorable. Victor – you are such a kind soul with a big heart, always in an optimistic mindset and willing to help in any way. I appreciate all the times I requested advice and assistance, you were always ready to lend your time and patience. We have come a long way since you supervised me for my CHEM 419 project during undergrad and I have learned so much from you. Chris – for being the life of the party and DRIFTS go-to, thank you for always helping me out and making me laugh with your endless jokes. Ximena – thank you for being so sweet, supportive and a great friend to start our Master's together. Hudson – thank you for all your kindness, patience and knowledge in the field of drug delivery. Rafa – you are always there to lend a helping hand, so thoughtful and so informed with crystallography, I appreciate all your insight. Lavinia – thank you for being a ray of sunshine and always motivating me when I was at my lowest. Laure-Anne – for being friendly and kind. Clara – who I've known for only a short period, you have been so sweet and amazing to work with. Lars – for being a great TA partner and office neighbor, thank you for all the laughs and amazing times. Amna – thank you for being so encouraging, lifting up everyone's spirits and for what is now my lab name "Mantha girl". Paola – thank you for your patience, kindness and unwavering support and mentorship in guiding me

through my project, I appreciate all your dedication and hard work you have put into initiating our project, I couldn't have done it without you. Zvart – thank you for being so cool, awesome, and guiding me as I was integrating into the lab.

I would like to thank the Majewski group whom we've shared special moments together and made the lab setting such a fun working environment. I would like to give a special thank you to Victoria – our special bond and friendship will always be cherished. I will forever be grateful of our journey together during our grad studies, your support, our endless laughs, and our special lunch times. Thank you for being a great friend through it all.

Thank you to our collaborators – Élodie, Gabrielle and Cloé, you have truly been amazing to work with, I have learned so much about my project and am thankful for this opportunity to have worked on a really interesting application with MOFs.

Thank you to our technical staff at Concordia – Costa, Nooshin, Vincent, Mihai, Marika, Heng, Neema for your assistance and support along the way. To Jenn, thank you for being so helpful and sweet.

To the graduate student community at Concordia, thank you for all your support.

To Kevin – thank you for always being there for me, being my # 1 fan and encouraging me along the way. You truly always know how to make me smile and make me believe in myself, that with confidence and devotion, I can achieve anything I set my mind to.

To my parents – thank you for being my supporters, for being curious about my days in the lab and trying to understand what I research, I could have not done this without you both. I know I made you both proud parents. To my brother and Jessica – thank you for your motivation and encouragement. To Campo – my dog who has been with me every step of the way, watching me write, study and rehearse my presentations. To my grandparents, aunts, uncles and cousins, and close family friends, I appreciate all your endless support and I am forever grateful.

Dedication

To my family – Mom, Dad, Brother and Campo

To my partner – Kevin

Contribution of Authors

In all chapters, Dr. Ashlee J. Howarth acted in a supervisory role. Chapters 2 and 3 involved a collaboration with Dr. Élodie Boisselier, Gabrielle Raiche-Marcoux, and Cloé Maranda from the Department of Ophthalmology at Université de Laval in Quebec City, Canada.

Chapter 2 is an inter-institutional collaborative project in which I am the primary author of this work. Paola Marino initiated the first step of this research and shared procedures and protocols pertaining to the synthesis of micron sized UiO-66 and UiO-67 MOFs, and the Ellman's test by UV–Vis spectroscopy. Nooshin Movahed from the Centre for NanoScience Research facility assisted with sample preparation and collecting SEM and TEM data for all samples. Constantin Yannopoulos from the Department of Chemistry & Biochemistry at Concordia University performed the ^{1}H-NMR spectroscopy analysis for all samples. Chris Copeman assisted with the sample preparation and collection of all DRIFTS data. Gabrielle Raiche-Marcoux and Cloé Maranda performed the mucoadhesion experiments using PAS coloration and fluorescence spectroscopy.

Chapter 3 is an inter-institutional collaborative project in which I am the primary author of this work. Cloé Maranda performed the mucoadhesive experiments using PAS coloration and fluorescence spectroscopy.

Table of Contents

LIST OF FIGURES

List of Tables

List of Abbreviations

^{1}H-NMR	proton nuclear magnetic resonance spectroscopy
BET	Brunauer-Emmett-Teller
BSD	back-scattered electron detector
CCDC	Cambridge Crystallographic Data Centre
$CDCl_3$	chloroform
D	translational diffusion coefficient
D_2O	deuterium oxide
D_2SO_4	deuterated sulfuric acid
DEF	*N,N*-diethylformamide
DLS	dynamic light scattering
DMA	*N,N*-dimethylacetamide
DMF	*N,N*-dimethylformamide
DMSO-d_6	deuterated dimethyl sulfoxide
DRIFTS	diffuse reflectance infrared Fourier transform spectroscopy
DTNB	5,5'-dithiobis-(2-nitrobenzoic acid)
EDS	energy dispersive X-ray spectroscopy
EELS	electron energy loss spectroscopy
fcu	face-centered cubic topology
H_2BDC	1,4-benzenedicarboxylic acid
H_2BPDC	biphenyl-4,4'-dicarboxylic acid
H_2SO_4	sulfuric acid
H_3BTC	1,3,5-benzenetricarboxylic acid
HCl	hydrochloric acid
IUPAC	International Union of Pure and Applied Chemistry

KBr	potassium bromide
MOF	metal–organic framework
NaOD	sodium deuteroxide
NLDFT	non-local density functional theory
NSAID	non-steroidal anti-inflammatory drug
OMS	open-metal sites
PAS	Period Acid–Schiff
PCS	photon correlation spectroscopy
pcu	primitive cubic topology
PDI	polydispersity index
PEG	polyethylene glycol
PSM	post-synthetic modification
PXRD	powder X-ray diffraction
RCSR	Reticular Chemistry Structure Resource
SALE	solvent-assisted ligand exchange
SALI	solvent-assisted ligand incorporation
SBU	secondary building unit
$scCO_2$	supercritical carbon dioxide
SED	secondary electron detector
SEM	scanning electron microscopy
spn	spinel topology
ssNMR	solid-state nuclear magnetic resonance spectroscopy
STEM	scanning transmission electron microscopy
TEM	transmission electron microscopy
TNB	2-nitro-5-thiobenzoic acid

UiO	University of Oslo
UV–Vis	ultraviolet–visible spectroscopy
UV–Vis DRS	ultraviolet–visible diffuse reflectance spectroscopy

Chapter 1

Introduction

1.1. History and Definition of Metal–Organic Frameworks

Coordination compounds, first introduced by Alfred Warner in the late 19th century, are structures involving bonding between ligands and a central metal ion - the foundation for studies of coordination chemistry.[1] Later advancements in coordination chemistry gave rise to coordination polymers in the early 1960's, defined as metal ions connected to bridging ligands.[2] Metal–organic frameworks abbreviated as MOFs (Figure 1.1), have emerged during the past 30 years in the field of inorganic chemistry. Some of the earliest work reported in 1965 from Tomic showcases the synthesis of coordination polymers differing in metal ions and di-, tri-, and tetratopic carboxylic acid-based linkers, with the resulting materials investigated for thermal stability.[3] In the early 1990's, preliminary work from Hoskins and Robson reported scaffolding-like materials with potential cavities that are accessible, demonstrating the possibility and prospect of this work in the growing field of MOFs.[4] Additional understanding of MOFs structures and synthesis was detailed by Yaghi in an ever-growing field known as reticular chemistry. This field explores diverse approaches to connecting molecular components using coordination bonds. This work also investigates the structural porosity of MOFs, granting them the ability to enclose guest molecules.[5, 6] The first ever named metal–organic framework, MOF-5, showcases the universal design and synthesis of a stable yet crystalline MOF with permanent porosity as confirmed by crystal structure and gas sorption experiments.[7]

MOFs are often referred to as coordination networks, a subclass of coordination solids described as 2D and 3D coordination polymers.[8] The International Union of Pure and Applied Chemistry (IUPAC) states that MOFs are 3D coordination networks containing organic ligands with potential voids and long-range order (crystalline)[9] and that MOFs can also be 2D with short-range order (amorphous).[9] However, what distinguishes MOFs from coordination polymers and coordination networks is the presence of potential voids in the overall structure.[9] Owing to their seemingly endless combination of building units, MOFs are characterized by their high structural tunability. These materials are composed of inorganic metal nodes, that can be in the form of clusters, ions or chains,[10] which are bridged together by multitopic linkers, often containing nitrogen and oxygen.[11] The individual cluster entities that are formed when the metal node is

surrounded by linkers are referred to as secondary building units (SBU)s and have defined geometries.[12] Depending on the metal and ligand chosen, the connectivity and stability of the framework will be influenced, with high-valent metal cations requiring more coordinating linkers and ligands to balance the overall charge.[10] The key features of these materials are the ability to tune the identity and functionality of the building blocks to achieve defined porosity, surface area and stability. Owing to the variety of metals and organic linkers that can be combined, the design and structure of MOFs is highly diverse. MOFs continue to be studied as emerging materials in many different applications including gas storage and release,[13–15] drug delivery,[16, 17] catalysis,[18–20] removal of contaminants from wastewater,[21–23] and degradation of chemical warfare agents to name a few.[24, 25]

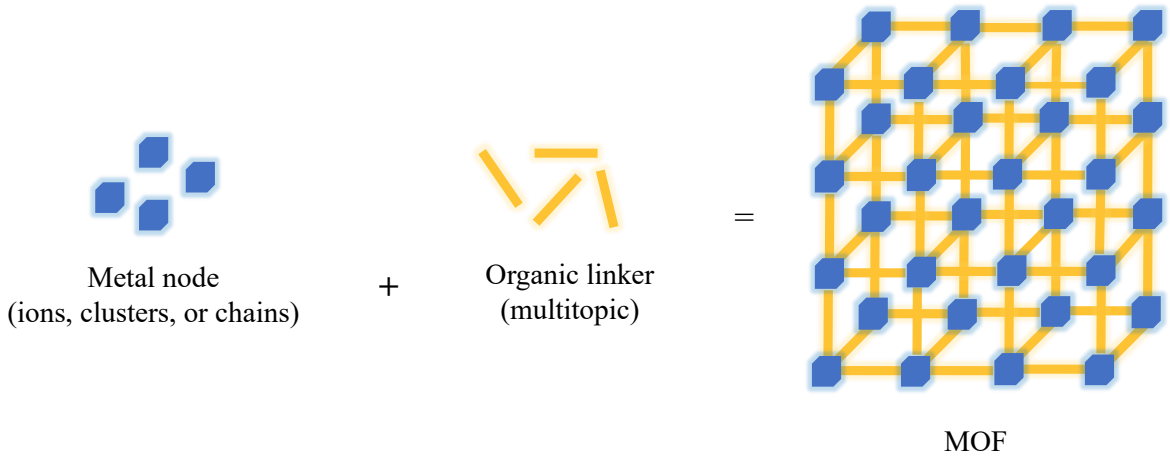

Figure 1.1. Periodic construction of a metal–organic framework (MOF).

1.2. Fundamental Principles of MOFs

The synthesis of MOFs has attracted much attention over the years due to their vast tunability and potential for many applications. The properties of MOF building blocks including coordination geometry of the metal node and its connectivity with the linker are factors that directly contribute to the overall structure and characteristics of MOFs.[26]

1.2.1. Reticular Chemistry

The chemistry of network structures by linking molecular building units together through strong bonding to form an extended porous assembly is referred to as reticular chemistry.[9] The approach was first introduced by MOF researchers, Yaghi, and O'Keeffe, who addressed the

importance of stable, yet defined SBUs that maintain their overall stability to direct the synthesis and design of predetermined structures and compositions.[27]

1.2.2. Topology

The network structure of a MOF and its connectivity are the basis to understanding the overall topology. What makes up the topology of a MOF are the metal nodes, which often represent the vertices of a net, and the multitopic linkers that often represent the edges of a net.[26] Predicting the topology of a MOF is not always straightforward due to the number of possible varieties of coordination geometries and interconnectivities that can occur within different building blocks.[26] Several reaction parameters influence the network structure of a MOF such as solvent, temperature, and pH, giving rise to endless possibilities for topologically different vertices and edges.[26] The topology is designated with a code represented by three bolded letters (i.e., **fcu** face-centered cubic, Figure 1.2) and can be accessed in the Reticular Chemistry Structure Resource (RCSR) database.[28]

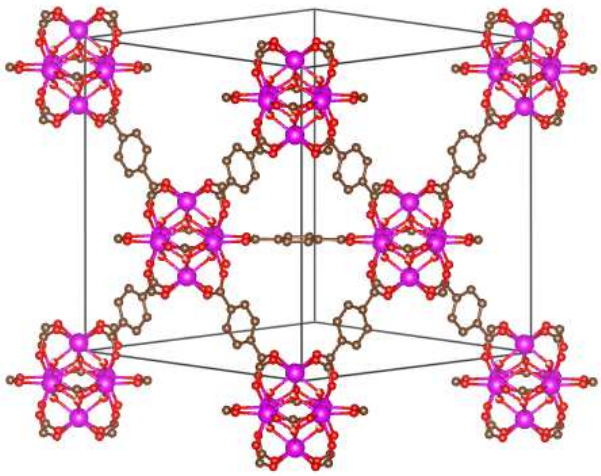

Figure 1.2. Representation of a MOF with **fcu** topology, showing the extended unit cell of UiO-66; Zr_6-based metal cluster (magenta), oxygen (red), and carbon (brown).

1.2.3. Open-metal sites in MOFs

Open-metal sites (OMS) are defined as unsaturated coordination sites on metal ions or coordination sites that have labile terminal ligands that can be easily substituted.[29] A Cu-based MOF, HKUST-1, was first reported in 1999 by Chui *et al.* having a defined open-framework with easily obtainable OMS.[30] The initial stable coordination geometry of a MOF node often consists

of structural organic linkers as well as coordinated solvent molecules or modulators from the reaction.[29] OMS can be achieved by the removal of labile terminal ligands (Figure 1.3), such as a solvent molecules and modulators that are initially coordinated to a metal node, and removed during activation with acid or under heat and vacuum.[29] When generating OMS in MOFs, it is crucial to ensure that the overall structure does not collapse.[29] OMS can increase surface area, interactions with guest molecules, and catalytic activity.[29]

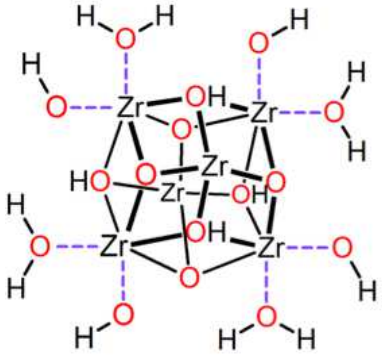

Figure 1.3. Representation of labile terminal ligands that can be removed and generate coordinatively unsaturated open-metal sites in MOFs.

1.2.4. Postsynthetic Modification of MOFs

A key approach in the advancement of MOFs that was first suggested by Hoskins and Robson in 1990 and later introduced by Cohen, is postsynthetic modification (PSM). It is a concept that was developed in the field to introduce functionality to MOFs after they have been synthesized.[31] The potential advantages that can be offered by PSM include a diverse range of functional groups that can be added onto an existing MOF structure, and the control of the degree of modification to systematically tune MOF properties.[32, 33] Additionally, PSM can be advantageous to obtain MOFs that are difficult to synthesize *de novo* and various PSM methods can be implemented including solvent-assisted ligand incorporation (SALI)[34] through functionalization of the metal cluster and solvent-assisted-linker exchange (SALE)[35] allowing for the incorporation of new linkers into a MOF network having the same topology as the parent MOF.[36]

With much recent work on using SALI with Zr-based MOFs, the technique has attracted much attention. SALI works by functionalizing the OMS on a metal node with charge

compensating functional groups to introduce a wide variety of modularity to synthetic MOF structures.[37] The earliest works of SALI were first demonstrated by Deria *et al.* using the Zr-based MOF NU-1000, which involves replacing terminal -OH and -OH_2 ligands on neighbouring metal sites with an incoming ligand bearing a carboxylate (-COOH) functional group.[38, 39] The interaction is based on acid-base chemistry between the terminal hydroxyl groups or aqua moieties on the metal center and the incoming ligand bearing a charge compensating functional group, thereby not replacing any bridging hydroxyl groups from the metal cluster.[34, 37, 40] The general conditions favouring the accessibility of the metal cluster with the incoming ligand require mild heating and short reaction times with occasional swirling (Figure 1.4).[38, 41]

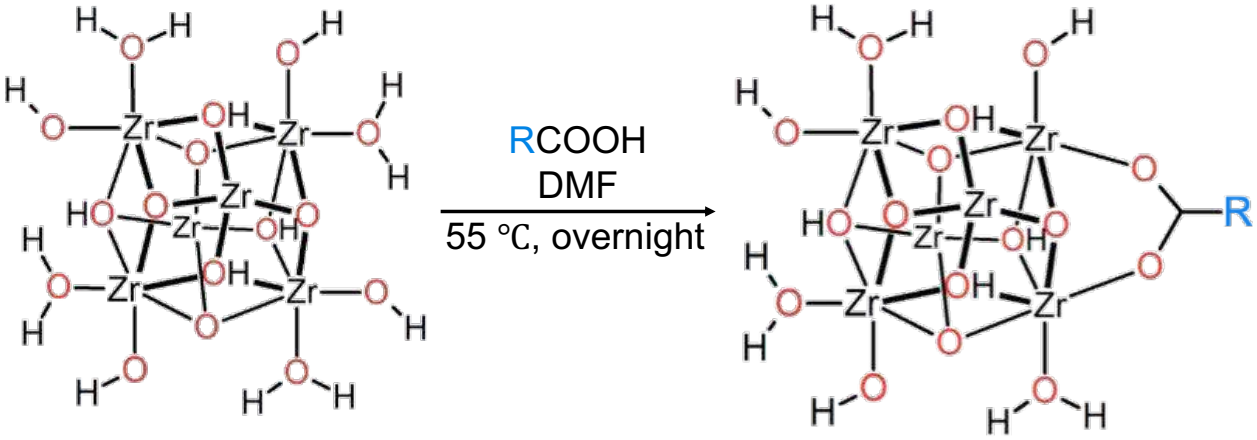

Figure 1.4. Schematic of solvent-assisted ligand incorporation (SALI) on a Zr_6-cluster node.

1.3. Characteristics and Properties of Zr-based MOFs

As one of the most widely studied and largest families of MOFs, Zr-based MOFs are promising materials for a wide array of applications. Owing to their intrinsic characteristics such as the high coordination number of Zr(IV) ions, they can form strong metal–linker bonds with carboxylate oxygen atoms.[42] In addition, Zr(IV) is abundant and its low toxicity makes it an interesting building block to work with for biological applications.[42] With excellent porosity, high stability, and structural diversity, Zr-based MOFs have numerous possibilities.[42] This thesis will focus on three Zr-based MOFs, MOF-808 and the isoreticular MOFs UiO-66 and UiO-67.

1.3.1. MOF-808

Furukawa *et al*. discovered the Zr-based MOF, MOF-808 (Figure 1.5), which has permanent porosity and large pores, useful for many applications.[43] The MOF is synthesized solvothermally by combining zirconyl chloride octahydrate ($ZrOCl_2$) and 1,3,5-benzentricarboxylic acid (H_3BTC) linker in a solvent mixture of *N,N*-dimethylformamide (DMF) and formic acid modulator.[43, 44] The overall structure is comprised of a six connected Zr_6-cluster node where six BTC linkers and six formate ligands are coordinated to one SBU.[43] Further characteristics of the MOF network include it's **spn** (spinel) topology, giving rise to two pore shapes and sizes; tetrahedral small pores of 4.8 Å and one adamantine large pore of 18.4 Å in diameter.[43, 45] With some of the capping ligands pointing into the channels and having open-metal sites accessible, this topology provides many advantages to introduce functionality through PSM processes and accessibility for guest molecules.[45] Single crystal data show that MOF-808 has a cubic space group, $Fd\bar{3}m$, with the spinel network.[43] Attributed with a high surface area of 2060 m^2g^{-1} and a pore volume of 0.85 cm^3/g, MOF-808 is one of the most highly robust MOFs with permanent porosity.[46]

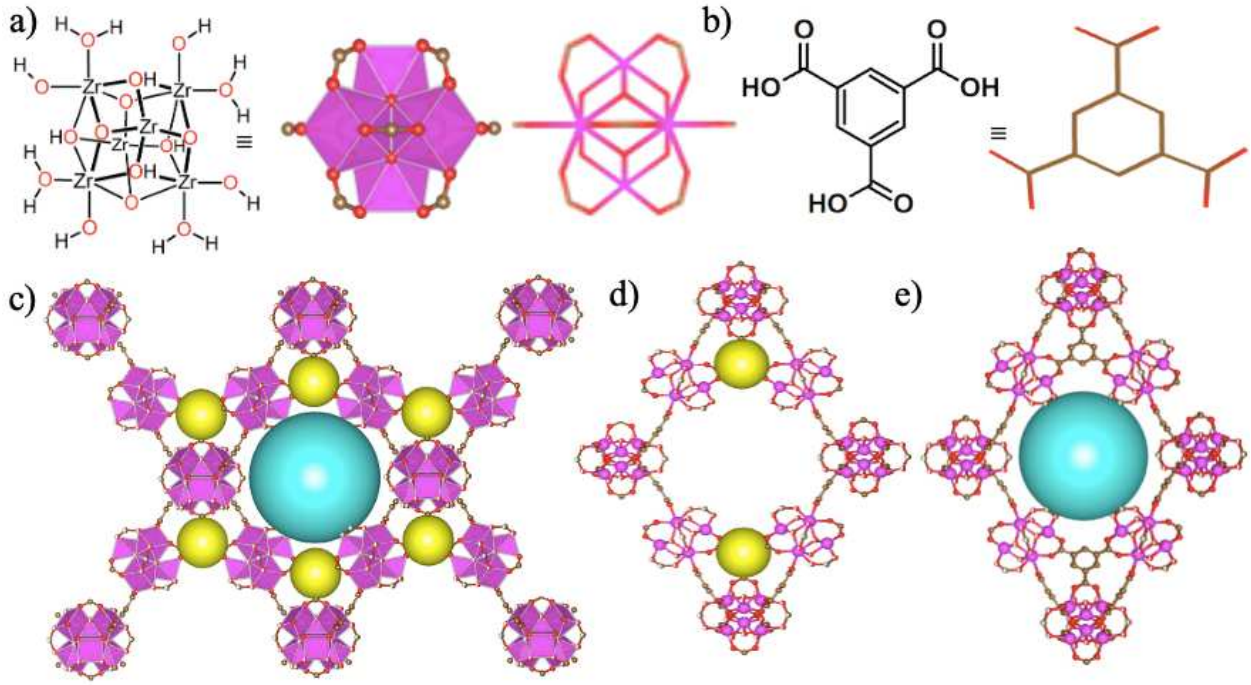

Figure 1.5. Representation of MOF-808 constituents a) Zr_6 hexanuclear cluster b) tritopic 1,3,5-benzenetricarboxylic acid BTC linker c) MOF-808 with **spn** topology and two cages of d)

tetrahedral cage (yellow spheres) and e) one adamantine (blue sphere). Zr_6-based metal cluster (magenta), oxygen (red), and carbon (brown).

The presence of the modulator in any MOF synthesis is to ensure a dynamic process where the overall framework of the MOF is stabilized throughout the synthesis and the rate of crystal growth is controlled. Specifically, formic acid is the most commonly used modulator for the synthesis of MOF-808, however, propionic acid and acetic acid have also been reported as modulators (Figure 1.6).[44, 47] The activated form of MOF-808, free of formate capping ligands, is achieved by heating the MOF in fresh solvent or soaking in a diluted hydrochloric acid (HCl) solution.[44, 46] The resulting activated MOF material yields six –OH and six $–OH_2$ ligands coordinated to each of the six-connected metal nodes.[44]

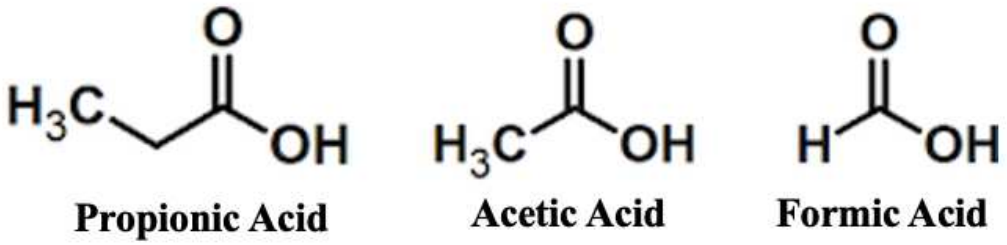

Figure 1.6. Modulators used in the synthesis of MOF-808.

1.3.2. UiO-66 and UiO-67

As one of the most studied and widely used MOFs, UiO-66 is a benchmark for its outstanding performance in many applications. Named after the University of Oslo (UiO) where it was first reported and synthesized, UiO-66 has gained increasing attention for its high stability, and reproducible and straightforward lab-scale synthesis.[48] The overall MOF structure is comprised of Zr_6-clusters bridged by a ditopic 1,4-benzenedicarboxylic acid (H_2BDC) linker (Figure 1.7).[48, 49] According to the RCSR, UiO-66 exhibits an **fcu** topology with an $Fm\bar{3}m$ crystallization space group.[48] Described as 12-connected, there are twelve linear ditopic BDC linkers coordinated to the Zr_6-metal clusters.[50] The Zr_6-based cluster is bridged by oxygen atoms in the form of μ_3-O and μ_3-OH ligands, giving rise to the strong Zr-O bonds defining the overall stability.[48, 50, 51] The MOF structure is defined as having two different types of cages: a small tetrahedral cage of 7.5 Å and a large octahedral cage of 12 Å in diameter.[48] With a pore volume of

0.77 cm^3/g and a surface area of 1160 m^2g^{-1}, UiO-66 showcases permanent porosity and accessible surface area for many applications.[48]

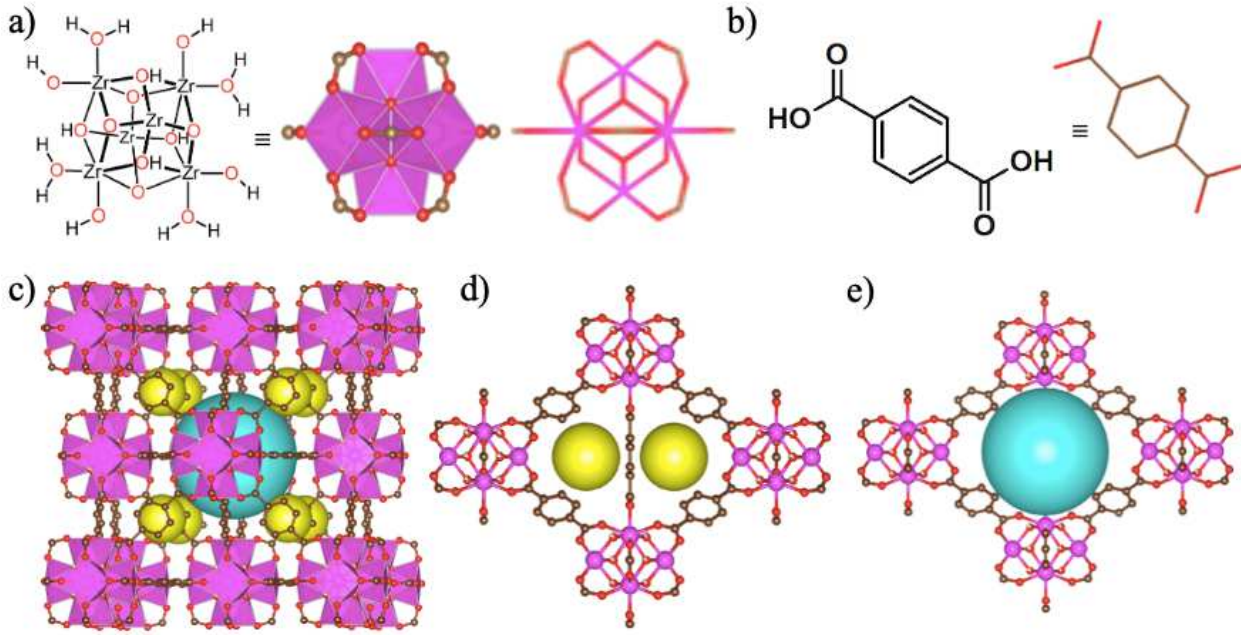

Figure 1.7. Representation of UiO-66 structure, building blocks and pores. a) Zr_6-based metal cluster, b) linear ditopic benzene dicarboxylic acid (BDC) linker, c) **fcu** topology, d) tetrahedral cage (yellow spheres) and e) octahedral cage (blue spheres). Zr_6-based metal cluster (magenta), oxygen (red), and carbon (brown).

Early work on the solvothermal synthesis of UiO-66 reported mixing a Zr^{4+} metal salt with the BDC linker dissolved in a DMF solvent and heated overnight.[48] As the first generation of Zr-based MOF, the lack of a modulator led to a rapid reaction resulting in a gel-like product.[48] The modulator used to synthesize UiO-66 normally consists of a carboxylic acid (-COOH) functional group (i.e., acetic acid, benzoic acid) that will compete with the linker in binding to the metal node.[48] The amount of modulator plays a role in nucleation as too low concentrations of modulator can result in a material with short-range order and a gel-like product.[48] On the other hand, too high concentrations of modulator result in a high number of defects in the MOF, including missing linkers or missing metal nodes.[48] Introducing defects (i.e., missing linkers) in a MOF can be advantageous as it can result in higher surface areas and larger pores for the encapsulation of guest molecules, but too many defects can affect structural integrity.[48]

Owing to the versatility of UiO-66, functionalized analogues can be synthesized with amine (UiO-66-NH_2), bromine (UiO-66-Br) or fluorine (UiO-66-F) groups, to name a few and giving rise to a series of isostructural MOFs.[48, 52, 53]

Also a Zr-based framework, UiO-67 is comprised of a Zr_6-based metal cluster bridged by a biphenyl-4,4'-dicarboxylate (H_2BPDC) linker (Figure 1.8).[53] Having similar solvothermal synthesis and reproducibility as UiO-66, UiO-67 exhibits high thermal and chemical stability.[53, 54] Compared to UiO-66, UiO-67 has a higher expected surface area of 2500 m^2g^{-1} and pore volume of 0.85 cm^3/g.[53, 55] Owing to the longer BPDC linker used in the UiO-67 synthesis, the tetrahedral cage is of 11.5 Å and the octahedral cage of 23 Å in diameter, making the pores larger for the encapsulation of guest molecules.[53] UiO-67 also follows the same topology as UiO-66, exhibiting an **fcu** unit cell with an $Fm\bar{3}m$ crystallization space group.[48, 55]

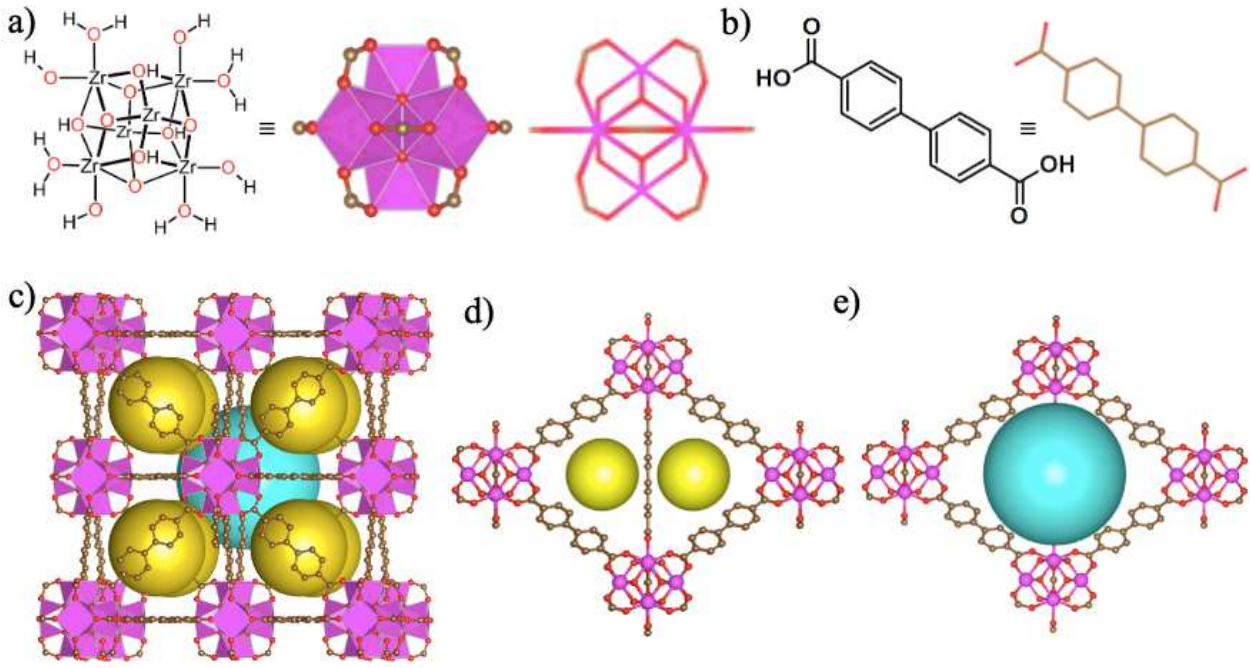

Figure 1.8. Representation of UiO-67 structure, building blocks and pores. a) Zr_6-based metal cluster, b) linear ditopic biphenyldicarboxylic acid (BPDC) linker, c) **fcu** topology, d) tetrahedral cage (yellow spheres) and e) octahedral cage (blue spheres). Zr_6-based metal cluster (magenta), oxygen (red), and carbon (brown).

1.3.3. Isoreticular MOFs

Isoreticular chemistry can allow for the addition of functional groups and tunable pores in MOFs. It is defined as the same overall spatial arrangement of the MOF (i.e., topology and network), but the chemical components can be different.[56] Isoreticular series of MOFs can be synthesized by (i) tuning the parent framework precursors (i.e., linker size, or metal ion), and (ii) post-modification (i.e., metal site or linker replacement, or modification).[56] Yaghi and co-workers have studied and synthesized a class of porous frameworks and introduced a series of isoreticular MOFs from the parent MOF-5 by introducing different functional groups on the ditopic carboxylate BDC linker including -Br, and -NH_2, all while maintaining the primitive cubic (**pcu**) topology.[57, 58] In addition, combining the octahedral Zn-O metal node with extended ditopic linkers including BPDC, gives a MOF-5 analogue with an expanded pore size.[57] In order to design derivative structures without altering the topology from the parent framework, it is important to consider (i) the properties of the precursors necessary for the assembly of the framework, (ii) the synthesis must be flexible for the use of derivatives, and (iii) the final framework should maintain the same topology.[57]

1.3.4. Isostructural MOFs

UiO-66 and UiO-67 are isoreticular MOFs that are also considered to be isostructural, defined as having the same overall crystal structure (same 12-connected metal cluster and topology) but different unit cell dimensions owing to the extended BPDC linker used in the UiO-67 synthesis.[55]

1.3.5. Nanosized MOFs

Nanoscale MOFs, also commonly referred to as nanoMOFs, present a leading discovery in the field of MOFs with a variety of promising new properties and structural diversity for implementation in many applications such as catalysis,[59–61] gas storage and separation,[62, 63] and biomedicine.[64–67] The unique properties that make nanoMOFs of interest include (i) fast adsorption/desorption kinetics, (ii) high surface areas coupled with high surface to volume ratio, and (iii) ease of accessibility to internal active sites and pore space.[68] NanoMOFs can be synthesized through (i) solvothermal synthesis, (ii) microemulsion, (iii) microwave-assisted synthesis, and (iv) ultrasound-assisted synthesis to name a few.[68, 69] Solvothermal synthesis remains the most efficient and flexible approach for controlling the nucleation and growth rate of

nanoMOFs by modifying synthesis parameters including (i) modulator concentration, (ii) reaction time, (iii) pH, and (iv) temperature to regulate the particle size of MOFs.[68, 70] In addition, the uniform morphology and monodispersity can be controlled by regulating the above-mentioned synthetic parameters, notably (i) modulator concentration and type to give precise control over the crystallization process by separating the nucleation and growth steps – as fast nucleation leads to smaller but more uniform size distributions, and (ii) constant stirring of the reaction mixture – allowing the precursors to be dispersed in a homogeneous way.[69–71] For some applications including drug delivery, nanoMOFs of less than 200 nm in size are desired and must have good colloidal stability to avoid aggregation when dispersed in solution.[72] The advantages of nanoMOFs in drug delivery include (i) increased velocity and diffusion in physiological conditions, (ii) prolonged blood circulation time, (iii) good biocompatibility, all while remaining tunable with physiological stability.[68] For the scope of this thesis, the use of nanoMOFs for drug delivery will be explored and discussed.

1.4. Methods in MOF Synthesis

1.4.1. Synthetic Approach

The approach used for MOF synthesis stems from understanding coordination of the inorganic building blocks and the organic linkers, as well as the kinetics and dynamic processes that give rise to nucleation and crystal growth.[36, 73] Several methods have been proposed to synthesize MOFs including microwave-assisted heating,[74] electrochemistry,[75] and mechanochemistry[76] to name a few. The most widely used synthesis route is solvothermal under conventional heating.[77] Also referred to as *de novo* synthesis, the self-assembly process consists of mixing the metal salt and the organic multitopic linker with a high-boiling point solvent in a closed screw-top vessel or reaction jar and heated in an oven or hot plate at temperatures varying between 80-150 ℃ for typically 12-48 h.[36, 77] Different reaction parameters can be varied to tailor the synthesis such as (i) solvent, (ii) temperature, (iii) reaction time, (iv) concentration, and (v) pH.[36] Choosing the right solvent is very important in MOF synthesis as it will provide the medium for crystal growth and allow for structure propagation.[78] In addition, the choice of solvent also acts to deprotonate the carboxylic acid ligands and provide a basic environment.[78] Commonly used high-boiling solvents for MOF synthesis include DMF, *N,N'*-dimethylacetamide (DMA), or *N,N'*-

diethylformamide (DEF) as most precursors are soluble in these solvents and they remain liquid at temperatures at which crystallization occurs.[79]

Another important parameter in MOF synthesis is the presence of a modulator. Modulators are defined as non-structural monotopic ligands that compete with multitopic linkers for binding to metal nodes.[36] The purpose of a modulator is to ensure a dynamic process and overall slow crystal growth.[36] As often the metal to linker bonding in solution is so strong, that bonding will lead to precipitation out of solution and result in premature structure termination.[36] Therefore, with the presence of a modulator, one can favor the formation of metal to ligand bonds all while breaking and reforming those bonds in order to fully propagate a structure in 2D or 3D.[36, 80] Typical examples of monotopic modulators that have been widely used in Zr-based MOF synthesis include hydrochloric acid, and -COOH-based functional groups such as acetic acid, benzoic acid, and formic acid.[36] The dynamic process of the modulator has not only facilitated MOF synthesis but has offered insight into controlling particle size, introducing defects, and controlling physical properties.[81]

1.4.2. MOF Activation

To achieve the highest possible surface area and porosity of a MOF, it is important to perform an activation step following MOF synthesis. Many precursors (i.e., solvent, reagents), impurities, and by-products can be trapped within the pores and on the surface of the MOF, impeding overall access, and lowering the surface area of the resulting material.[36] Activation involves washing and soaking the MOF with the solvent that was used throughout the MOF synthesis for a few hours or days to allow full infiltration of the fresh solvent into the pores and on the surface of the MOF.[36] By performing a cycle of washes and soakings, it can ensure the removal of any guest molecules and uncoordinated linkers impeding accessible areas of the MOF.[36] The most desirable MOFs are those with permanent porosity and high surface areas to allow encapsulation of guest molecules for many applications.[82]

There are a few ways to perform the activation step including solvent-exchange and vacuum drying, as well as supercritical CO_2 drying ($scCO_2$).[82] Activation by solvent-exchange is the most widely performed method of activation which involves the exchange of a high-boiling solvent (i.e., DMF) for a lower boiling-point solvent (i.e., acetone, ethanol, or methanol) (Figure 1.9).[82] First, the MOF is washed and soaked multiple times with the high boiling-point reaction

solvent in a centrifuge tube and it is collected by centrifugation.[36] Following is the exchange and soaking with a lower boiling-point solvent.[82] Essentially, lower boiling-point solvents have weaker intermolecular interactions and have little surface tension effect on the framework of the MOF, impeding capillary force tension that can be destructive to the MOF.[82, 83] Using a lower boiling-point solvent has been proven to retain not only the overall structure but porosity of the MOF as observed with powder X-ray diffraction (PXRD) and N_2 adsorption-desorption measurements, compared to using water as an exchange solvent.[83] Once the solvent-exchange process is complete, the MOF is then placed under vacuum with applied heating that is between the boiling point of the solvent but below the decomposition temperature of the MOF structure.[36] Alternatively, $scCO_2$ is a complementary activation process where the high boiling-point reaction solvent is replaced with liquid CO_2, followed by conversion of liquid CO_2 to $scCO_2$ at high pressure and temperature, and then venting the $scCO_2$ at temperatures above the critical point.[82] Essentially, this activation process is less invasive to the framework as it avoids passing through the liquid-to-gas phase that is critical for high capillary forces, and alternatively passing directly to the gas-phase.[82]

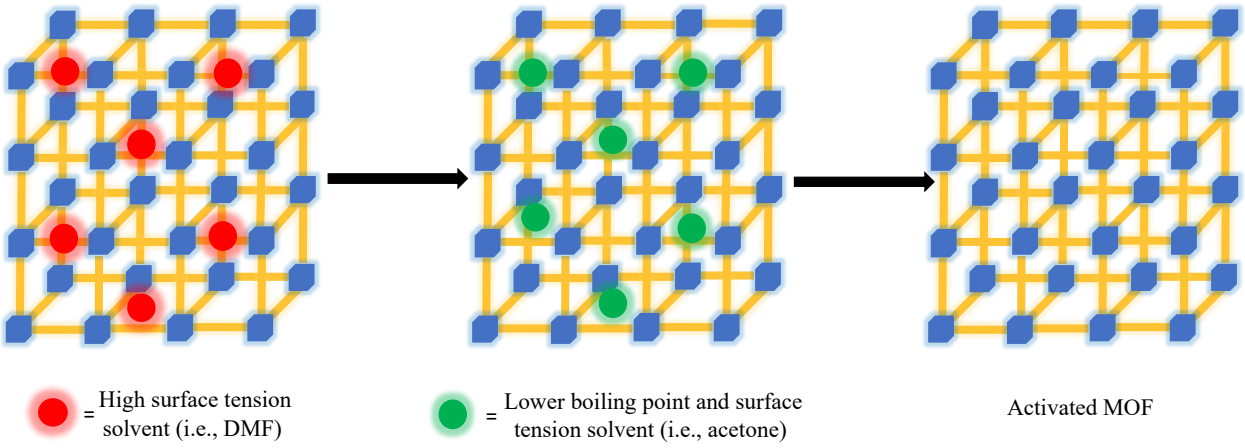

Figure 1.9. Schematic of MOF activation process through solvent exchange.

1.4.3. MOFs for Drug Delivery

The use of MOFs for drug delivery applications (Figure 1.10) has expanded over the past few decades owing to their ease of functionality coupled with tunable surface areas and pore sizes, allowing for the encapsulation of drug molecules while also targeting specific sites in the body.[84] As such, many parameters including the (i) metal, (ii) linker, (iii) SBU, (iv) morphology, and (v)

the potential for open-metal sites are important to consider for drug delivery and predetermine the fate of the adsorption, release, and degradation of the MOF in biological applications.[17] In addition, MOFs have demonstrated high drug loading capacities, controlled release of drug cargo and allow for precise control of surface functionalization, making them versatile and adaptable for the loading of a variety of drug molecules and improving retention times for efficient targeting.[17] Tuning PSM of MOFs has also been widely studied to improve the drug loading and release capacities. Examples include, but are not limited to, surface modification with a polymer coating (i.e., polyethylene glycol) to improve MOF biocompatibility[85] and functionalization of a linker to introduce a surface charge for charged drug molecules.[17] To further optimize the biocompatibility of MOFs and their performance in biological applications, the properties of the building blocks (i.e., metal and linker) need to be considered to ensure their toxicity threshold is not too high for human bodies.[86] The size of the MOF is also an important factor for the biodistribution and circulation lifetime of the drug loaded MOF, which should not exceed a particle size of 200 nm.[86] The interaction of the drug molecules and the MOF is governed by a concentration gradient and has been found to occur through chemical interactions such as van-der-Waals forces, $\pi - \pi$ stacking, electrostatic interactions, and hydrogen bonding.[17, 87] The use of MOFs for drug delivery has been explored for cancer therapy with the encapsulation of anticancer drugs like doxorubicin,[88] nucleic acid delivery to activate biological treatments for a variety of diseases,[89] and protein macromolecules in which they are protected from enzyme deactivation and improve their overall efficacy.[90]

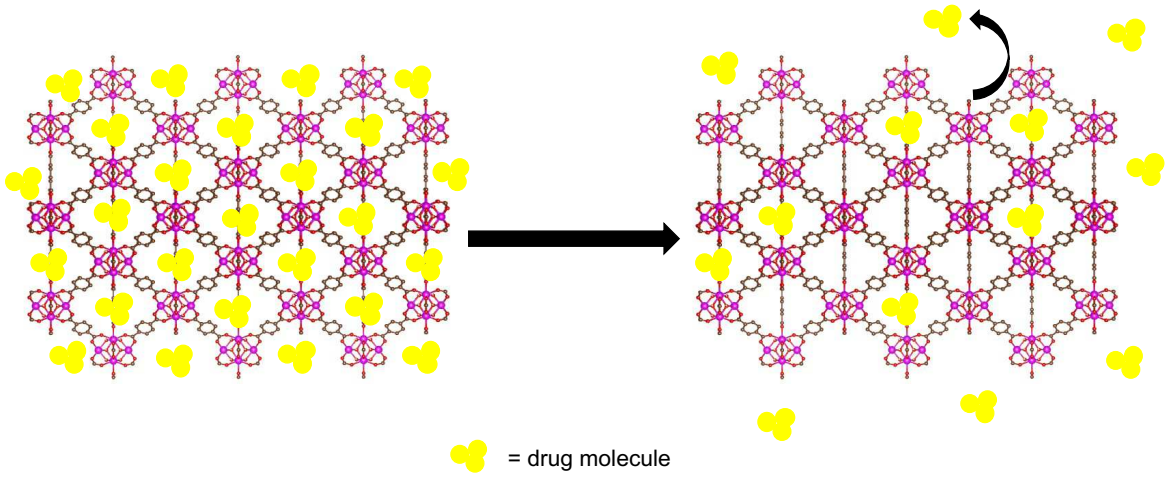

Figure 1.10. Schematic of UiO-66 as a drug carrier with the encapsulation and release of the drug molecules.

1.5. MOF Characterizations

1.5.1. Overview of MOF Characterization Techniques

MOFs are complex structures with many diverse properties and characteristics defining their potential for many applications. As such, to understand their unique features and properties, a series of characterization techniques are explored post MOF synthesis which can allow us to understand the wide array of MOF materials. In this thesis, the techniques that are used include (i) PXRD that can provide information on the overall bulk crystallinity and phase purity of the MOF structure, (ii), N_2 adsorption-desorption to measure the surface area and porosity, (iii), proton nuclear magnetic resonance (^{1}H-NMR) spectroscopy to quantify linker incorporation and linker ratios, (iv) dynamic light scattering (DLS) to gain information on the crystallite size of the MOF, (v) diffuse reflectance infrared Fourier transform spectroscopy (DRIFTS) that measures the IR active functional groups in the MOF structure, (vi) scanning electron microscopy (SEM) that is a qualitative and quantitative technique providing insight into MOF topology and particle size, respectively, and (vii) transmission electron microscopy (TEM) that is also a qualitative and quantitative technique offering information on MOF morphology and particle size mainly for nanosized MOF materials. In addition to these standard techniques used for MOF characterization, ultraviolet-visible (UV–Vis) spectroscopy is used to quantify the surface accessible thiol groups of the thiolated MOFs.

1.5.2. Powder X-ray Diffraction (PXRD)

One of the preliminary characterization techniques used to confirm the synthesis of MOFs is PXRD. A diffractogram is collected and yields useful information on MOF integrity, unit cell dimensions, phase composition, and crystallite size. A diffractogram includes an experimental pattern and a simulated pattern (in some cases accessed using the Cambridge Crystallographic Data Centre (CCDC)) to which the experimental pattern can be compared to confirm the phase purity of the MOF (Figure. 1.11). In addition, a set of allowed reflections represent all the possible reflections for a given MOF and are included to indicate if there are any impurities present in the MOF identified by the presence of additional or missing peaks in the pattern. It is also greatly important to include allowed reflections to circumvent confusion caused by preferred orientation that can lead to missing peaks and differences in peak intensities.[36] It is best to have sample rotation to observe random crystallite orientations.[36]

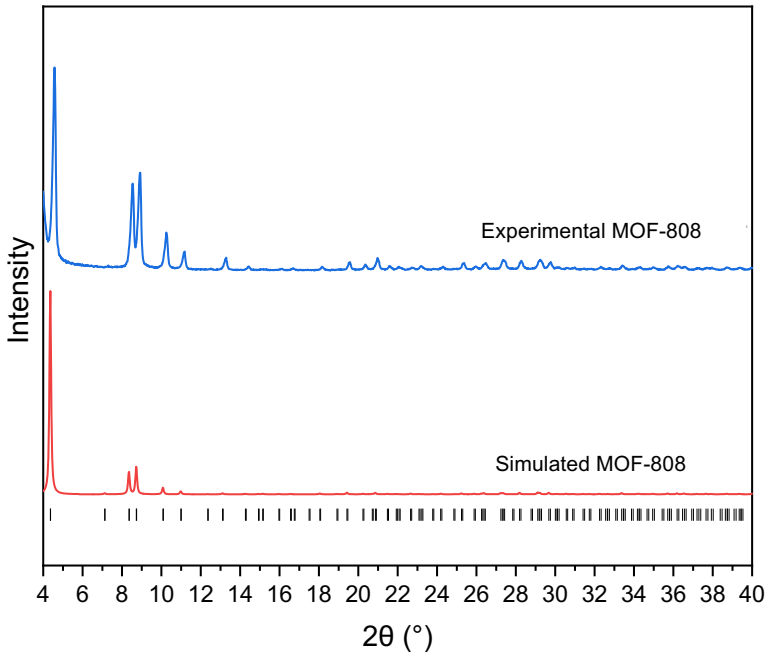

Figure 1.11. PXRD diffractogram of the simulated (bottom) and experimental (top) patterns for MOF-808. The allowed reflections are shown with black tick marks.

The general PXRD sample preparation consists of placing the dry powdered MOF sample onto a zero-background silicon holder. Composed of a monocrystalline silicon-grown base and sliced across a plane that will not diffract most routine analysis, one can obtain high-quality data with no interferences from scattered or diffracted peaks from the silicon substrate.[91] MOF samples can also be drop casted onto the sample holders with volatile solvents. A set of X-rays are generated by a cathode ray tube and further accelerated by a copper anode (Cu K-alpha (Kα) 1.5406 Å) targeting the sample on the rotating sample holder and upon X-ray exposure, a 1D semiconductor detector will translate to an intensity count.[92] Most PXRD instruments are also equipped with a nickel filter (i.e. Ni (K_β)) that is essential to block out the K_β radiation that can result in a polychromatic peak leading to the presence of two peaks or peak broadening. When the X-rays interact with the sample material, the diffraction can produce constructive (in-phase) or destructive (out-of-phase) interference at specific angles. The angle at which the constructive interference is produced can be calculated with Bragg's law ($n\lambda = 2dsin\theta$) to gain information on the d-spacings between the lattice planes and the diffractogram is obtained once Bragg's law is satisfied at varying angles.

1.5.3. N_2 Adsorption-Desorption Experiments

Gas adsorption is the most widely used technique to determine MOF surface areas, pore sizes and pore volumes. Nonreactive gases (i.e., nitrogen (N_2) at 77 K, argon (Ar) at 87 K, and carbon dioxide ((CO_2) at 273 K) have been used for such measurements owing to some of their physical properties including (i) their high stability owing to their full valence electron shells meaning they are unlikely to form chemical bonds when in contact with the adsorbent,[93] and (ii) their weak interatomic forces result in low-boiling and melting points suitable for the analysis of gas adsorption.[94] However, N_2 gas remains the most widely and commonly used gas for isotherm measurements due to its well-defined properties. N_2 gas is widely available, inexpensive, non-reactive with most materials, and has a constant effective adsorbate area (16.2 m^2g^{-1}) allowing the gases to closely pack with the surface and pores of the material and form reasonably defined monolayers.[95] The type of adsorption that can occur includes physisorption and chemisorption; physisorption being more suitable for determining surface area and pore sizes. That said, physisorption occurs when an adsorbate gas encounters an adsorbent material forming Van der Waals' interactions giving rise to a reversible process.[96] A typical gas isotherm measurement consists of weighing an activated powdered sample in a tube with a filler rod inserted and capped with a seal frit. The sample tube is then mounted onto a vacuum manifold instrument with controlled heating to undergo a preliminary degas step where the material inside the tube is heated and evacuated under vacuum. The sample tube is then filled with an inert gas (i.e., Helium) to measure the void space and undergoes another round of degas to ensure all the helium has been removed. Following, the sample tube is then mounted onto a gas adsorption instrument where N_2 gas is adsorbed and pumped into the tubes at increasing pressure. Once the pores have been filled with N_2 gas, a monolayer is formed, and the desorption step occurs where the N_2 is evacuated at decreasing pressure. The adsorption and desorption process are represented by an isotherm where the relative pressure (P/P_0) represented by the equilibrium pressure and the saturation vapor pressure at the adsorption temperature is plotted as a function of the amount of N_2 gas adsorbed in cm^3/g at standard relative pressure (1 atm) and temperature (298 K). There exist six classifications of adsorption isotherms as represented in (Figure 1.12).

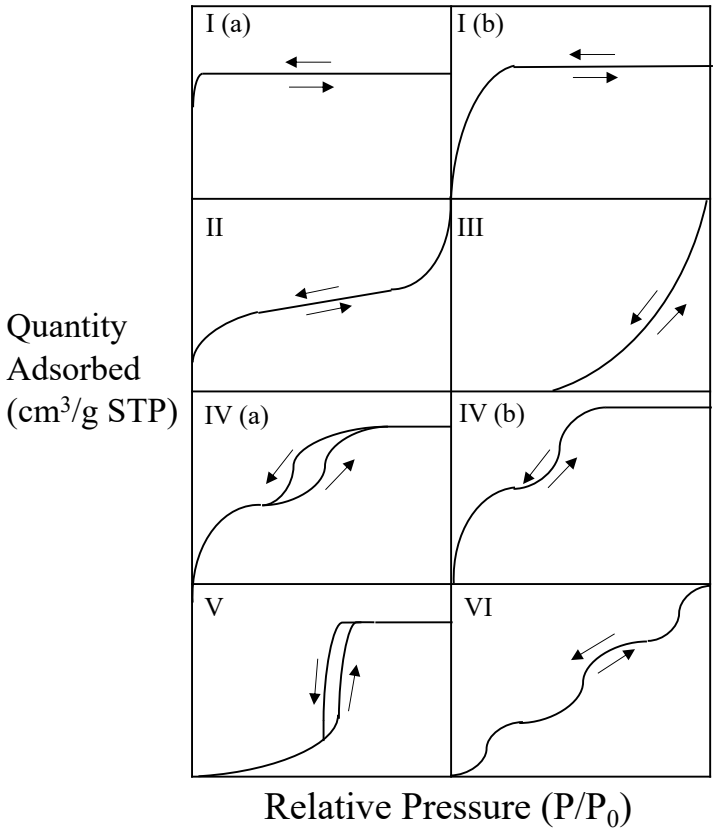

Figure 1.12. Classification of adsorption isotherms ranging from Type I to Type VI.

The accessibility of the gas adsorbate to the pores of the MOF is dependent on the shape and size of the MOF internal pores and surface area.[96] According to the IUPAC definition and classification of pore sizes, there exist three types of pore widths. Pores exceeding a width of 50 nm are termed macropores, pores widths between 2 nm and 50 nm are termed mesopores, and pore widths less than 2 nm are termed micropores.[96] The isotherm classification is based on the above-mentioned pore widths and provide insight on MOF porosity. Type I reversible isotherms are designated for microporous solids, represented by a steep uptake at high pressure. Type I isotherms can be subcategorized into Type I(a) – microporous materials with narrow pore widths and Type I(b) – microporous materials with slightly larger pore widths. The Type II isotherm classification is designated for macroporous or non-porous materials, as represented by a plateau caused by an initial monolayer completion, followed by an unrestricted monolayer and multilayer adsorption. Type III isotherms are related to macroporous, or non-porous materials represented by a weak adsorbent-adsorbate interaction. Type IV isotherms are given by mesoporous materials and further subcategorized into Type IV(a) – as represented by an initial monolayer coverage, followed by a

non-reversible adsorption-desorption curve, most termed by hysteresis. Hysteresis is generally associated with pore condensation when the pore width exceeds a critical width of more than ~ 4 nm.[96] Type IV(b) – is represented by a reversible process with mesopores below the critical width. Type (V) isotherms are related to Type III isotherms with weak adsorbent-adsorbate interactions and pore fillings at higher relative pressures. Type (VI) isotherms are designated for uniform, non-porous materials and represented by a stepwise layer-by-layer adsorption.[97]

To determine the surface area from an adsorption isotherm, the Brunaeur-Emmett-Teller (BET) theory is the most suitable for a broad range of isotherm types and porous materials. BET theory predicts the number of gas adsorbate molecules needed to form a monolayer, even when some adsorbent sites are more energetic resulting in a multilayer adsorption prior to a monolayer formation. Contrarily, the Langmuir theory is used for surface area analysis and calculations but assumes that only a perfect monolayer is formed. Hence, this is not an acceptable theory for fitting MOF isotherms since it is best for simple materials with limited pores sizes and surface areas. In addition to surface area calculation, pore density and size/volume profiles can be analyzed by the non-local-density functional theory (NLDFT) that models the microfluid density at cryogenic temperatures (N_2 gas at 77 K).[98]

1.5.4. Nuclear Magnetic Resonance (NMR) Spectroscopy

Nuclear magnetic resonance (NMR) spectroscopy is a characterization technique that provides information on linker ratios, MOF purity, ligand incorporations, leftover modulator, and the presence of solvent in a MOF (Figure 1.13).[36] The general sample preparation for NMR spectroscopy samples requires digestion of the MOF with a few drops of deuterated acid (i.e., sulfuric acid (D_2SO_4), or a mixture of diluted deuterated sodium hydroxide (NaOD) with deuterated water (D_2O)) followed by sonication to ensure that the MOF is well dispersed in the acid.[36, 99] This step is a fundamental requirement for MOF samples as MOFs are not soluble in conventional NMR solvents (i.e., deuterated dimethylsulfoxide (DMSO-d_6), or deuterated chloroform ($CDCl_3$)). Hence, by digestion with concentrated deuterated acid or base, the bonds in the MOF (i.e., metal-linker, or metal-modulator) are broken, followed by the addition of NMR spectroscopy solvents to dissolve the components.[99] Solid-state NMR spectroscopy (ssNMR) is a complementary technique used for the analysis of whole MOF structures, characterizing host-guest interactions, and probing the local environment of metal clusters.[100–102]

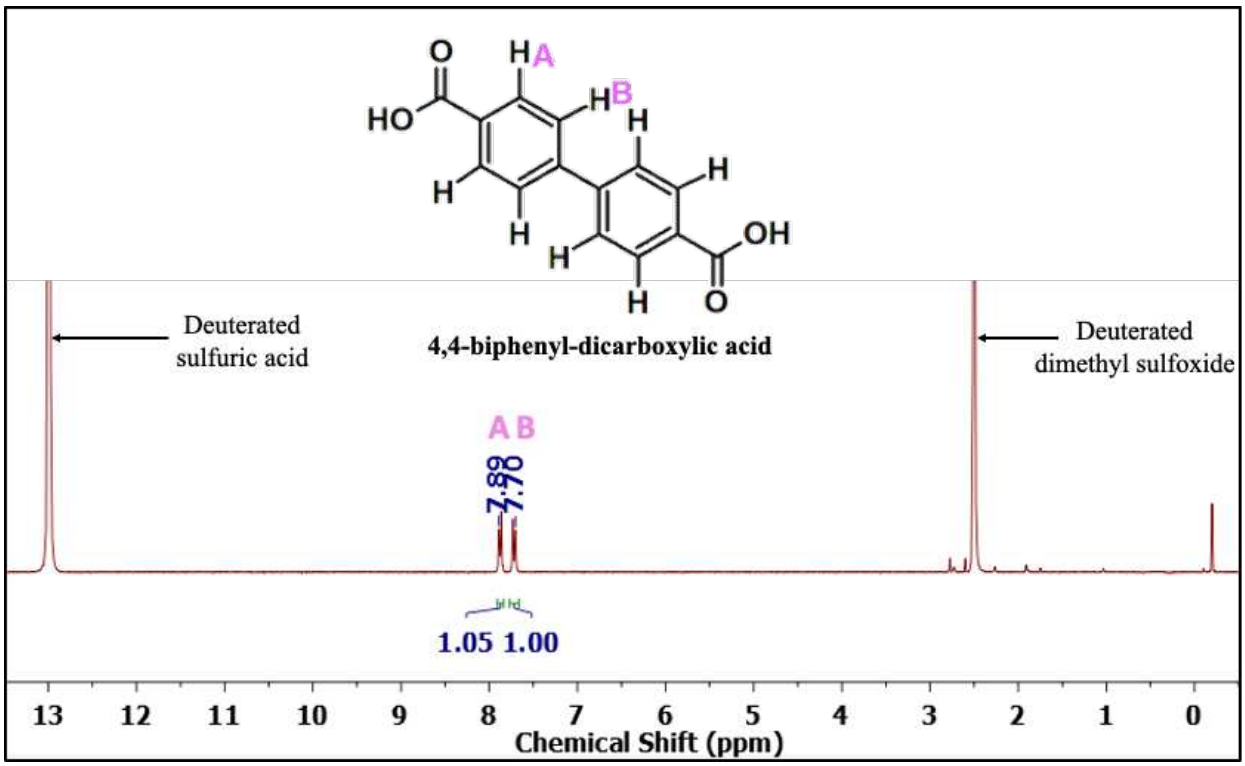

Figure 1.13. [1]H-NMR spectra of UiO-67 digested in D_2SO_4 and DMSO-d_6 to digest and dissolve the mixture.

1.5.5. Ultraviolet-Visible Absorption Spectroscopy (UV–Vis)

The amount of light transmitted through a sample can be measured by UV–Vis absorption spectroscopy. It is a quantitative technique that provides information on the intensity of light passing through a sample with an analyte, with the only requirement being that the analyte absorbs in the UV–Vis region of the electromagnetic spectrum. Based on the Beer-Lambert law ($A = \varepsilon lC$), where A is the absorbance, ε is the constant molar absorptivity, l is the length of light path, and C is the concentration, one can calculate the concentration of a sample based on the linear relationship between absorbance and concentration. Samples for UV–Vis can include solutions, but also solid state samples by UV–visible diffuse reflectance spectroscopy (UV–Vis DRS) and can be applied to measure the absorption of light reflected off the sample interior and surface.[103] Most commonly carried out in solutions, the samples are prepared in quartz cuvettes and a reference cuvette (without the measured substance) is prepared to avoid error due to the reflected light at the cuvette surfaces or absorbance of solvents.[104] For any quantitative technique, a standard calibration curve is plotted with known concentrations of a standard analyte, followed by measuring the absorbance

of the unknown analyte of interest to determine the concentration based on the Beer-Lambert law. UV–Vis spectroscopy is used in this thesis for thiol quantification as explained in section 1.5.10.

1.5.6. Diffuse Reflectance Infrared Fourier Transform Spectroscopy (DRIFTS)

Diffuse reflectance infrared Fourier transform spectroscopy (DRIFTS) is a useful characterization technique that will confirm the presence or absence of IR active functional groups in a MOF, as well as the interaction with guest molecules.[36] The IR spectrum is obtained when incident infrared light interacts with the sample using an instrument equipped with mirrors and optics to reflect the light in multiple directions. A stream of inert gas (i.e., N_2) is purged throughout the instrument at a regulated flowrate to ensure no accumulation of water or moisture condenses on the mirrors.[105] DRIFTS can be used to measure functional groups that are found internally (i.e., pores) as well as the surface of the MOF. The general experimental approach of DRIFTS consists of mixing activated dry MOF powder and potassium bromide (KBr) pellets to increase the reflectance coming off from the sample, into a finely ground solid powder with a mortar and pestle.[36] The use of a mortar and pestle to compress the powders together is more mild than applying direct mechanical strain on the MOF itself like in other IR spectroscopy techniques (i.e., ATR), hence DRIFTS remains more suitable for MOF samples.[106] The MOF samples should also be properly activated and vacuum dried prior to DRIFTS analysis as water or exposure to air can influence spectral features, more specifically perturbing the hydroxyl bands (3500 – 3800 cm^{-1}).[36, 106] In addition, the presence of water can block open-metal sites and the ability to probe interactions with guest molecules.[106]

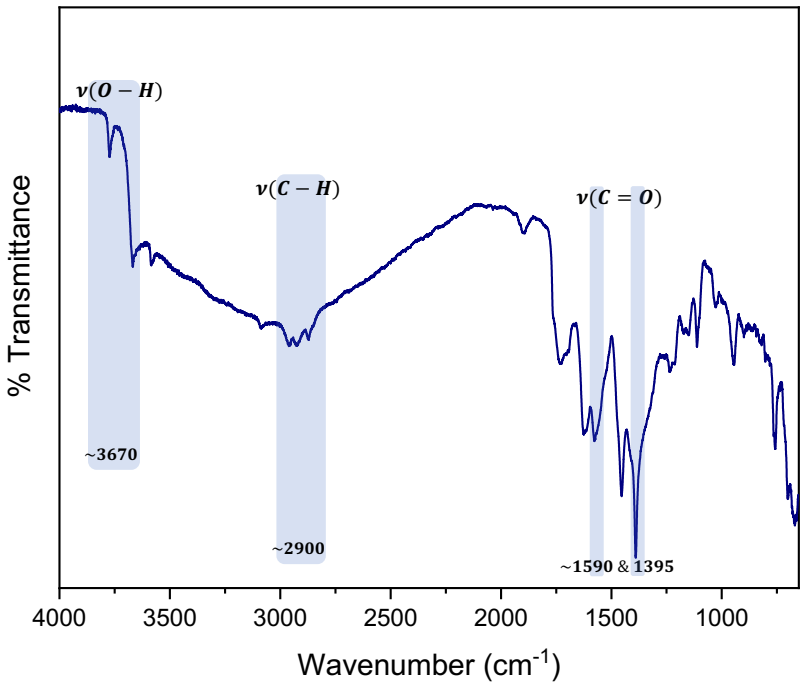

Figure 1.14. DRIFTS spectra of MOF-808 showcasing the characteristic peaks in the region of 3670 cm^{-1}, 2900 cm^{-1}, 1600 cm^{-1} and 1590 cm^{-1} and 1395 cm^{-1} attributed to the terminal and bridging -OH stretches of the metal node, -CH and -C=O stretches from the organic linker, respectively.

A DRIFTS spectrum (Figure 1.14) for most Zr-based MOF samples will include absorption bands stemming from common functional groups. Specifically, -OH bridging and terminal stretches from the metal cluster will appear at 3671 cm^{-1}, and 3674 cm^{-1}, respectively.[39] The carbonyl -C=O appear as two stretches around 1395 cm^{-1} and 1590 cm^{-1} attributed to the symmetric and asymmetric vibrations from the organic linker, followed by the asymmetric and symmetric -CH_3 and -CH_2 stretches of the organic linker in the region of 2900 cm^{-1}.[106]

1.5.7. Dynamic Light Scattering (DLS)

Dynamic light scattering (DLS), also referred to as photon correlation spectroscopy (PCS), is a useful characterization technique that provides information on particle size and size distribution. Based on Brownian motion, the hydrodynamic diameter of the particles (i.e., MOF crystallites) can be studied by their diffusion through a solvent medium and bombardment with solvent molecules.[107] A typical DLS experiment consists of a beam of light from a monochromatic

light source interacting with the particles in suspension and a photon detector will detect that signal as a function of intensity.[107] The hydrodynamic diameter can be calculated from the translational diffusion coefficient (D) stemming from the Stokes Einstein equation ($d(H) = \frac{kT}{3\pi\eta D}$). The (i) shape, (ii) size, (iii) temperature, (iv) viscosity, and (v) ionic strength of the solution are parameters that can directly influence the intensity and motion of the particles.[107] As such, the larger the particle sizes, the slower they will diffuse in solution, whereas the smaller the particles, the faster they will diffuse in solution.[107] Owing to the aggregation that arises from nanoparticles in concentrated solutions, it is often recommended to perform dilutions as to avoid measuring aggregates and obtain smaller size distributions.[108, 109] A typical DLS profile (Figure 1.15) will include one narrow peak indicating a monodisperse sample with a uniform size distribution. A cumulants analysis is often used as a method for fitting the coefficient from an algorithm where the mean size and polydispersity index (PDI) can be extrapolated. The PDI is a dimensionless measure indicating the broadness of the size distribution.[110] Typically, values between 0 to 1 are suitable for DLS measurements and values above 1 indicate that the sample has a high polydispersity.[110]

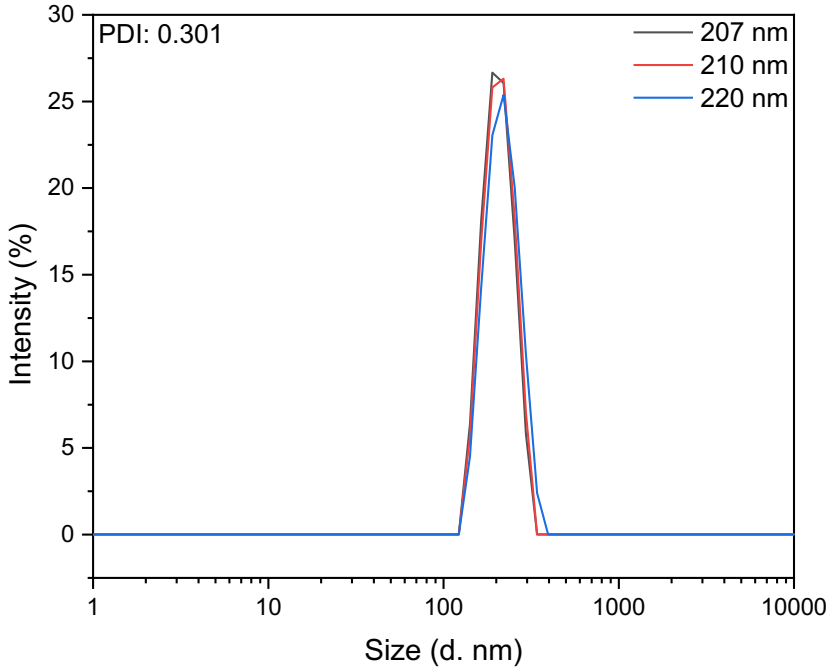

Figure 1.15. DLS profile of nanosized UiO-66 with an average particle size of 212 nm.

1.5.8. Scanning Electron Microscopy (SEM)

Determination of static particle size and morphology for porous materials can be characterized by scanning electron microscopy (SEM) (Figure 1.16). It is a technique that offers magnification of up to 150 000x and is performed under vacuum where electrons with voltages between 5-15 kV are accelerated and focused onto the sample surface and scanning is performed by the electron beam across the sample to generate information including size, morphology, and chemical composition in some cases. The SEM is equipped with condenser and objective lenses to focus the electron beam into a narrow point on the sample. Once the electrons have interacted with the sample, they will be scattered depending on the electron energies, atomic number (Z) of the elements in the sample, and the density. A secondary electron detector (SED) and backscattered electron detector (BSD) are most used to understand the interaction of the electrons with the sample surface and dictates the information we can obtain. SED detectors can provide topographic information as the electrons are generated from the surface of the sample, whereas a BSD can provide compositional information as the electrons originate from deeper regions of the sample. Dry powdered MOF samples are prepared on metal stubs and are often coated with a thin conductive layer of metal as MOFs are insulating.[36] As such, by sputter coating the MOF samples, the risk of charging effects can be minimized and mitigate issues of sample analysis and sample destruction. SEM can be coupled with energy dispersive X-ray spectroscopy (EDS or EDX) where an X-ray characteristic of the element is emitted to quantitate elemental composition and ratios.

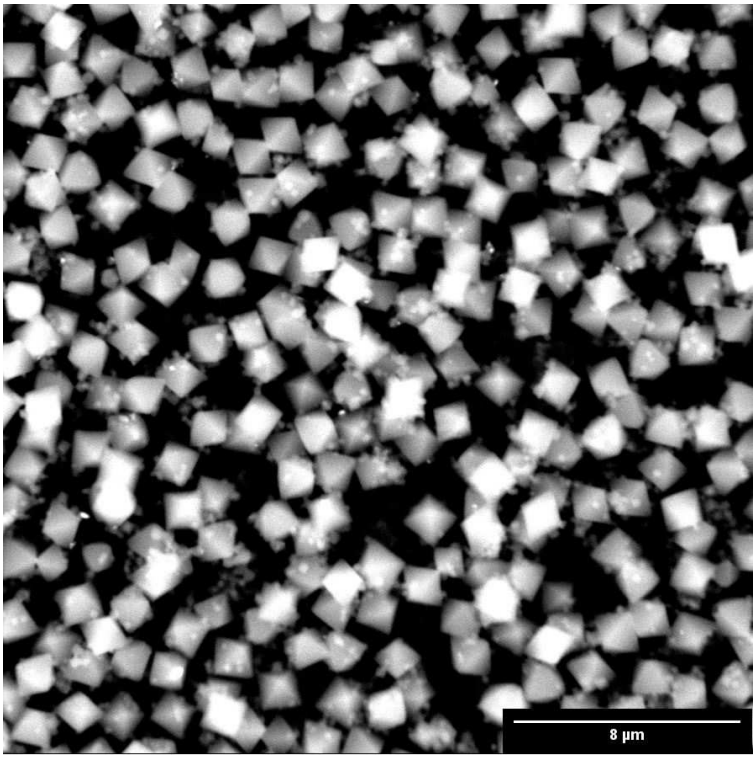

Figure 1.16. SEM micrograph of UiO-67 showcasing the octahedral morphology.

1.5.9. Transmission Electron Microscopy (TEM)

Also an electron microscopy characterization technique, transmission electron microscopy (TEM) allows for high resolution images that can be used to analyze what is inside and beyond the surface of MOF samples. TEM does not only analyze particle size, morphology, and composition of the MOF, but electron diffraction patterns as well as they can be useful to study polycrystalline or mixed crystalline phases.[111] The general instrumental components are like SEM however, TEM operates at much higher accelerating voltages (60 – 300 keV) and higher magnification levels. Sample preparation consists of creating a solution of MOF powder in a volatile solvent followed by sonication and dropcasting onto a carbon grid. There are different illumination modes in TEM including parallel (TEM) and convergent (STEM). Scanning transmission electron microscopy (STEM) is an illumination mode in TEM that produces an image based on converging the electron beam, producing signals that cannot be spatially correlated by TEM. Hence, with STEM, inelastic scattering can allow for analysis of X-ray emission (EDS) for elemental mapping,[112] and electron energy loss spectroscopy (EELS) for information on the local environment of atomic electrons.[113]

1.5.10. Thiol Quantification: Ellman's Test

Ellman's reagent, also commonly referred to as 5,5,'-dithiobis-(2-nitrobenzoic acid) DTNB for short, is used to quantify and estimate the external thiol groups on the surface of the thiolated materials.[114, 115] The test consists of the DTNB reagent reacting with the surface thiols on a material to result in a mixed disulfide and 2-nitro-5-thiobenzoate (TNB), as depicted in Figure 1.17.[114, 115] The yellow-colored product of the TNB can be quantified at ~ 400 nm by UV–Vis spectroscopy.[114] A standard calibration curve is prepared with N-acetyl-L-cysteine reagent at different concentrations ranging from 0 mM to 60 mM. The diluted solutions are then dissolved with a sodium phosphate reaction buffer, DTNB reagent, and 2-amino-2-hydroxymethyl-propane-1,3-diol (TRIS) buffer. The determination of free thiols can then be calculated based on the absorbance of the mixed disulfide.

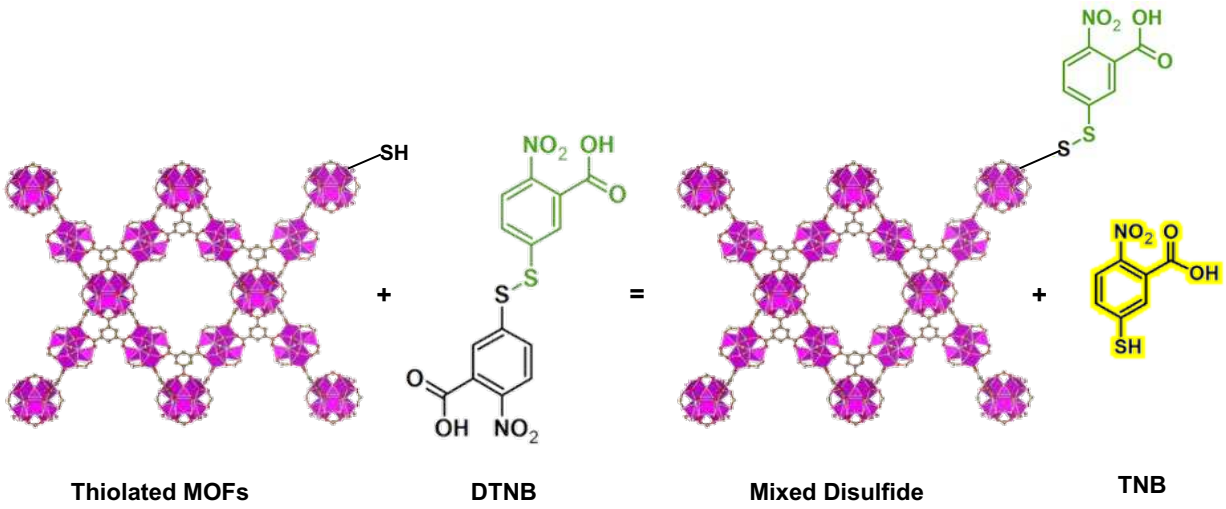

Figure 1.17. DTNB reagent with a thiol group reaction scheme represented by Zr_6-based metal cluster (magenta), oxygen (red), and carbon (brown).

1.6. Mucoadhesion Experiments

1.6.1. Properties of Mucins and the Mucosal Layer

Ophthalmology encompasses the study of major eye diseases associated with vision loss, including the risk factors and potential treatments with ongoing scientific research.[116] The external barrier on the surface of the eye is called the mucosa. The mucosa layer is comprised of 95% water, and 1-5% of lipids, salts, and other enzymes.[117] The gel-like layer of the mucosa stems from the

main component of the mucosa, that being mucins.[117] Mucins are a family of glycosylated proteins commonly characterized by their enriching properties including (i) high molecular weight (0.5–40 MDa), (ii) polypeptide backbone with amino acids rich in threonine, serine, and proline, (iii) high degree of glycosylation, and (iv) negative charge. 10% of mucins consist of cysteine amino acid regions, making them susceptible to many interactions.[117, 118] Mucins can be subdivided into two categories, (i) secreted mucins, described as gel-forming and small soluble with their main function to excrete pathogens, provide lubrication by their viscous properties, and provide antimicrobial activity,[119] and (ii) cell-surface associated mucins with lower molecular weight and extended cell surface up to 500 nm, providing surface protection, barrier, and osmosensing.[117, 119] There exist up to 20 mucin gene types ranging from MUC1-MUC21 that each represent their gene expressions, 11 belonging to the cell-surface associated mucins (MUC1, MUC3A, MUC3B, MUC4, MUC12, MUC13, MUC15, MUC16, MUC17, MUC20, MUC21) and 7 belonging to the subcategories of soluble mucins (MUC7, MUC9) and gel-forming (MUC2, MUC5AC, MUC5B, MUC6, MUC19).[119, 120] Both secreted and cell-surface mucins share common features, that being that they consist of up to 80% of oligosaccharide carbohydrate chains, mainly *N*-acetylgalactosamine, that can form moderate branching by *O*-glycosidic bonds to the hydroxyl group chains found on the serine and threonine amino acids protein cores.[121]

1.6.2. Mucoadhesion

Mucoadhesion is described as the ability of a material to form interfacial forces and interactions to adhere to mucosal tissue found in ocular, nasal, and oral mucous, to name a few.[118, 122] With much work and studies on mucoadhesion in recent years, it has attracted much attention to expand drug delivery systems and to fully understand the complexity of interactions. Current ophthalmic drug delivery systems are inefficient resulting in (i) poor corneal permeability, (ii) reflex blinking, (iii) tear secretion, and (iv) dosage spillage to name a few.[117] As a result, only a small percentage of the administered drug reaches the intended target, leading to a low residence time of the drug and frequent drug administration.[118] One way to circumvent this limitation is to introduce mucoadhesion. Mucoadhesion has been reported to (i) increase drug retention times, (ii) improve bioavailability, (iii) reduce drug administration frequency, and (iv) improve targeting.[123] Ocular mucoadhesion can occur by two different types of interactions; (i) electrostatic interaction between the negatively charged carboxylate groups of the sialic acid of the monomers found in the

mucins with positively charged systems and,[123] (ii) disulfide bonds between free thiol groups found within the mucins and a thiol-functionalized system.[118] In this thesis, mucoadhesion will be explored taking advantage of the disulfide bond type of interaction between the cysteine amino acids in the mucins and thiol-functionalized MOFs.

1.6.3. Periodic Acid–Schiff (PAS) Coloration Mucoadhesion Characterization

The mucoadhesive properties of MOF crystallites can be characterized by a periodic acid-schiff base coloration protocol originally proposed in 1978.[118] This quantitative study was developed to understand the level of mucoadhesive content of materials (i.e., gold nanoparticles) as well as to understand their interaction with mucins. The general reaction scheme as explained in (Figure 1.18) shows periodate oxidizing vicinal hydroxyl groups of carbohydrate molecules to aldehydes.[124] When reacted with Schiff's reagent, a pink-purple colored basic fuchsin is formed (Figure 1.18b). In parallel, the basic fuschin is decolored by the addition of sodium metabisulfite, as the central carbon atom of the triarylmethane system is no longer highly delocalized.[118, 125] Upon reaction of the decoloured fuchsin with the oxidized mucin species, the fuchsin regains its color and highly delocalized π system.[118] Followed by centrifugation upon specific protocols and UV–Vis spectroscopy, the quantification of mucins adhered to the MOF can be determined.[118]

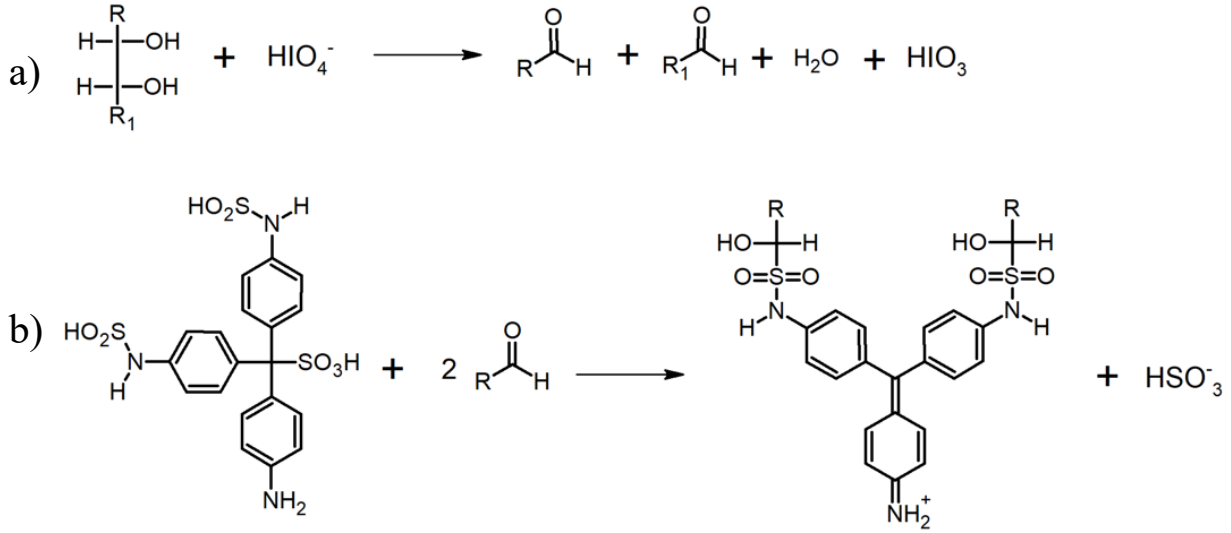

Figure 1.18. PAS coloration reaction scheme where a) represents the oxidation of hydroxyl groups by periodate, and b) represents the Schiff reagent reacts with aldehyde groups to form the fuchsin pink-purple colored compound.

1.6.4. Fluorescence Spectroscopy for Mucoadhesion Characterization

Fluorescence spectroscopy is a technique that is used to probe the mucoadhesion interaction between the cysteine amino acids within the mucins and the thiol-functionalized MOFs (Figure 1.19). A Stern-Volmer plot best describes the static and collisional quenching between the fluorescent molecules, that being the mucins and the thiolated MOFs. The interaction is plotted as a function of thiol-functionalized MOF concentration vs. relative fluorescence intensity considering the fluorescence intensity of the mucins alone and the fluorescence intensity of the mucins interacting with the thiolated MOFs. The general protocol consists of a fluorophore, being the mucins, that will emit light at 337 nm after excitation at 285 nm due to tryptophan, resulting in high fluorescence intensity.[118] The fluorescence emission is measured from 300 nm to 450 nm.[118] When MOFs are introduced, they will interact with the mucins and result in a decrease in fluorescence intensity owing to the collisional quenching that arises when the excited-state fluorophores (mucins) are deactivated when in contact with the quencher (MOFs), returning to the ground-state in a non-radiative process.[118] In this thesis, fluorescence spectroscopy is used to measure the mucoadhesion of the thiolated MOFs and the cysteine amino acids of the mucins.

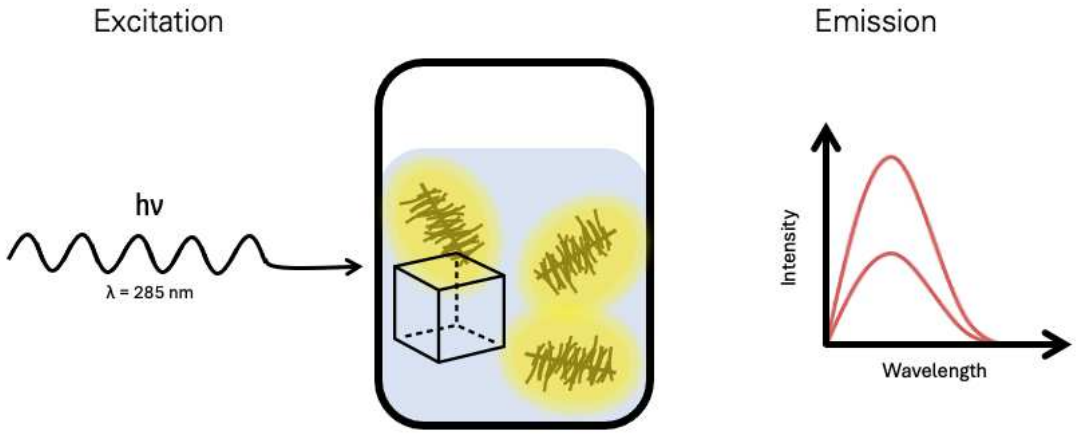

Figure 1.19. Fluorescence quenching of mucins upon interaction with MOFs (Gabrielle Raiche-Marcoux).

1.7. Scope of Thesis

The following chapters of this thesis will focus on the design and synthesis of MOFs for their potential application in ophthalmic drug delivery. The general scope of both thesis chapters

aims to discuss and provide insight into (i) the synthesis and characterization of nanosized thiol-functionalized Zr-based MOFs, and (ii) their mucoadhesive properties with the goal to develop a better shuttle for ophthalmic drug delivery providing slow and sustained release of the drug to the intended target.

Chapter 2 of this thesis explores the synthesis of three Zr-based MOFs; MOF-808, UiO-66, and UiO-67. All MOFs are synthesized in the nanoscale size regime under solvothermal conditions, and further washed and activated prior to characterization. The MOFs are then thiol-functionalized by a PSM process, specifically SALI using thioglycolic acid, and mercaptoundecanoic acid. The MOFs are characterized by PXRD, N_2 adsorption-desorption experiments, DLS, SEM, TEM, ^{1}H-NMR spectroscopy, and DRIFTS. The thiol-functionalized MOFs are investigated for thiol quantification by UV–Vis spectroscopy, and their interaction with mucins by PAS coloration and fluorescence spectroscopy measurements for mucoadhesion.

Chapter 3 of this thesis explores the synthesis of mixed-linker analogues of UiO-66 in the nanoscale size regime. Using BDC and 2,5-dimercaptoterephthalic acid (BDC-SH_2), mixed-linker UiO-66 analogues with a varying number of thiolated linkers are synthesized with the goal of providing insight into the number or density of thiol groups required for mucoadhesion. The MOFs are characterized by PXRD, N_2 adsorption-desorption experiments, ^{1}H-NMR spectroscopy, DLS, and SEM. The thiol-functionalized MOFs are investigated for thiol quantification by UV–Vis spectroscopy, and their interaction with mucins by PAS coloration and fluorescence spectroscopy measurements for mucoadhesion.

Chapter 2

Thiol-Functionalized Nanosized Metal–Organic Frameworks Synthesized by Solvent-Assisted Ligand Incorporation for Ophthalmic Drug Delivery

2.1. Introduction to Cataracts and the Anatomy of the Eye

The anatomy of the eye is complex as the organ has many different parts serving different purposes. Optical eye diseases include (i) glaucoma, (ii) allergic conjunctivitis, (iii) age-related macular degeneration, and (iv) cataracts, which can be responsible for vision impairment.[126] Cataracts specifically, are the leading cause of blindness with an estimated 95 million people affected worldwide.[127] Cataracts are most often described as the clouding or loss of transparency of the lens leading to vision loss (Figure 2.1).[128, 129] When the lens of the eye is clouded, the light that would normally be focused onto the lens, is now scattered, and sends a blurry image through the optic nerve and to the brain.[129] Most often caused by age-related developments between 45–50 years of age resulting from (i) protein breakdown, and (ii) damage of the fiber cell membranes, cataracts can also be caused by secondary effects – such as (i) diabetes, (ii) smoking, and (iii) alcohol consumption, as well as traumatic effects – including (i) accidents, (ii) injuries, leading to the physical damage of the lens and, (iii) hypertension – caused by the rearrangement of protein structures in the lens.[129–131]

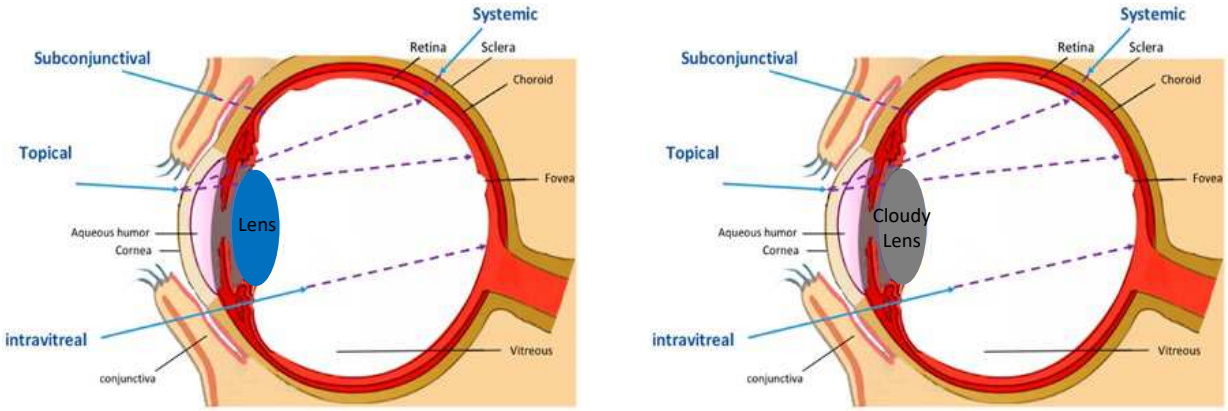

Figure 2.1. Representation of a lens with no cataracts (left) and with cataracts (right). Reprinted with permission from Li, Q.; Weng, J.; Wong, S.N.; Lee, W.Y.T.; Chow, S.F. *Mol. Pharmaceutics*. **2021**, *18*(2), 506–521. Copyright 2023 American Chemical Society.[132]

To better recognize the impact of cataracts, it is important to understand the optical design of the eye. The overall structure of the eye is divided into two segments: the anterior and the

posterior segments (Figure 2.2).[126] The anterior segment is responsible for tissues such as the (i) cornea, (ii) conjunctiva, (iii) iris, and the (iv) lens, whereas the posterior segment is where the (i) sclera, (ii) choroid and the (iii) optic nerve can be found, to name a few.[126] Most optical diseases affect both the anterior and posterior segments, with age-related macular degeneration affecting the posterior segment, and cataracts affecting the anterior segment.[126]

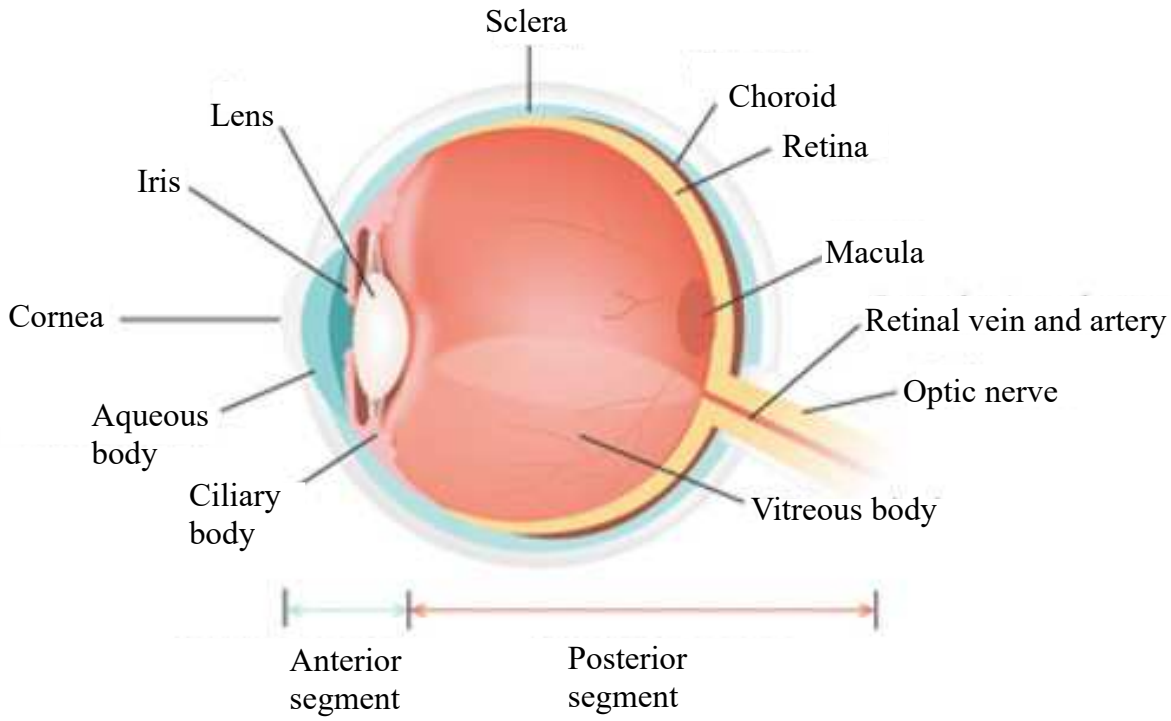

Figure 2.2. The broad division of the different structures of the eye. Reprinted with permission from Cheng, K-J.; Hsieh, C-M.; Nepali, K.; Liou, J-P. *J. Med. Chem*. **2020**, 63, 10533–10593. Copyright 2023 American Chemical Society.[133]

Made of a spherical structure, the ocular surface and front liners to the external environment are composed of the (i) cornea, (ii) conjunctiva, and the (iii) tear film.[120] The cornea is responsible for providing a barrier to external or foreign particulates, and a passageway for light to enter through to the lens. The cornea consists of five innermost layers including; (i) epithelium – the outermost layer of the cornea made of several different cells to ensure enough lubrication and prevent foreign materials from penetrating through, (ii) bowman's layer – with the primary function to provide structure and integrity to the cornea, and composed of collagen arrangements that can resist trauma events, (iii) stroma – mainly made from a mix of water and collagen, it provides the elasticity and rigidity to form the cornea, (iv) Descemet's membrane – regeneration

layer made from tissue that protects the cornea from exposure to injuries and infections, (v) endothelium – the innermost layer of the cornea that maintains overall proper stroma and Descemet's membrane functionality.[134] The second innermost layer of the eye is the iris – a thin colored and circular structure that separates the eye into the anterior and posterior segments and controls the amount of light the pupil focuses in.[135, 136] The pupil – is the main entry way for light penetration and changes its shape upon how much light enters.[136] The pupil is in direct contact with the retina in which the light focused by the pupil will be translated into electrical signals in order for the brain to understand it as an image.[136] The sclera – represents the white elastic region of the eye encompassing the circular shape of the eye.[134] The lens located behind the iris, is an elastic and transparent organ composed of proteins and water that allows penetration of light to obtain clear images at various distances.[137] However, in the event that a cataract is present, the clouding of the lens will result and scatter the light instead, leading to a blurry image.[129] A cataract can develop in any one of the following forms and areas; (i) nuclear cataract – results in a yellow and brown pigmented nucleus at the center of the lens, (ii) cortical cataract – a wedge-like cataract surrounding the lens, and (iii) posterior capsular cataract – a rapidly developing cataract located at the back of the lens.[129]

Several cataract surgeries are administered every year where topical treatments in the form of eye drop formulations have become the most widely preferred drug administration post-cataract surgery. Accounting for more than 90% of ophthalmic formulations, topical treatments are non-invasive with ease of manipulation, and high patient compliance.[126] Typically, pre- and post-cataract surgery protocols include NSAID (non-steroidal anti-inflammatory drugs) accompanied by a corticosteroid that is applied four times daily for up to four weeks post-surgery.[138] However, owing to the current poor mucoadhesion methods and the high anatomical and physiological constraints of the eye such as (i) reflex blinking, (ii) precorneal tear clearance, (iii) corneal–epithelial barrier, and (iv) pH, this method of administration results in poor bioavailability.[127, 139] In fact, only 5% of topically administered drugs reach layers deeper than the ocular tissues and it becomes necessary to apply large doses with higher concentrations and frequent administration of the drug in order to achieve the effective therapeutic dose.[127, 140, 141]

The tear film is the first layer exposed to the environment and protects the outer mucosal surfaces of the eye, and the cornea (Figure 2.3). This thin transparent film consists of glands and tissues approximately 3 μm in thickness and 3 μL in volume with three distinct layers. The

outermost layer is the (i) lipid layer – made of different lipids and fatty acids that interact with the aqueous layer and block evaporation of tears, (ii) aqueous layer – provides oxygen, electrolytes and water to the corneal tissue and blocks any foreign guest molecules, and (iii) mucin layer – composed of proteins that provide lubrication and hydration to the ocular surface.[120, 142] Specifically, mucins consist of a large protein core with up to 80% glycosylated oligosaccharide chains exhibiting long branches and involving *O*-glycosidic bonding interactions to the protein core.[121] The protein core is further subdivided into different regions made up of amino acids, specifically with a high composition of cysteine-rich amino acids, making up >10% of the protein core.[121] These cysteine-rich domains have been shown to be involved in disulfide bond formation among interactions with thiol groups on functionalized MOFs in order to achieve mucoadhesion.

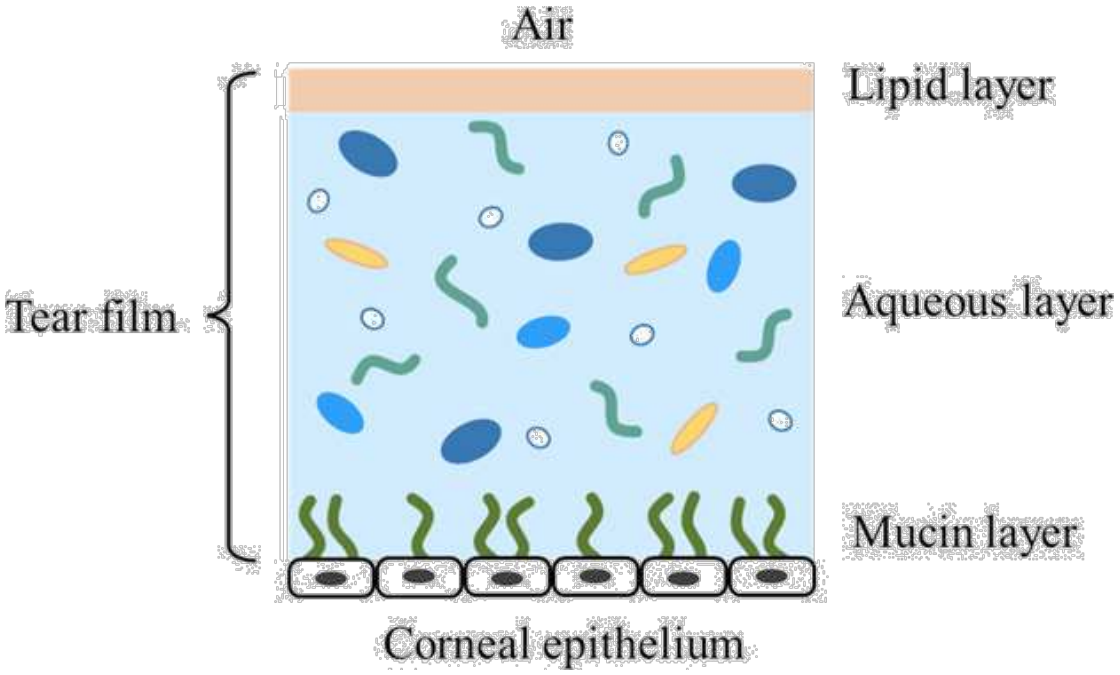

Figure 2.3. Three main layers encompassing the tear film of the eye. Reprinted with permission from Yoshida, M.; Yamaguchi, M.; Sato, A.; Tabuchi, N.; Kon, R.; limura, K-i. *Langmuir*, **2019**, 35, 8445–8451. Copyright 2023 American Chemical Society.[143]

Modern day treatments for post-cataract surgery involve the use of topical applications in the form of eye drops where anti-inflammatory drugs are immersed in saline solutions. NSAIDs for ocular treatments are used to manage ocular inflammation and have been proven to be a safe and effective tool for post-cataract surgery and routine analysis.[144] NSAIDs are composed of functional groups such as (i) salicylates, (ii) fenamates, (iii) indoles, (iv) phenyl alkanoic acids, (v)

phenyl acetic acids, and (vi) pyrazolones.[144] The role of NSAIDs is to block the cyclooxygenase (COX) enzymes (COX-1 and COX-2) that promote the production of prostaglandin which produces inflammation.[145, 146] Commercially available topical ophthalmic NSAIDs include Bromfenac, Indomethacin, Diclofenac, Flurbiprofen, and Nepafenac. Flurbiprofen is specifically effective in suppressing ocular inflammation by inhibiting the COX-1 and COX-2 enzymes owing to anti-inflammatory, and analgesic properties.[146] It is mainly used for the treatment of rheumatoid arthritis, osteoarthritis, and topically in the form of eye drops post-cataract surgery to treat ocular inflammation.[146]

Nanomaterials for ocular drug delivery systems take advantage of submicron particles ranging from 10 – 200 nm in size and provide many advantages for drug delivery such as (i) low irritation, and (ii) controlled drug release, avoiding frequent administration.[126] They exist in the form of a colloidal suspension where dispersed drug loaded nanoparticles are insoluble in aqueous solvents and are retained in the pericorneal pocket found in the cornea.[141] Nanoparticles in the form of (i) nanomicelles, (ii) liposomes, (iii) dendrimers, and (iv) gold nanoparticles (Figure 2.4),[118] have been employed, however they lack flexible structural integrity and are difficult to control the drug release leading to toxic levels of drug concentrations.[147, 148] Metal–organic frameworks (MOFs) have been studied for ocular drug delivery owing to their (i) high surface areas and porosities capable of encapsulating drug molecules, and (ii) tunable pore sizes for the controlled release of drugs.[149] Composed of inorganic metals bridged by organic polydentate ligands, they lead to the formation of highly functionalized and uniform porous structures adapted for the absorption of a variety of molecules not limited to drug delivery,[149] but gas storage and catalysis.[150, 151] Owing to the ease of post-synthetic modification of MOFs, their functionality and versatility can be adapted to satisfy the biocompatibility and bioavailability requirements for drug delivery applications. A few factors that are important for MOFs that will be studied as potential platforms for biological applications include (i) size – determine the overall speed and diffusion, and overall circulatory time *in vivo*, (ii) nature of the building blocks – metal ions and ligands, (iii) stability – metal-ligand bond strength, basicity of the ligand, coordination number, and (iv) ease of surface modification – post-synthetic modification with silica or organic polymers like polyethylene glycol (PEG) to tune the stability and ability of MOFs to circulate in aqueous media.[86]

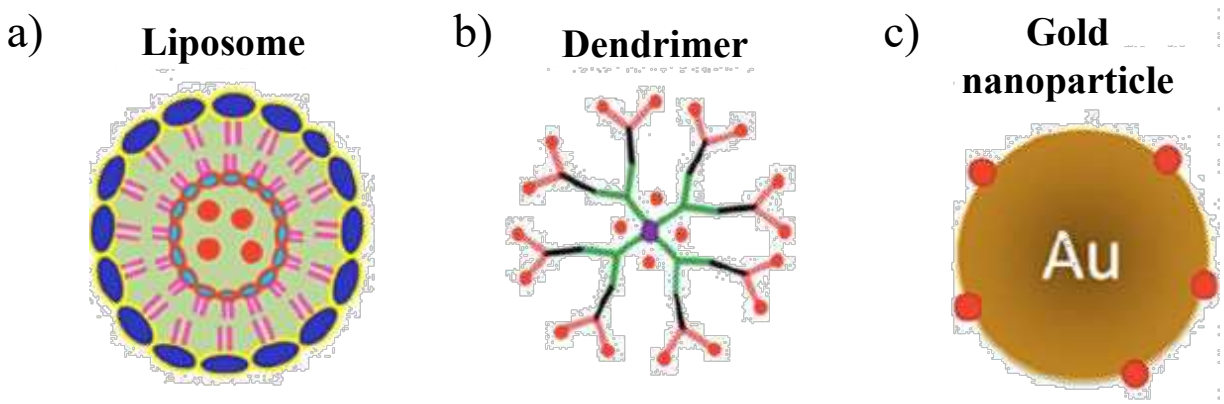

Figure 2.4. Representation of nanoparticles in the form of a) liposomes, b) dendrimers, and c) gold nanoparticles for drug delivery applications. Reprinted with permission from Zhang, Y.; Fang, F.; Li, L.; Zhang, J. *ACS Biomater. Sci. Eng*. **2020**, *6*(9), 4816–4833. Copyright 2023 American Chemical Society.[152]

The development of novel and conventional drug delivery systems with mucoadhesive properties help to (i) improve patient compliance, (ii) reduce side effects, (iii) increase retention times, and (iv) improve overall ophthalmic administration.[139] Mucoadhesion is defined as interfacial forces that form a bond with a mucosal surface for a prolonged period of time.[153] Mucins are highly glycosylated proteins located in the mucosa and allow for mucoadhesion to occur based on specific properties including (i) electrostatic interactions – mucins are negatively charged and can interact with positively-charged systems, (ii) hydrophobic interactions with the nonglycosylated protein regions,[154] and (iii) disulfide bonding – mucins consist of highly glycosylated proteins rich in thiol groups stemming from the presence of cysteine amino acids capable of bonding with thiol groups on drug vector systems. (Figure 2.5).[118]

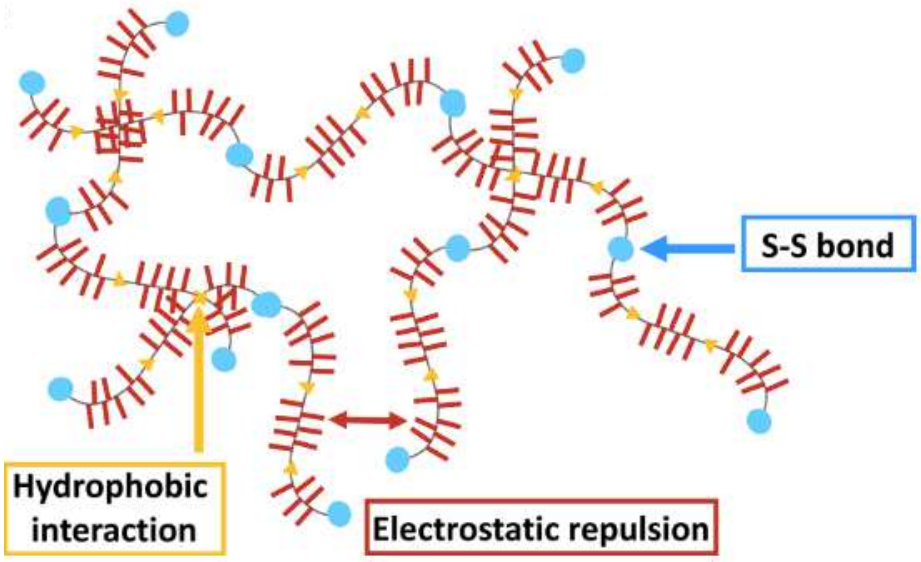

Figure 2.5. Representation of mucin glycoproteins and their potential mucoadhesive interactions. Reprinted with permission from Wagner, C.E.; Turner, B.S.; Rubinstein, M.; McKinley, G.H.; Ribbeck, K. *Biomacromolecules*, **2017**, 18, 3654–3664. Copyright 2023 American Chemical Society. [155]

The present scope encompassing the study of drug delivery systems for mucoadhesion through disulfide bonding include insights on gold nanoparticles. Owing to their multiple thiol groups present on their metallic surface and in the core, they can interact with the mucins through disulfide interactions as well as gold-sulfur bonds, giving rise to enhanced mucoadhesive interactions.[118] Gold nanoparticles have provided potential drug targeting and carrier abilities in nanomedicine, however potential toxicity of these materials owing to their intrinsic characteristics particularly associated with their physiochemical properties, require further characterization of their pharmacokinetics for drug delivery.[156]

The mucoadhesive properties of MOFs have not yet been thoroughly explored in the literature but offer an interesting alternative for mucoadhesive drug delivery systems. Previously reported mucoadhesive NH_2-MIL-88 showed encapsulation and controlled release of brimonidine for topical drug delivery through a hydrogen bonding mucoadhesive property.[149] Interaction between the hydrogen-rich ligand with the hydroxyl and carboxyl functional groups of the mucins generated a highly mucoadhesive drug vector system.[149] Preliminary research of mucoadhesion by thiolation of Zr_6-based MOFs introduced a new approach that remains novel in the field. The synthesis and characterization of bulk-size thiolated UiO-66-$(SH)_2$ and UiO-67-$(SH)_2$ was explored resulting in enhanced mucoadhesion interactions through disulfide bonding with the

mucins owing to the presence of thiols in the core and on the periphery of the MOFs.[157] However, preliminary drug delivery experiments resulted in lower drug loadings of the thiolated MOFs due to the large ionic radii of sulfur (1.84 Å) and blocking the pores for the drug uptake.[157]

Zr_6-based MOFs are of interest for this study since they are classified as some of the most stable class of MOFs reported with biocompatibility attributed to the highly oxophilic nature of the $(Zr)^{IV}$ sites.[86] In addition, polycarboxylate linkers are highly polar and permit ease of removal under physiological conditions.[86] Herein, expanding upon the previous research of Zr_6-MOFs for mucoadhesion through disulfide bonding, the development of nanosized Zr_6-MOFs will be explored to improve the biocompatibility and bioavailability properties, followed by tuning the thiol-functionality of the Zr_6-MOFs to increase the drug loading capacity with less surface thiols for potential drug delivery experiments. The alternative approach at functionalizing the Zr_6-MOFs with thiol groups is by a post-synthetic modification process known as solvent-assisted ligand incorporation (SALI). This method takes advantage of available polar -OH and $-OH_2$ ligands on the Zr_6 oxoclusters that can be exchanged with a thiol-functionalized ligand bearing a terminal carboxylate (-COOH) functional group.[34] The two thiolated ligands of interest are thioglycolic acid, and mercaptoundecanoic acid, each bearing a terminal (-SH) group that will serve to form the disulfide bridge with the cysteine amino acids in the mucins, and a terminal (-COOH) group to coordinate to the open-metal sites of the MOF (Figure 2.6).

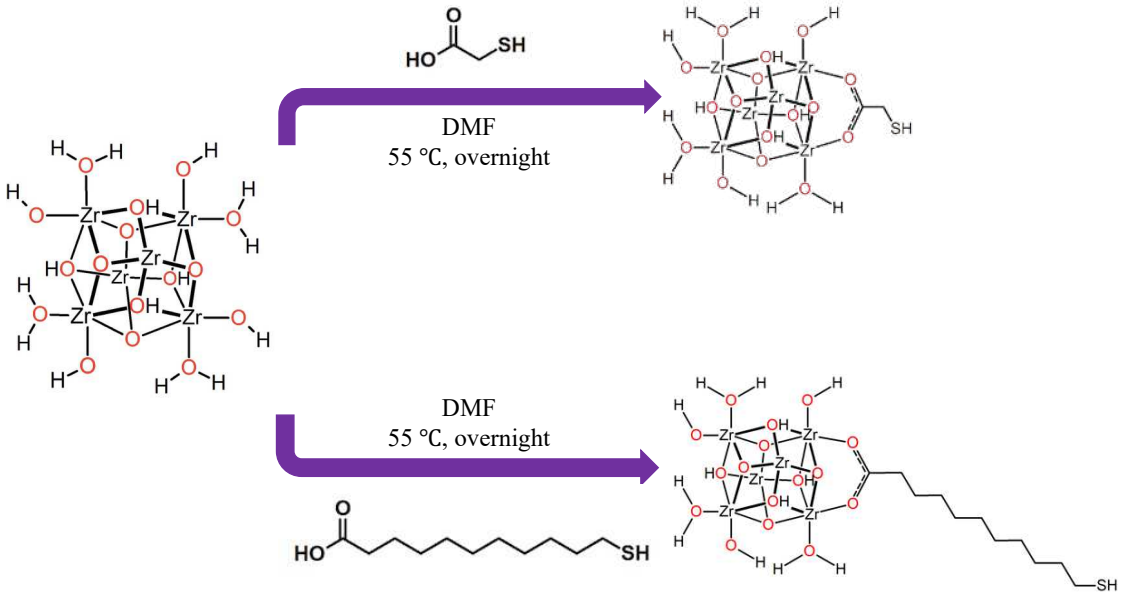

Figure 2.6. Schematic representation of solvent-assisted ligand incorporation (SALI) of Zr_6-based MOFs with thioglycolic acid (top) and mercaptoundecanoic acid (bottom).

A general representation of the mucoadhesion process can be understood from Figure 2.7, where step 1 consists of the topical application of the Flurbiprofen drug loaded SALI MOF sample administered onto the surface of the cornea, followed by step 2 – mucoadhesion by the interaction between the thiol group from the thiolated ligand of the MOF forming a disulfide bridge with the cysteine amino acids found in the mucous layer, and step 3 – Flurbiprofen drug release into the cornea and into the epithelium layers until it reaches the anterior chamber where it exerts its pharmacological function.

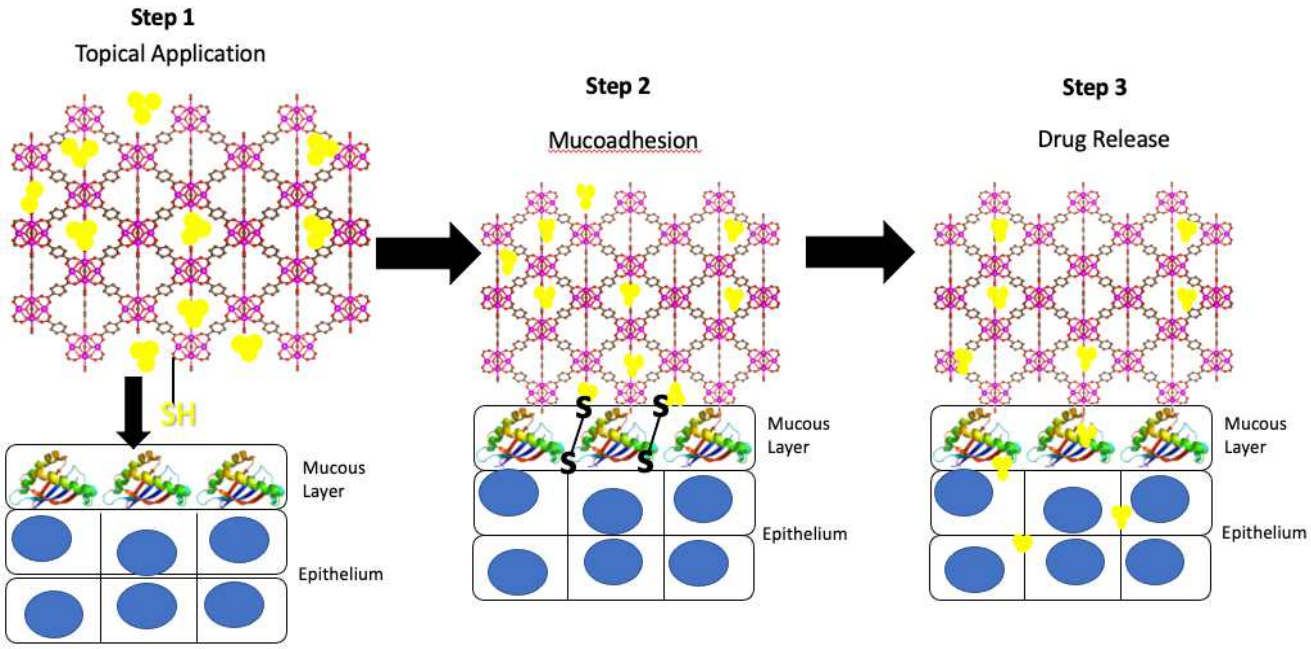

Figure 2.7. Mucoadhesion topical application process involving drug loaded MOF samples interacting with the mucins in the mucous layer by forming a disulfide bond and resulting in the drug release.

This study aims to develop a series of Zr_6-based MOFs; MOF-808, UiO-66, and UiO-67, that are synthesized in the nanoscale size regime and thiol functionalized through post-synthetic modification using SALI in order to assess their mucoadhesive properties as characterized by colorimetric quantification and fluorescence spectroscopy.

2.2. Experimental Procedure

2.2.1 Materials and Chemicals

All chemicals were purchased from commercial suppliers and used with no further purification. Zirconium (IV) chloride ($ZrCl_4$; Alfa Aesar, 99.5%), glacial acetic acid (Fisher Scientific, 99.7%), isopropanol (Sigma-Aldrich, 99.5%), formic acid (Thermo Scientific, 97%), 1,3,5-benzenetricarboxylic acid (BTC; Alfa Aesar, 98%), terephthalic acid (BDC; Acros Organics, 99.5+%), *N,N*-dimethylformamide (DMF; Fisher Chemical Certified ACS, ≥99.8%), 4,4-biphenyldicarboxylic acid (BPDC; Acros Organics, 98%), zirconium dichloride oxide hydrate ($ZrOCl_2$; Alfa Aesar, 99.9%), thioglycolic acid (Tokyo Chemical Industry, > 95%), mercaptoundecanoic acid (Ambeed, 98%), acetone (Fischer Chemical Certified ACS, 99.5%), deuterated sulfuric acid (D_2SO_4; Sigma-Aldrich, 99-98 wt%), deuterated dimethyl sulfoxide (DMSO-d_6; Cambridge Isotope Laboratories, 99.8% D with 0.05% v/v tetramethysilane (TMS)), sodium acetate (Sigma-Aldrich, ≥99.9%), Tris (Tris(Hydroxymethyl) Aminomethane) (Acros Organics, +99%), N-acetyl-L-cysteine (Alfa Aesar, 98+%), and 5,5-dithiobis(2-nitrobenzoic acid) (Alfa Aesar, 99%).

2.2.2. General Methods

Powder X-ray diffraction (PXRD) results were collected using a Rigaku Miniflex or a Bruker D2 Phaser (Bruker AXS, Madison, WI, USA) both equipped with a Cu-based (Kα) X-ray source and a nickel filter. The dry powdered samples were packed into a smooth layer onto a silicon wafer zero-background sample holder. Results were collected from 4-40° at 0.02 θ increments in the 2θ-range.

N_2 adsorption-desorption experiments were conducted on a Micromeritics Tristar II Plus instrument equipped with a nitrogen dewar filled with liquid nitrogen at 77 K to obtain surface area and porosity results. A Micromeritics SmartVac prep with a hybrid turbo vacuum pump was used prior to BET analysis to activate the samples at 120 ℃ for 24 h under vacuum conditions.

Dynamic light scattering (DLS) size distribution profiles were collected with a Malvern Panalytical Zetasizer Nano ZSP instrument at 25 ℃. The MOF samples were sonicated in 18-ohm MilliQ pore water, followed by dilutions with 500 μL aliquots of the MOF suspension in 1.5 mL

of MilliQ pore water. The samples were analyzed in a quartz cuvette with 1 cm path length and 3.50 mL capacity.

Proton nuclear magnetic resonance (^{1}H-NMR) spectra were obtained on a 500 MHz Bruker spectrometer instrument equipped with a Topsin software system. The samples were digested and sonicated with ~ 6 drops of deuterated sulfuric acid, followed by 600 μL of DMSO-d_6. The samples were analyzed at 1024 scans and referenced to the residual solvent peaks.

Diffuse reflectance infrared Fourier transform spectroscopy (DRIFTS) spectra were collected with a Thermo Scientific Nicolet 6700 FT-IR equipped with an MCT detector and resolution of 1 cm^{-1} from 400-8000 cm^{-1} wavelength range. The MOF samples were vacuum dried at 90 ℃ prior to DRIFTS analysis to avoid measuring solvent peaks and were further suspended with dry KBr pellets for analysis.

Ultraviolet–visible (UV–Vis) absorption analysis was conducted on a Cary 5000 series UV–Vis NIR spectrophotometer from Agilent technologies. The solutions were analyzed using dual beam mode from 200-800 nm and a source changeover wavelength at 350 nm. A two-sided quartz cuvette with a 1 cm path length and maximum volume of 3.50 mL capacity was used to measure the sample solutions.

Scanning electron microscopy (SEM) micrographs were collected on a Phenom ProX SEM benchtop at 12 kV. All samples were first sputter coated with a 5 mm gold (Au) layer by using a Cressington 108 Auto/SE Sputter Coater with MTM-20 high resolution film thickness controller.

Transmission electron microscopy (TEM) micrographs were collected on a Talos ™ L120C TEM. All samples were first suspended in acetone, sonicated, and 10 μL of the solution was dropcast onto a carbon grid.

Thiol Quantification with Ellman's Test: A 1M TRIS Buffer solution was prepared in a volumetric flask with TRIS base (12.220 g, 101 mmol) and MQ H_2O. The pH of the solution was adjusted to 8.0 by adding hydrochloric acid and further diluted to 100 mL. A 50 mM sodium acetate solution was prepared in a 100 mL volumetric flask by adding sodium acetate (0.4101 g, 5.0 mmol) and MQ H_2O. The pH was adjusted to ~ 4-5 by addition with acetic acid (93.5 μL) and further diluted to 100 mL. The 5,5'-dithiobis(2-nitrobenzoic acid) (DTNB) reagent was prepared

by dissolving 8.50 mg (0.0214 mmol) of DNTB in 10 mL of sodium acetate (50 mM) in a 10 mL volumetric flask. The solution was then sonicated and stored in the fridge. The Ellman's test was followed according to previously reported methods.[158] A calibration curve was prepared with a known N-acetyl-L-cysteine standard starting at 0 μM. The standard samples were prepared by mixing 150 μL of DTNB reagent, 300 μL of TRIS buffer, 2520 μL of MQ H_2O, and 30 μL of N-acetyl-L-cysteine standard for a total cuvette volume of 3000 μL. A calibration curve was prepared with concentrations of standard from 0-60 μM, with 0 μM attributed to the blank with just MQ H_2O. The solution was mixed and incubated for 5 mins at room temperature. Once the yellow colour of the solution was produced, the cuvette was placed into the UV spectrophotometer and the optical absorbance was measured at 400 nm. The UV–Vis was blanked with each sample in between runs.

2.2.3. Synthesis and Activation of nanosized Zr_6-based MOFs (MOF-808, UiO-66, and UiO-67)

Nanosized MOF-808

Nanosized MOF-808 was synthesized according to an already published procedure.[46] Briefly, Zr_6 oxoclusters were prepared in a scintillation vial with the addition of $ZrCl_4$ (1000 mg, 4.29 mmol) added to a mixture of 1.5 mL of acetic acid and 2.5 mL of isopropanol. Once all reagents were added, the solution was heated at 120 ℃ with constant stirring at 500 rpm on a standard hot plate for 60 mins. The white powdered product was collected by centrifugation at 7800 rpm for 8 mins and the suspension was washed with acetone 2x. The product was then placed in a vacuum oven at 80 ℃ for 60 mins.

Following the Zr_6 oxocluster synthesis, nanosized MOF-808 (210 nm) was prepared in a scintillation vial with the addition of Zr_6 oxoclusters (120 mg, 0.515 mmol) dispersed in 300 μL of formic acid while stirring at 600 rpm. 500 μL of distilled water was subsequently added, and the solution turned colorless. 1,3,5-benzentricarboxylic acid (30 mg, 0.14 mmol) was added to the reaction mixture and was left stirring at 600 rpm overnight at room temperature. The white powdered product was collected by centrifugation at 7500 rpm for 5 mins and the suspension was washed with 5 mL of distilled water 3x, followed by 5 mL of acetone 3x, and was left to soak overnight. The product was left to dry in a vacuum oven at 80 ℃ for 2 h. The sample was soaked

in dilute HCl (0.1 M, 9 mL) overnight to remove excess formate ions on the surface and pores of the MOF. The sample was washed with 5 mL of distilled water 3x, followed by 5 mL of acetone 3x, and was left to soak overnight, and further placed to dry in a vacuum oven at 80 ℃ for 2 h.

Nanosized UiO-66

Nanosized UiO-66 was synthesized under solvothermal conditions in an 8-dram vial containing $ZrCl_4$ (31.0 mg, 0.133 mmol) and the addition of H_2BDC (31.3 mg, 0.188 mmol), with 7.5 mL of DMF and 250 μL of acetic acid. The sample mixture was sonicated until a white homogeneous solution was formed and the sample was placed in a 120 ℃ oven for 24 h. The white gel-like product was collected by centrifugation at 7500 rpm for 5 mins, and washed with 5 mL of DMF 3x for 3 subsequent days with soakings overnight, followed by 5 mL of acetone 3x for 3 subsequent days with soakings overnight. The sample was dried in a vacuum oven at 80 ℃ for 1 h.

Nanosized UiO-67

Nanosized UiO-67 was synthesized under solvothermal conditions by preparing two separate solutions in 8-dram vials: solution A consisting of H_2BPDC (40 mg, 0.165 mmol) and 2 mL of DMF.[159] Solution A was sonicated until a white suspension was formed. Solution B consisted of $ZrOCl_2 \bullet 8H_2O$ (18 mg, 0.055 mmol) and 6 mL of DMF, followed by sonication. The two solutions were combined into an 8-dram vial and 96.55 μL of acetic acid was subsequently added. The reaction mixture was sonicated and placed into a 90 ℃ oven for 18 h. The white transparent gel-like product was collected by centrifugation at 7500 rpm for 5 mins and washed with 5 mL of DMF 3x for 3 subsequent days with soakings overnight, followed by 5 mL of acetone 3x for 3 subsequent days with soakings overnight. The sample was dried in a vacuum oven at 80 ℃ for 1 h.

2.2.4. Postsynthetic Modification of Zr_6-based MOFs (MOF-808, UiO-66, UiO-67)

MOF-808 SALI

The SALI approach for the post-synthetic modification of nanosized MOF-808 with thioglycolic acid consisted of weighing out 45 mg of activated MOF-808 (0.0330 mmol) in a scintillation vial. Subsequently, 15 equivalents of thioglycolic acid (34.54 μL, 0.49497 mmol) was

added to the vial, followed by the addition of DMF (12 mL). The reaction mixture was capped and heated at 55 ℃ overnight with stirring. The product was centrifuged at 7500 rpm for 5 mins and washed with 5 mL of DMF 3x for 3 subsequent days with soakings overnight, followed by 5 mL of acetone 3x for 3 subsequent days with soakings overnight.

Additionally, the same approach was used to synthesize MOF-808 with mercaptoundecanoic acid. A 45 mg portion of activated MOF-808 (0.0330 mmol) was mixed with 15 equivalents of mercaptoundecanoic acid (108.08 mg, 0.49497 mmol), followed by 12 mL of DMF. The reaction mixture was capped and heated at 55 ℃ overnight with stirring. The product was centrifuged at 7500 rpm for 5 mins and washed with 5 mL of DMF 3x for 3 subsequent days with soakings overnight, followed by 5 mL of acetone 3x for 3 subsequent days with soakings overnight.

UiO-66 SALI

SALI was performed on nanosized UiO-66 with both thioglycolic acid and mercaptoundecanoic using similar procedures. A 45 mg portion of activated UiO-66 (0.0270 mmol) was mixed with 15 equivalents of thioglycolic acid (28.30 μL, 0.0374 mmol) and separately mercaptoundecanoic acid (88.57 mg, 0.4056 mmol), followed by 12 mL of DMF in each separate vial. The reaction mixture was capped and heated at 55 ℃ overnight with stirring. The product was centrifuged at 7500 rpm for 5 mins and washed with 5 mL of DMF 3x for 3 subsequent days with soakings overnight, followed by 5 mL of acetone 3x for 3 subsequent days with soakings overnight.

UiO-67 SALI

SALI was performed on nanosized UiO-67 with both thioglycolic acid and mercaptoundecanoic using similar procedures. A 45 mg portion of activated UiO-67 (0.0212 mmol) was mixed with 15 equivalents of thioglycolic acid (38.28 μL, 0.318 mmol) and separately mercaptoundecanoic acid (69.50 mg, 0.318 mmol), followed by 12 mL of DMF in each separate vial. The reaction mixture was capped and heated at 55 ℃ overnight with stirring. The product was centrifuged at 7500 rpm for 5 mins and washed with 5 mL of DMF 3x for 3 subsequent days with soakings overnight, followed by 5 mL of acetone 3x for 3 subsequent days with soakings overnight.

2.3. Results and Discussion

2.3.1. Characterization of Nanosized MOFs

Zr_6-based MOFs, notably MOF-808, UiO-66 and UiO-67, have been selected for this study to evaluate how nanosizing the MOFs and post-synthetically modifying them using SALI affects their mucoadhesive properties. Nanosized Zr_6-based MOFs were synthesized according to literature procedures.[45, 159] The size reduction of the resulting materials compared to standard Zr_6-based MOF synthetic procedures is attributed to the faster reaction kinetics that occur when using lower concentrations of modulator.[72] As such, with lower amounts of modulator present, the metal and linkers in solution will be quickly depleted owing to faster nucleation, and providing the opportunity to grow a large number of nanoparticles at the same time and with a homogeneous size distribution.[160] In addition, shortening the reaction time will decrease the overall crystal growth of the MOF as nucleation will reach a saturation point.[161] Owing to the low amounts of modulator implemented in each Zr_6-based MOF procedure, the resulting mixture exhibited a gel-like product owing to the weak non-covalent interactions that occur between the aggregates of the nanoparticles.[162] PXRD determines the bulk crystallinity and phase purity of the MOFs, confirming the successful synthesis of the nanosized MOFs according to the allowed reflections from the simulated patterns (Figure 2.8a, c, e). The respective N_2 adsorption-desorption isotherms for all MOFs are shown, collected at 77 K after activation of samples at 120 ℃ for 24 h under vacuum (Figure 2.8b, d, f). N_2 sorption analysis for MOF-808 reveals that the material has a surface area of 1700 m^2g^{-1} with a reversible Type I(b) isotherm following the Brunaeur-Emmett Teller (BET) analysis, confirming micropores nearing the size of mesopores. Additionally, the N_2 sorption analysis for UiO-66 and UiO-67 showcase a reversible Type I(a) isotherm, confirming micropore sizes with surface areas of 1270 m^2g^{-1}, and 1900 m^2g^{-1}, respectively.

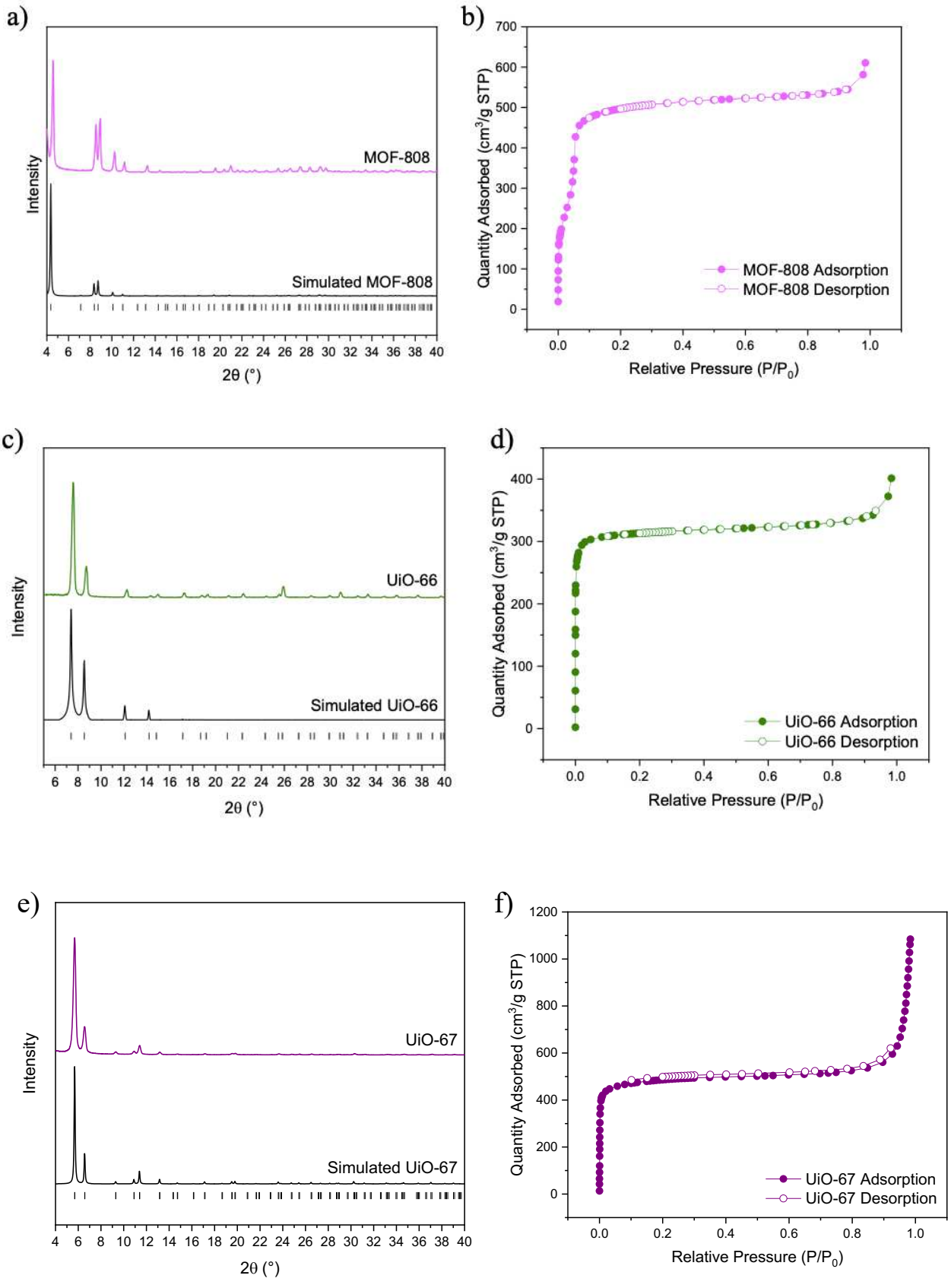
a)
Intensity
MOF-808
Simulated MOF-808
4 6 8 10 12 14 16 18 20 22 24 26 28 30 32 34 36 38 40
2θ (°)
b)
Quantity Adsorbed (cm3/g STP)
0 100 200 300 400 500 600 700
MOF-808 Adsorption
MOF-808 Desorption
0.0 0.2 0.4 0.6 0.8 1.0
Relative Pressure (P/P0)
c)
Intensity
UiO-66
Simulated UiO-66
6 8 10 12 14 16 18 20 22 24 26 28 30 32 34 36 38 40
2θ (°)
d)
Quantity Adsorbed (cm3/g STP)
0 100 200 300 400
UiO-66 Adsorption
UiO-66 Desorption
0.0 0.2 0.4 0.6 0.8 1.0
Relative Pressure (P/P0)
e)
Intensity
UiO-67
Simulated UiO-67
4 6 8 10 12 14 16 18 20 22 24 26 28 30 32 34 36 38 40
2θ (°)
f)
Quantity Adsorbed (cm3/g STP)
0 200 400 600 800 1000 1200
UiO-67 Adsorption
UiO-67 Desorption
0.0 0.2 0.4 0.6 0.8 1.0
Relative Pressure (P/P0)

Figure 2.8. PXRD diffractograms of (a) MOF-808, (c) UiO-66, and (e) UiO-67. N_2 adsorption-desorption isotherms for (b) MOF-808, (d) UiO-66, and (f) UiO-67.

DLS measurements were carried out to confirm the hydrodynamic particle size of each MOF sample in solution (Figure 2.9a, c, e). The solutions were prepared in MQ water owing to the stability of Zr_6-based MOFs in water and it's universal solvent role for biological conditions owing to its high polarity for cell transport.[163] The particle sizes based on DLS measurements are 310 nm, 212 nm, and 171 nm, respectively for MOF-808, UiO-66 and UiO-67. An SEM micrograph for MOF-808 (Figure 2.9b) was obtained to determine and compare the static crystallite size, which averages 286 nm. In addition, TEM micrographs were obtained for UiO-66 and UiO-67 (Figure 2.9d, f), resulting in static crystallite sizes averaging 62 nm and 39 nm, respectively. Comparison of SEM and TEM micrographs with the polydispersity index (PDI) of the DLS plots reveal that MOF-808 and UiO-66 are monodisperse and highly regular. Alternatively, the UiO-67 PDI is higher, further confirmed by a more aggregated sample distribution observed using TEM. It can be hypothesized that the difference in nanoparticle aggregation can arise due to the increase in surface defects, and unsaturated metal and linker sites, resulting in high surface energies that can favor aggregation.[164, 165] DLS results for all samples show a higher average particle size owing to the hydrodynamic layer being measured, taking into account the surrounding hydration layer of the particles diffusing in the solvent. Complete particle size statistical analysis for all nanosized MOFs can be referenced in the appendix (Figure A.1a-i).

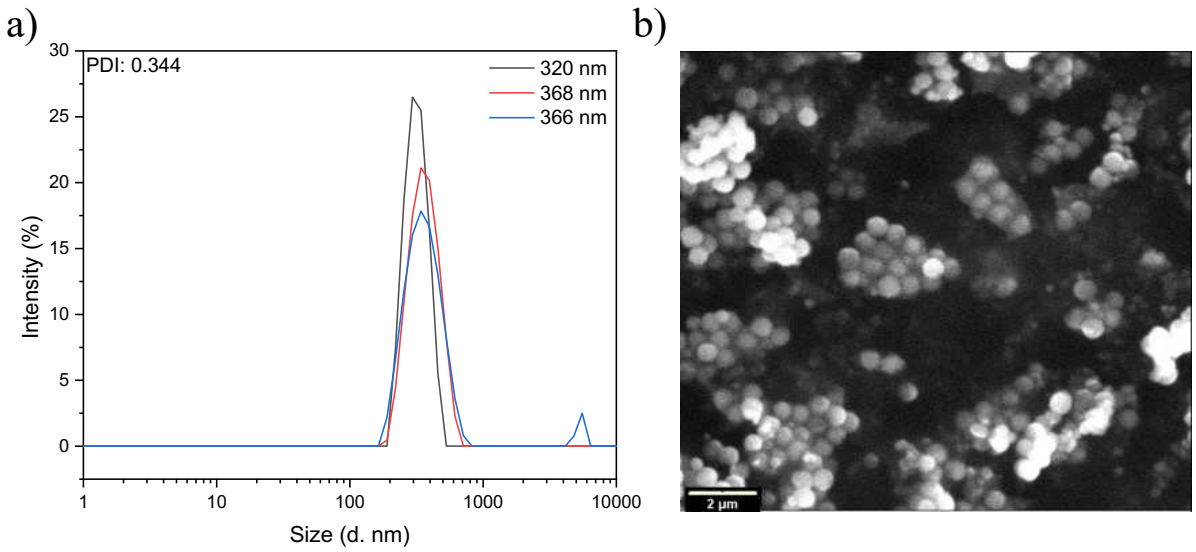

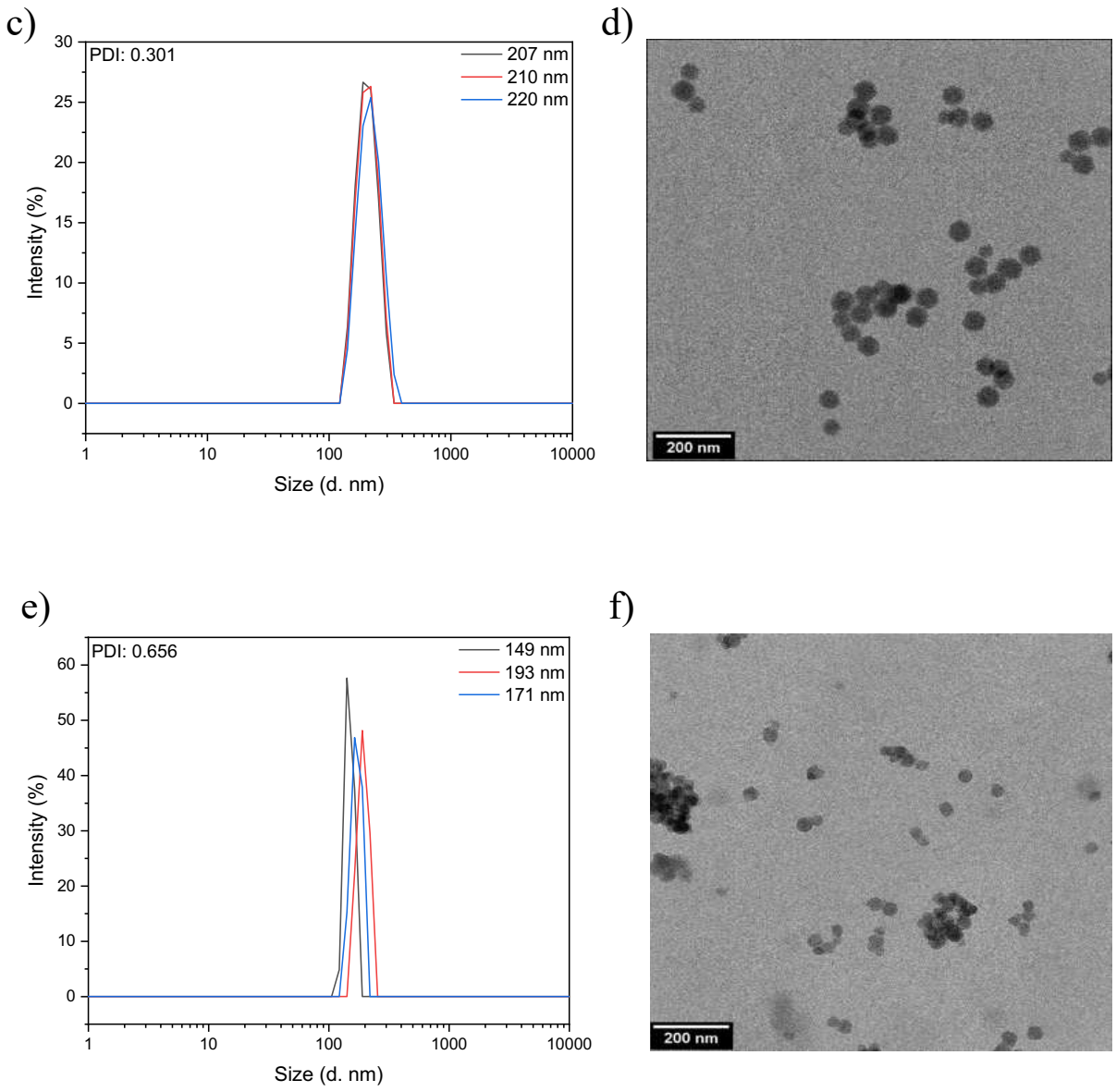

Figure 2.9. DLS measurements of (a) MOF-808, (c) UiO-66, and (e) UiO-67. SEM micrograph of (b) MOF-808, and TEM micrographs of (d) UiO-66, and (f) UiO-67.

2.3.2. Characterization of Post-Synthetically Modified Nanosized MOFs

Once the nanosized Zr_6-based MOFs were synthesized and characterized, the nanoMOFs were then post-synthetically functionalized using SALI with two thiol-containing ligands; thioglycolic acid, and mercaptoundecanoic acid. In order to confirm the presence of these ligands on the open-metal sites of the MOFs, further characterization techniques were performed. Figure

2.10 showcases PXRD diffractograms of the MOFs with both ligands incorporated post-synthetically and confirms that the structural integrity of the MOFs are maintained. In addition, the N_2 adsorption-desorption experiments were also conducted to determine the surface areas of the post-synthetically modified MOFs. The MOFs with thioglycolic acid ligands featured surface areas of 1780 m^2g^{-1} for MOF-808, 1190 m^2g^{-1} for UiO-66, and 2300 m^2g^{-1} for UiO-67. When mercaptoundecanoic acid is incorporated in the MOFs, the surface areas are 990 m^2g^{-1} for MOF-808, 1090 m^2g^{-1} for UiO-66, and 2160 m^2g^{-1} for UiO-67. As presented, the surface areas are higher for the MOFs with thioglycolic acid compared to the control MOFs without any ligands added post-synthetically, and lower for the MOFs with mercaptoundecanoic acid. This trend is what we would expect to observe since thioglycolic acid is smaller and lighter in mass, hence allowing for slightly more surface area while not significantly occluding accessibility of the pores. Compared with mercaptoundecanoic acid, a longer chain and heavier in mass, we would expect to see lower surface areas as the large linkers can significantly block access to the MOF pores. In addition, it is observed that some of the MOF surface areas are higher than the parent MOF which can be attributed to the possibility of introducing defects or displacing the linkers when incorporating thiolated ligands via SALI.

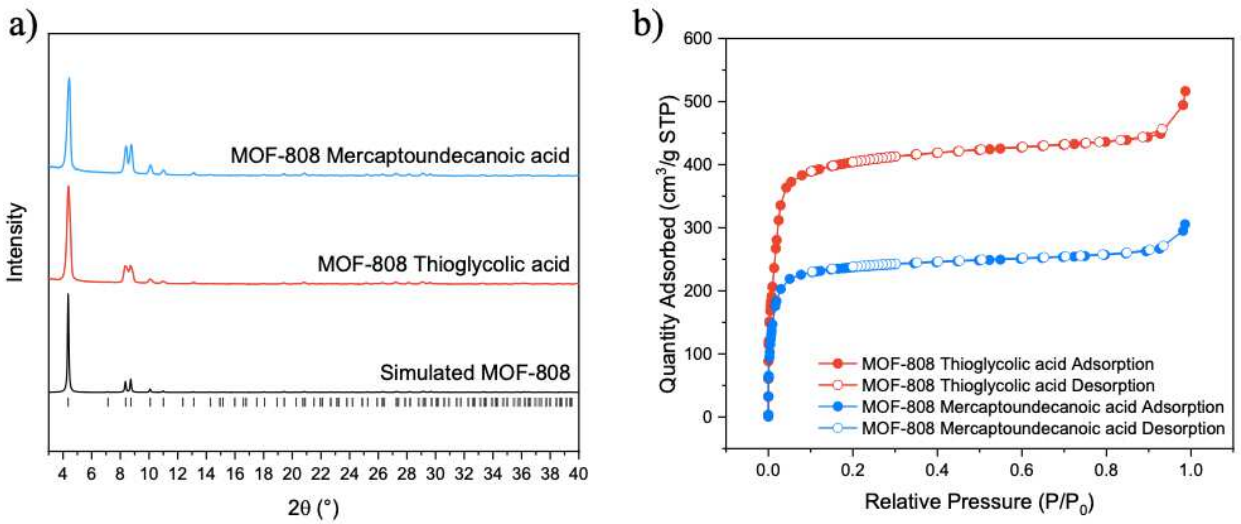

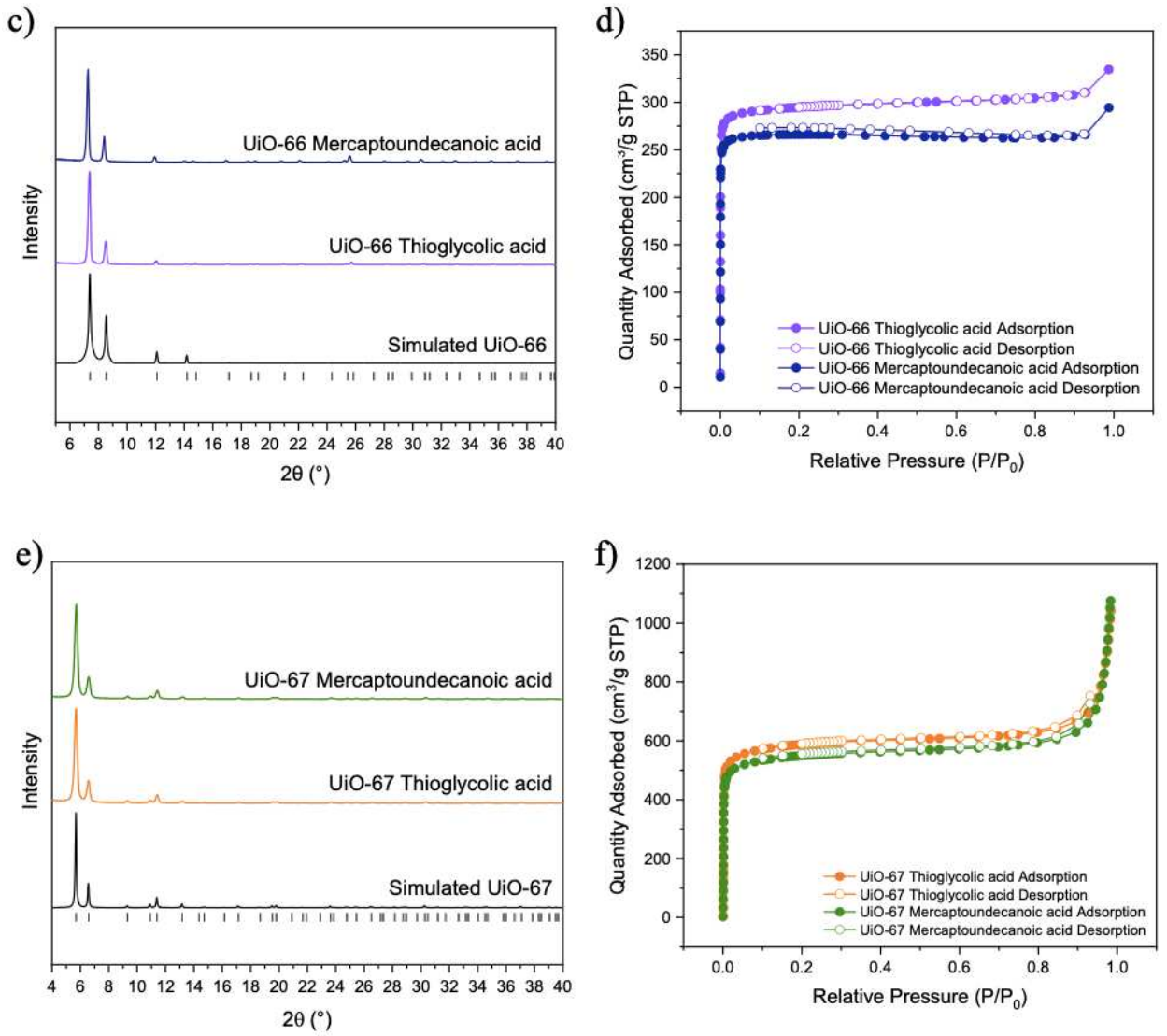

Figure 2.10. PXRD diffractograms with thioglycolic acid and mercaptoundecanoic acid for a) MOF-808, c) UiO-66, and e) UiO-67, followed by N_2 adsorption-desorption isotherms with thioglycolic acid and mercaptoundecanoic acid for b) MOF-808, d) UiO-66, and f) UiO-67.

Diffuse reflectance infrared Fourier transform spectroscopy (DRIFTS) was used to determine IR active functional groups present on the surface and inside the pores of the MOFs. Figure 2.11 showcases DRIFTS spectra for MOF-808, UiO-66, and UiO-67 with the expected absorption bands. The sharp stretches at 3671 cm^{-1} and 3674 cm^{-1} corresponds to the bridging and terminal -OH from the Zr_6 metal node, respectively. The stretches at 1395 cm^{-1} and 1590 cm^{-1} are attributed to the symmetric and asymmetric vibrations from the -C=O organic linker, while the asymmetric and symmetric $-CH_3$ and $-CH_2$ stretches of the organic linker appear in the region of

2900 cm^{-1}. The coordinated ligands to the metal nodes can be confirmed by the attenuated peaks of the terminal or bridging hydroxyls, indicating that portions of the metal node are functionalized by the carboxylates of the thiolated ligands.[41] However, residual intensity can be evidence of unfunctionalized hydroxyl and aqua ligands at the metal node termini.[38]

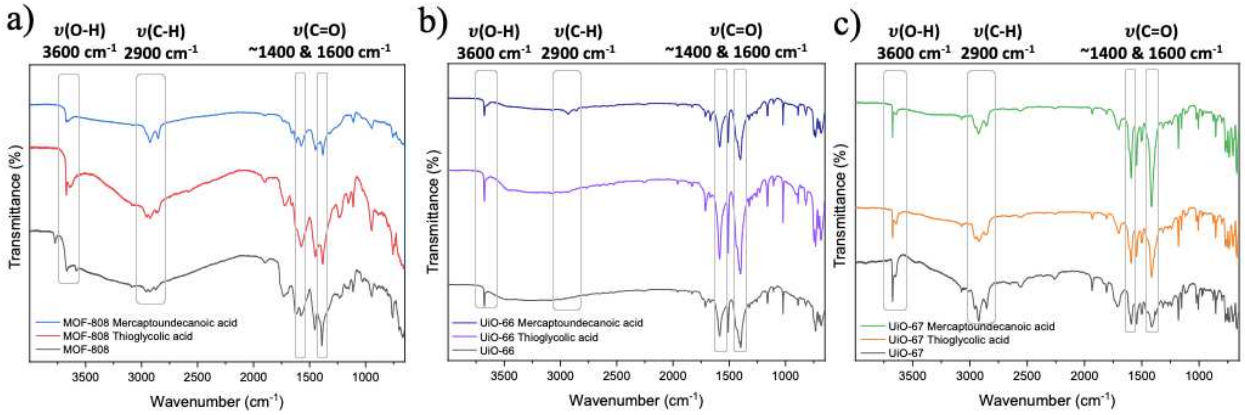

Figure 2.11. DRIFTS spectra for a) MOF-808, b) UiO-66, and c) UiO-67.

Proton nuclear magnetic resonance (^{1}H-NMR) spectroscopy of the digested post-synthetically modified MOF samples show structural organic linker purity and incorporation of the thiolated ligands into the MOFs. ^{1}H-NMR spectroscopy can also be used to quantify the amount of thiolated ligand per metal node of the MOF (Figure 2.12). All ^{1}H-NMR spectra integrations were set for the total number of protons for each structural organic linker per metal node of the MOF. ^{1}H-NMR spectra of just the thioglycolic acid and mercaptoundecanoic acid digested with sulfuric acid and further dissolved in DMSO was obtained to confirm the chemical shifts of the ligands (Figure A.5a, b). Figure 2.12a, b represent the ^{1}H-NMR spectra for MOF-808 with incorporations of 2.2 and 4.9 for thioglycolic acid and mercaptoundecanoic acid per Zr_6-node, respectively. It was hypothesized that less mercaptoundecanoic acid would be coordinated into MOF-808 compared to thioglycolic acid due to its longer ligand size. It is possible that excess mercaptoundecanoic acid ligand was not thoroughly washed out during the washing steps. Additionally, (Figure 2.12c, d) represents the ^{1}H-NMR spectra for UiO-66 thioglycolic acid and mercaptoundecanoic acid with incorporations of 0.28 and 0.36 per Zr_6-node, respectively, and UiO-67 (Figure 2.12e, f) with incorporations of 1.2 and 1.7, respectively. Similar to MOF-808, it was hypothesized that more thioglycolic acid would be coordinated into the MOFs compared to mercaptoundecanoic acid since the pores of the UiO-66 and UiO-67 are too small for the

mercaptoundecanoic acid to be coordinated. In addition to requiring more thorough washings, it is possible that the MOFs are becoming more defective when the thiolated ligands are incorporated as some of the MOF linkers can be displaced when new ligands are incorporated. It is expected to observe lower incorporations for the post-synthetically modified ligands in UiO-66 and UiO-67 when compared to MOF-808, attributed to the lower abundance of open-metal sites in the UiO-MOFs, which are only located at defect sites.[166, 167]

a)

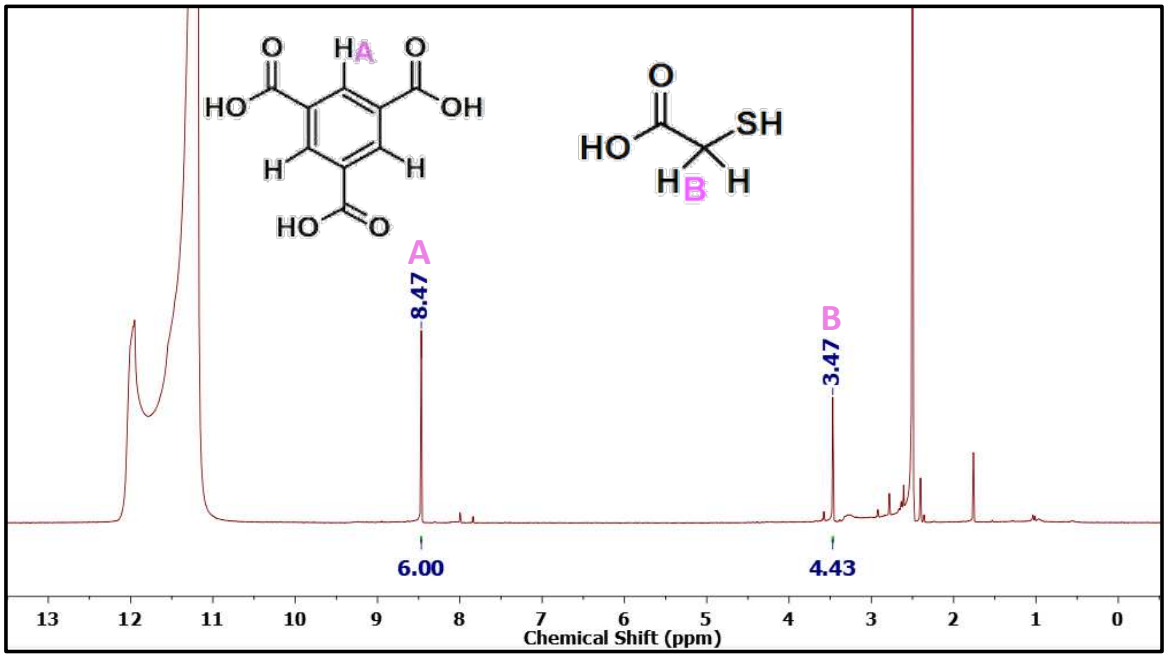

b)

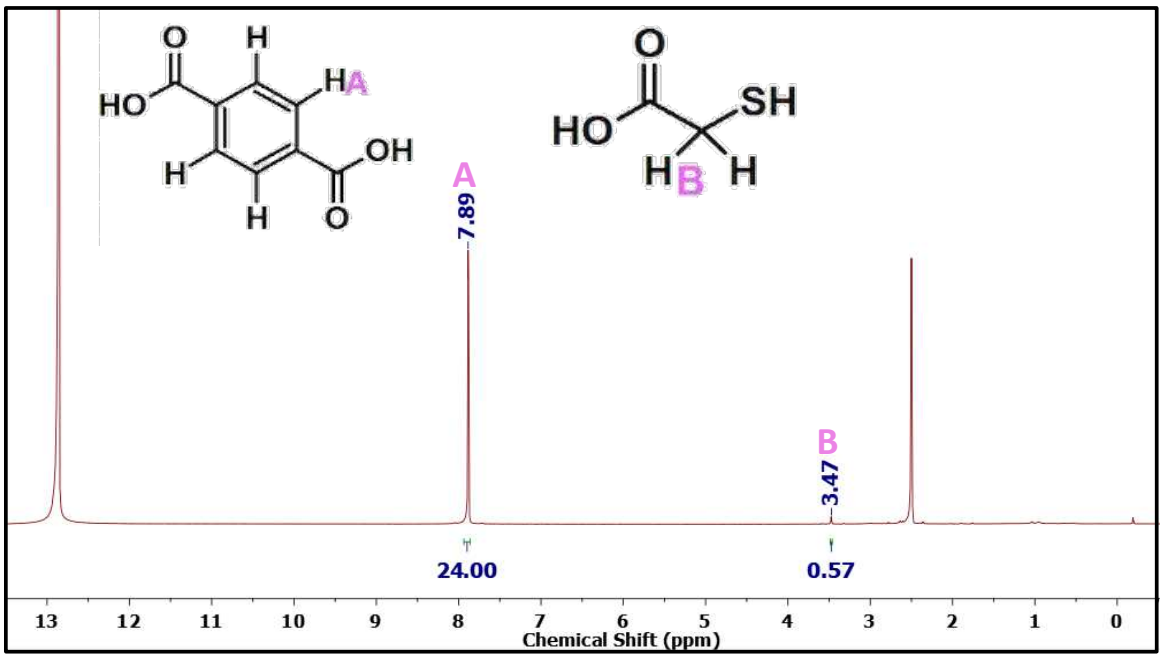
HO
O
H
HA
OH
O
H
H
HO
O
SH
HB
H
A
7.89
B
3.47
24.00
0.57
13 12 11 10 9 8 7 6 5 4 3 2 1 0
Chemical Shift (ppm)

c)

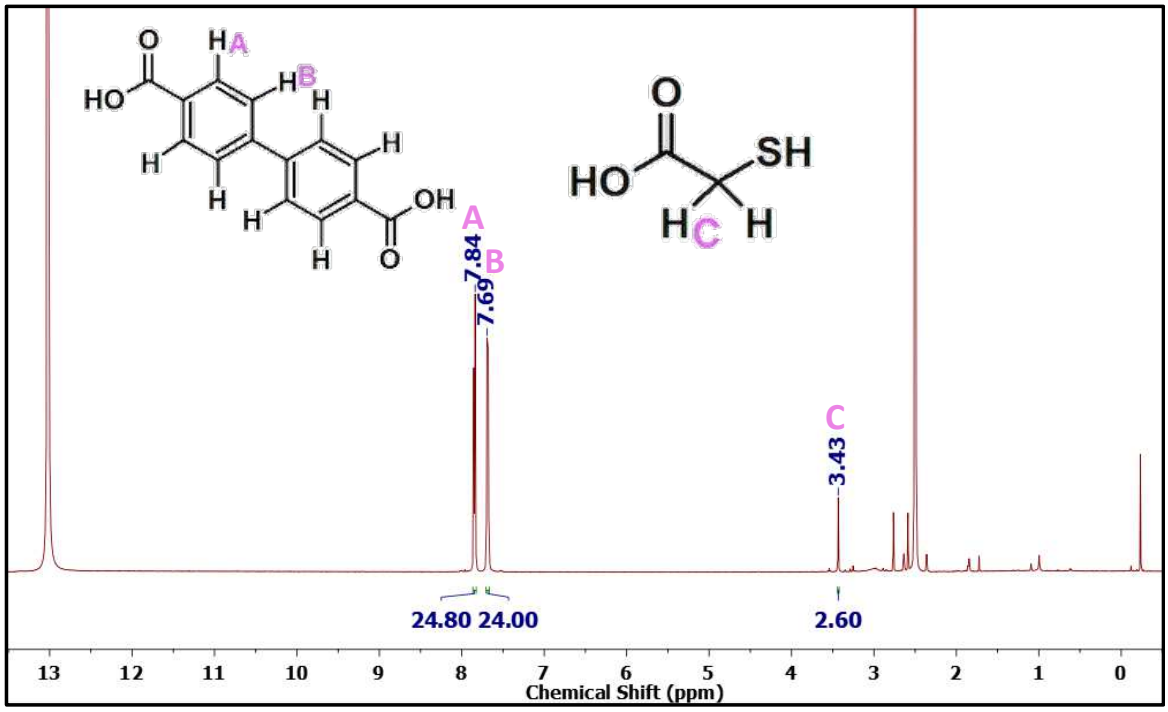
HO
O
HA
HB
H
H
H
H
H
H
OH
O
HO
O
SH
HC
H
A
7.84
B
7.69
C
3.43
24.80 24.00
2.60
13 12 11 10 9 8 7 6 5 4 3 2 1 0
Chemical Shift (ppm)

d)

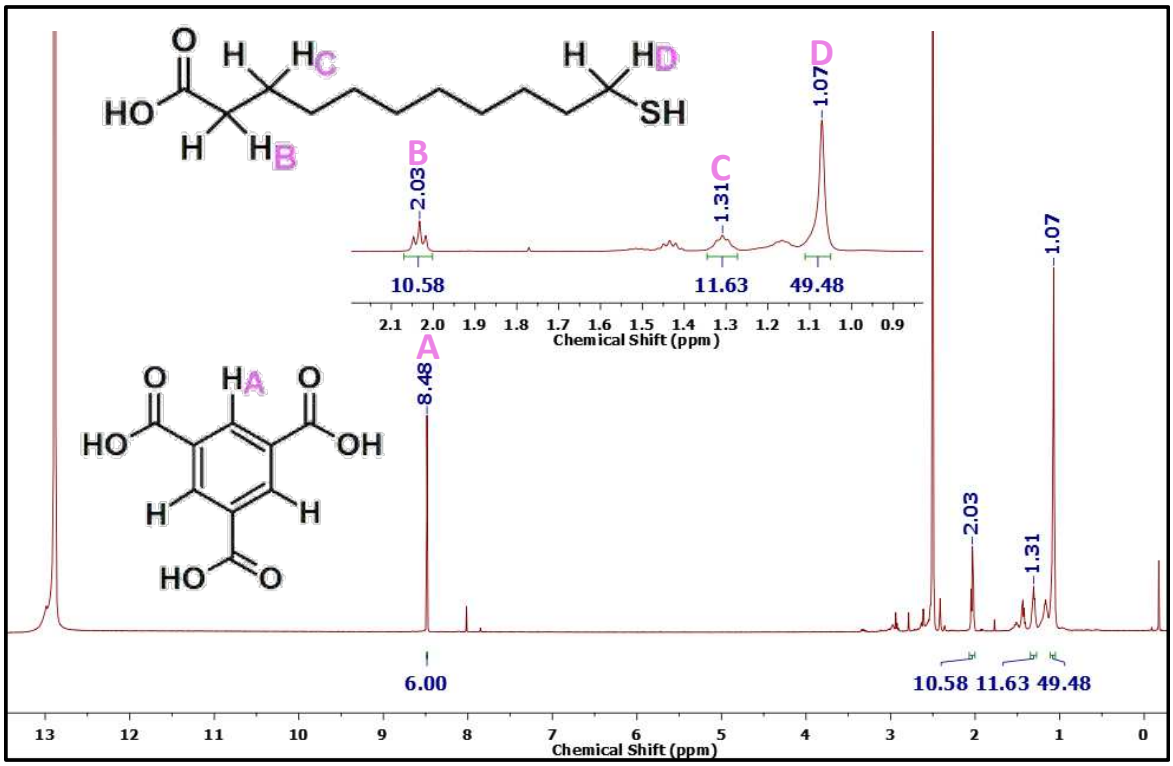
HO
O
H
HC
HB
HD
SH
A
B
C
D
8.48
2.03
1.31
1.07
10.58
11.63
49.48
6.00
HA
OH
Chemical Shift (ppm)

e)

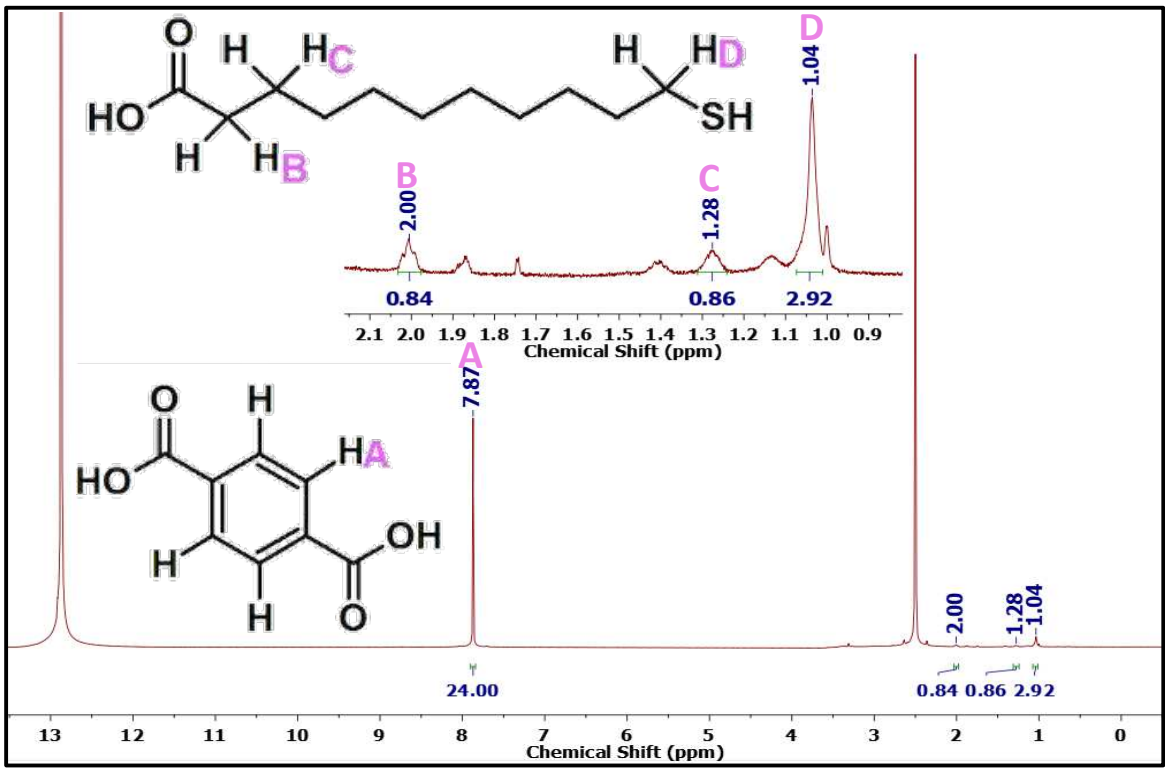
HO
O
H
HC
HB
HD
SH
A
B
C
D
7.87
2.00
1.28
1.04
0.84
0.86
2.92
24.00
HA
OH
Chemical Shift (ppm)

f)

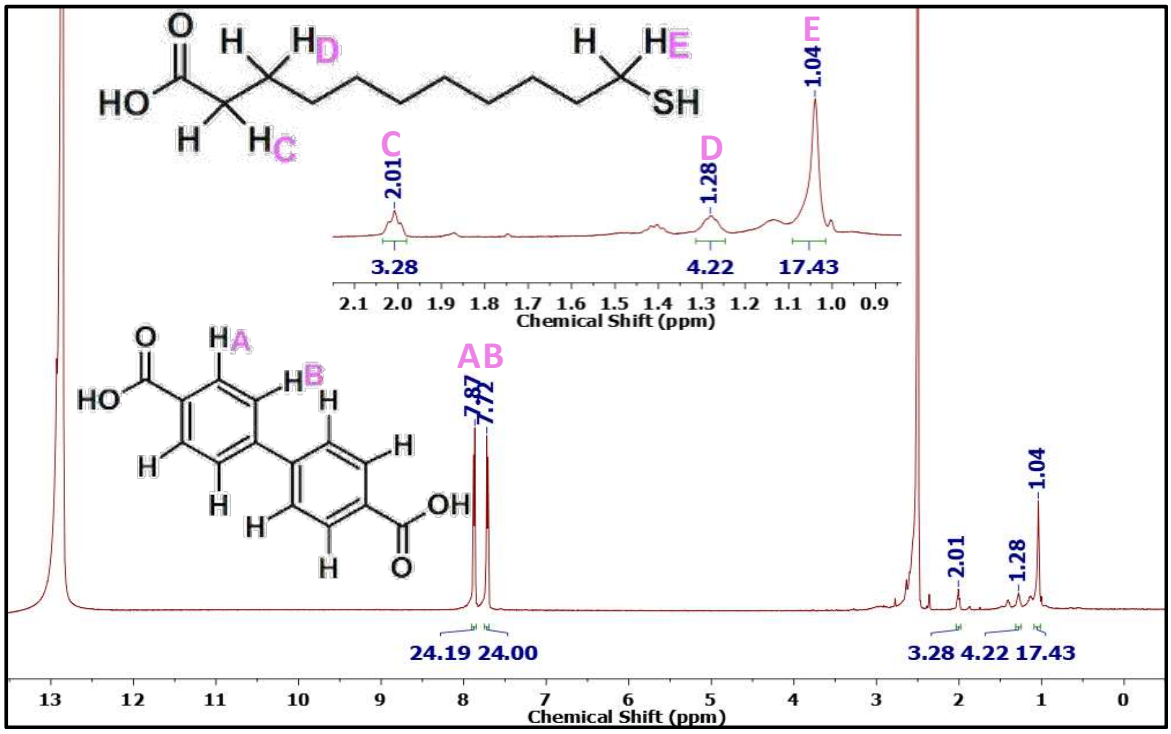

Figure 2.12. [1]H-NMR spectra showing ligand incorporation of thioglycolic acid in a) MOF-808 b) UiO-66, c) UiO-67 and mercaptoundecanoic acid in d) MOF-808, e) UiO-66, f) UiO-67.

Particle size analysis of the MOFs post-SALI were determined using DLS (Figure A.2-A.4). Incorporation of the thiolated ligands does not have a major effect on the average particle size of the nanoMOFs, and the hydrodynamic diameter of the MOFs after ligand incorporation present no aggregation and remain monodisperse and uniform.

2.4. Mucoadhesion Characterization

The mucoadhesive properties of all MOFs before and after post-synthetic modification were studied by (i) a quantitative colorimetric method to assess the % mucins retained when in contact with the MOFs, and (ii) fluorescence spectroscopy to gather information on the strength of the interaction between the mucins and MOFs. Typical experiments involve mixing a stock solution of commercial-based mucins from bovine submaxillary glands with the MOF samples. First, UV–Vis experiments were used for thiol quantification of the post-synthetically modified MOFs using Ellman's test to quantify the presence of thiol ligands on the surface of the MOFs.

2.4.1. Thiol Quantification by UV–visible Spectroscopy

In order to quantify the number of thiol groups present on the surface of the thiolated MOFs, a thiol quantification by Ellman's test is performed and quantified by UV–visible spectroscopy. Quantifying the surface thiols allows for the determination of the quantity of thiols capable of interacting with the mucins, since the reagents (and the mucins) are too large to enter into the MOF pores. The Ellman's test involves preparing a set of N-acetyl-L-cysteine standards, mixed with a 5,5'-dithiobis-(2-nitrobenzoic acid) (DTNB) reagent and will react with the sulfhydryl groups to form a mixed disulfide and 2-nitro-5-thiobenzoic acid (TNB) molecule. The yellow-colored TNB product can be measured by UV–Vis at 400 nm. Figure 2.13 represents a calibration curve with the known standard concentrations ranging from 0 μM to 60 μM resulting in a linear relationship where an increasing amount of thiols reacting with DTNB results in an increase in concentration of TNB. As such, the protocol is further justified by the appearance of a darker yellow colored solution when DTNB is mixed with TNB at increasing concentrations. Table 2.1 showcases the results obtained comparing the moles of thiol by ^{1}H-NMR and UV–Vis spectroscopy for MOF-808, UiO-66, and UiO-67 with thioglycolic acid and mercaptoundecanoic acid. Essentially, the moles of thiol determined by ^{1}H-NMR spectroscopy represents the relative moles of thiol when compared to the moles of linker, whereas the moles of thiol by UV–Vis spectroscopy determines the number of thiol groups on the external surface of the MOF only. The DTNB reagent with dimensions of ~ 17 Å x 6 Å is too large to be encapsulated in the pores of the MOF. It is thus expected to observe a lower amount of moles of thiol by UV–Vis spectroscopy and a higher amount of moles of thiol determined by ^{1}H-NMR spectroscopy, as shown in Table 2.1. This data confirms that there are surface thiol groups in all cases which may be capable of interacting with mucins.

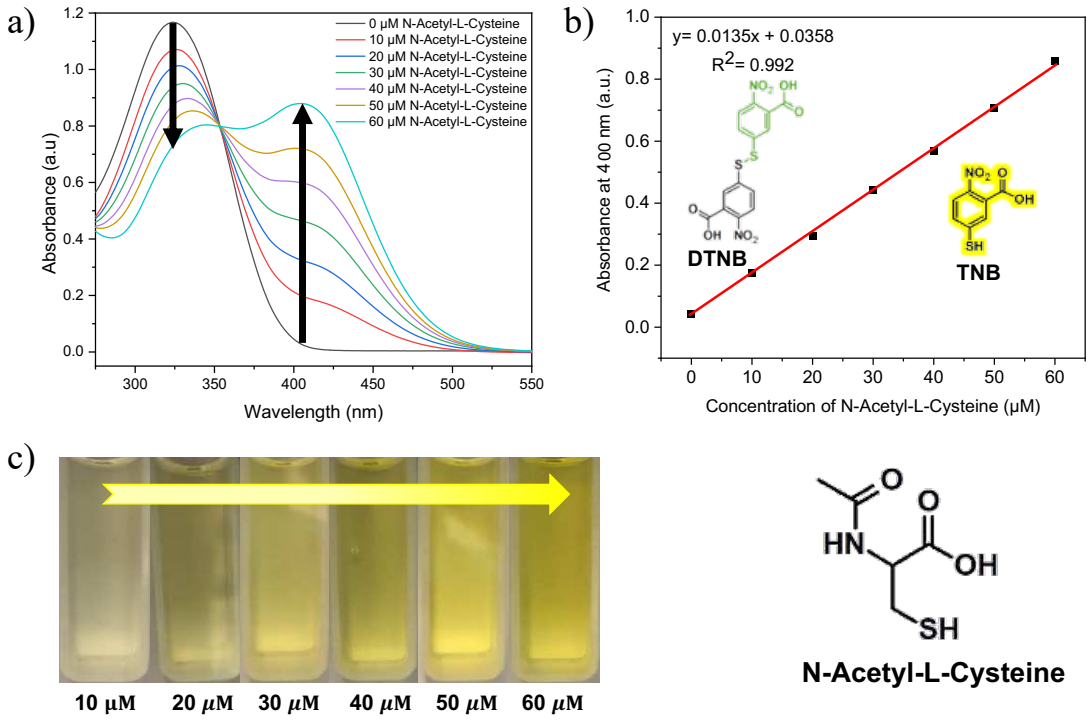

Figure 2.13. Representation of N-Acetyl-L-Cysteine (a) absorbance spectrum for all concentrations, (b) linear standard calibration curve, (c) increasing TNB concentration with increasing thiol concentration.

Table 2.1. Theoretical and experimental moles of thiol determined by ^{1}H-NMR and UV–Vis respectively, for MOF-808, UiO-66, and UiO-67 with thioglycolic acid and mercaptoundecanoic acid calculated based on the absorbance of TNB at 400 nm.

Sample	Moles of Thiol by ^{1}H-NMR per metal node	Moles of Thiol by UV–Vis per metal node (surface thiols only)
MOF-808 Thioglycolic acid	1.41 x 10^{-6}	2.19 x10^{-7}
MOF-808 Mercaptoundecanoic acid	2.03 x 10^{-6}	1.11 x 10^{-8}
UiO-66 Thioglycolic acid	1.70 x 10^{-7}	1.51 x10^{-8}
UiO-66 Mercaptoundecanoic acid	2.06 x 10^{-7}	4.59 x 10^{-9}
UiO-67 Thioglycolic acid	5.39 x 10^{-7}	1.42 x 10^{-9}
UiO-67 Mercaptoundecanoic acid	7.12 x 10^{-7}	1.23 x 10^{-9}

2.4.2. Periodic-Acid/Schiff's Reagent Coloration Protocol

Described as a colorimetric quantification process, PAS coloration assesses the percentage of mucins retained by the MOFs as determined by UV–Vis spectroscopy. In doing so, a set of standards of mucins, control MOFs, and post-synthetically modified MOF samples were prepared. MOF samples were then incubated with mucins under stirring for 2 h at room temperature, and further centrifuged. The supernatant was then collected (600 μL) and mixed with a 180 μL volume of periodic acid reagent and further incubated for 2 h at 37 ℃, followed by the addition of 60 μL of Schiff's reagent, and reacted for 30 mins before UV–visible absorption spectroscopy measurements.

Based on preliminary experiments, the standard protocol for PAS coloration is to use the same ratio of mucins to MOFs (1 mg/mL) or to use a higher concentration of MOFs to mucins in order to make a comparative analysis of the true mucoadhesion.[118, 157] When following this standard approach, however, it resulted in the samples falsely appearing highly mucoadhesive due to aggregation of the nanoMOFs with the mucins. When adding higher concentrations of nanoMOFs to the solution, aggregation increases and leads to trapping of the mucins, but that does not represent true mucoadhesion. As this protocol depends on the size of the material and ratio of mucins to material, the parameters were optimized by incorporating a lower concentration of nanoMOFs (0.1 mg/mL) in order to minimize aggregation of nanosized MOF samples and trapping of the mucins (Figures 2.14 and 2.16).

A calibration curve was collected with concentrations ranging from 0 to 150 μg/mL of standard mucins and each mucoadhesion sample (MOF present) was subtracted from a corresponding control sample (no MOF present) to quantify the free mucins adsorbed by the MOFs. Based on the results presented in Figures 2.14, 2.15, and 2.16, all MOFs demonstrate mucoadhesion, including the control and SALI samples. MOF-808 with thioglycolic acid is found to be more mucoadhesive than the MOF-808 with mercaptoundecanoic acid, which is consistent with the number of accessible surface thiols being higher in the former case as determined by the Ellman's test (Section 2.4.1). This trend holds true for the UiO-66 SALI samples but is not observed for the UiO-67 SALI samples.

Interestingly, the control nanoMOFs with no thiols, also demonstrate mucoadhesion. This was not the hypothesized scenario, as Zr_6-based MOFs have a surface that is slightly negatively

charged,[168] therefore it was not expected that the control MOFs would interact with the negatively charged mucins. Since there are no thiol groups present on the control MOFs, this suggests that they are able to interact with the mucins without any specific disulfide interaction required. In fact, in the case of MOF-808, the mucoadhesion in the control MOF surpasses that of the thiolated MOFs. However, further inquiry is needed to understand the potential interactions between nanosized Zr_6-based MOFs and mucins using this type of protocol.

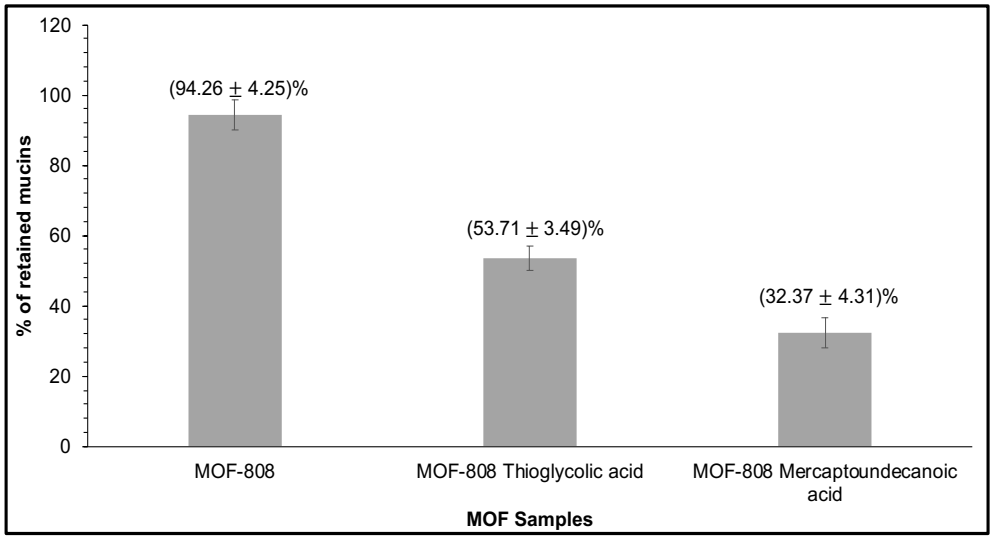

Figure 2.14. Periodic Acid-Schiff (PAS) colorimetric quantification representing % mucins retained to the thiolated MOFs for MOF-808 control and SALI samples. 0.1 mg/mL of MOF was used in each case to prevent aggregation and to observe a difference in the retained mucins.

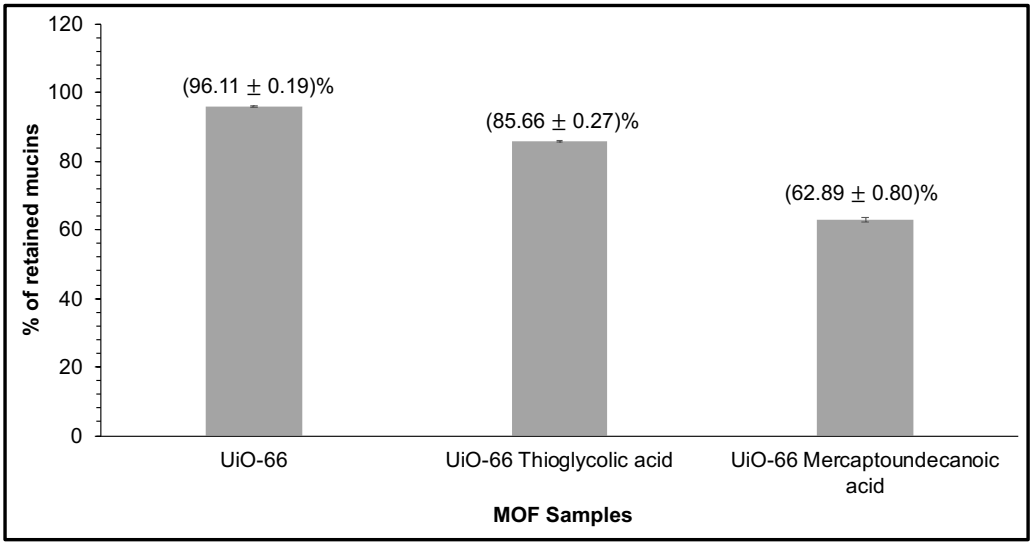

Figure 2.15. Periodic Acid-Schiff (PAS) colorimetric quantification representing % mucins retained to the thiolated MOFs for UiO-66 control and SALI samples. 1 mg/mL of MOF was used

in each case to prevent aggregation and to observe a difference in the retained mucins. It should be noted that the amount of MOF used for these samples is higher when comparing the data to those in Figure 2.14 and 2.16.

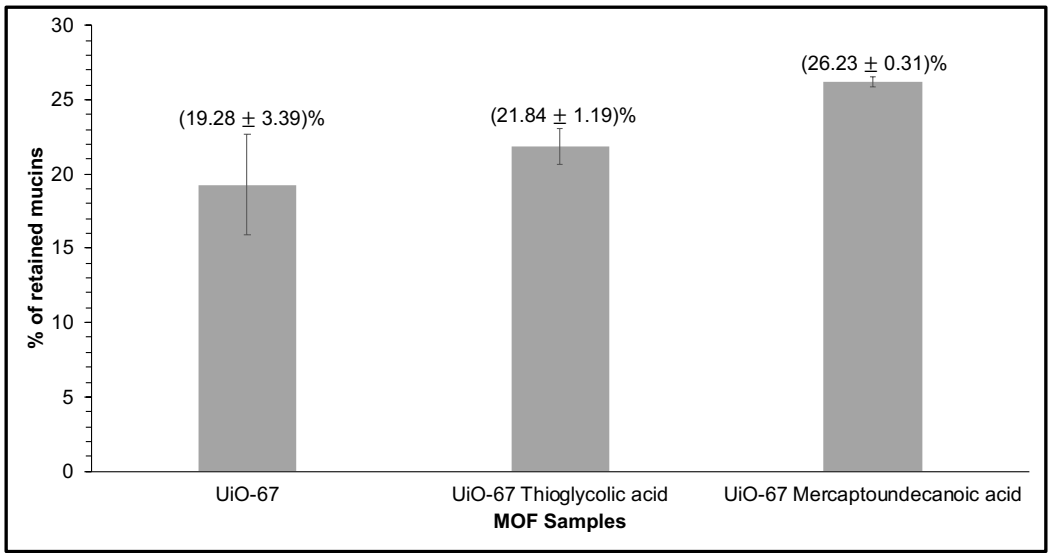

Figure 2.16. Periodic Acid-Schiff (PAS) colorimetric quantification representing % mucins retained to the thiolated MOFs for UiO-67 control and SALI samples. 0.1 mg/mL of MOF was used in each case to prevent aggregation and to observe a difference in the retained mucins.

2.4.3. Fluorescence Spectroscopy

In order to determine how strong the interaction is between the mucins and the MOFs, and to understand the localization between the MOFs and mucins, fluorescence spectroscopy measurements were gathered. The general protocol consists of a fluorophore, being the mucins, that will emit light at 337 nm after excitation at 285 nm, resulting in high fluorescence intensity. With the mucin concentration remaining the same, an increasing amount of MOF sample is added to the solution to quench the fluorescence if mucoadhesion occurs. The emission spectrum in Figure 2.17a represents the mucins in the presence of varying concentrations of thiolated MOF-808 samples and results in two emission peaks; 315 nm representing the blank, that being water, and the second peak from MOF samples that are fluorescing in the region of 350 nm. This emission from the samples interferes with the fluorescence signal that is evidence of mucoadhesion at 337 nm. A Stern-Volmer plot best describes the quenching effect that occurs due to the dynamic interaction between the MOFs and the mucins. Figure 2.17b, suggests that there are no strong interactions between the MOFs and the mucins, however, due to interference of the fluorescence signals, the results should not be overinterpreted.

The thiolated UiO-66 and UiO-67 samples cannot be analyzed by fluorescence spectroscopy because the fluorescence of the MOFs is very high. The emission of thiolated UiO-66 and UiO-67 is also in the region where the mucins emit at 337 nm (Figure A.6) and owing to the fact that the tryptophan emission from the mucins is weak, the MOF emission masks it. It is interesting to note that this fluorescence spectroscopy protocol was used previously to analyze mucoadhesion of bulk MOF materials with a similar composition to those reported herein and there was no fluorescence observed to be coming from the MOFs. As such, the fluorescence coming from the nanosized MOFs must be related to the materials having different properties on the nanoscale. Hence, at the moment we can only rely on the PAS coloration results for the nanosized MOFs, suggesting that the MOFs are highly mucoadhesive but not giving any information about the strength of those interactions.

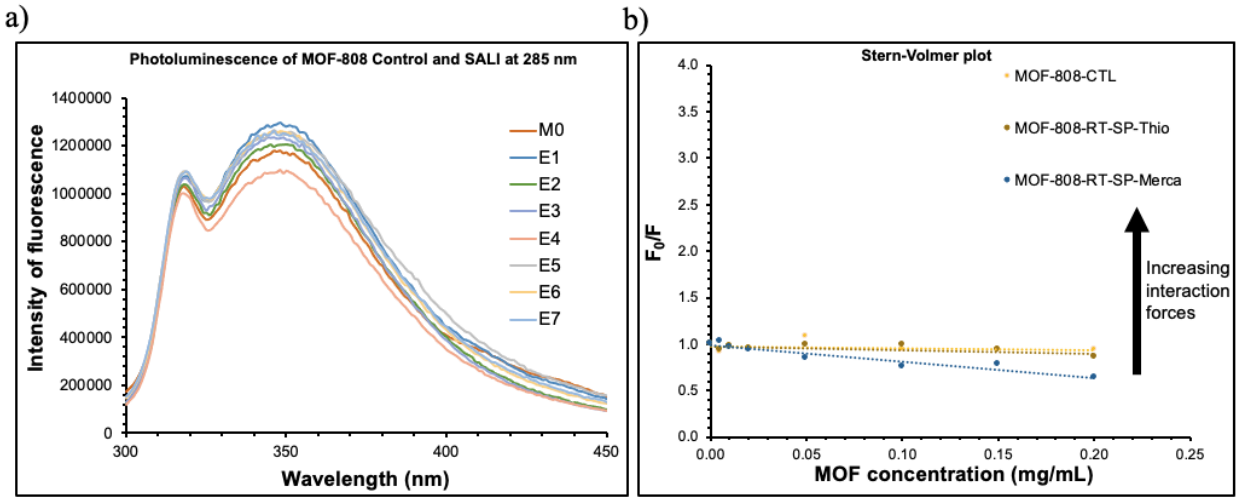

Figure 2.17. Fluorescence spectroscopy measurements for mucoadhesion characterization. a) emission spectra of MOF-808 control (no thiols) and SALI MOF-808 samples excited at 285 nm. b) Stern-Volmer plot for mucin fluorescence in the presence of SALI MOF-808 samples.

To summarize, the mucoadhesion characterization results from the PAS coloration protocol suggest that the SALI MOF samples (MOF-808, UiO-66, and UiO-67) are mucoadhesive, even with the need to use lower MOF:mucin to prevent issues associated with MOF aggregation.

2.5. Conclusions

In conclusion, nanosized Zr_6-based MOFs were synthesized and characterized, and further post-synthetically modified using SALI to thiolate the open-metal sites of the MOFs with thioglycolic acid and mercaptoundecanoic acid and their mucoadhesive properties were assessed. The phase purity and bulk crystallinity of all MOFs were confirmed with PXRD, and their surface

areas were assessed with N_2 adsorption-desorption isotherms. DLS measurements confirm the nanoscale size of the MOFs before and after SALI. ^{1}H-NMR spectroscopy confirms the presence of the incorporated thiolated ligand and quantification of thiol ligands per metal node with results suggesting the possible presence of defects in the MOF or excess ligands trapped in the MOF pores in some cases. Thiol quantification by UV–vis spectroscopy demonstrates accessible thiols on the MOF surface. The mucoadhesive properties of the MOFs before and after modification with thiolated ligands were investigated with two techniques that required modification of standard protocols due to the unique properties of the nanosized MOFs. The PAS coloration results suggest that all MOFs studied herein are highly mucoadhesive. The fluorescence spectroscopy results are difficult to interpret due to fluorescent interferences from the MOF but show little to no quenching of the mucin fluorescence when in contact with the thiolated MOF-808 samples meaning that the mucoadhesive interaction may be weak. The SALI MOFs for UiO-66 and UiO-67 could not be analyzed by fluorescence spectroscopy due to the high fluorescence of the MOFs. Despite this hurdle, we can still conclude based on the PAS coloration results that all the MOFs in this study are mucoadhesive, including the control samples and thiolated materials.

Chapter 3

Nanosized Mixed Linker UiO-66-$(SH)_2$ Metal–Organic Frameworks for Ophthalmic Drug Delivery

3.1. Introduction and Ophthalmic Drug Delivery

Ophthalmic drug delivery has become of increasing interest and challenge over the past few decades owing to the barriers of the anatomy and physiology of the eye, and poor mucoadhesive properties of current eye drop formulations.[118, 169] As such, mucoadhesion, defined as the ability to adhere to mucosal layers or surfaces,[118] paves the way for designing and developing drug vector systems with improved performance and efficiency for long-term application. Metal–organic frameworks (MOFs), a class of porous and highly tunable materials exhibiting inorganic metal ions or nodes bridged by multitopic organic linkers, are promising potential systems for drug delivery.[170] Specifically, by incorporating thiol groups (-SH) in the structure of MOFs, a disulfide bond can form with cysteine amino acids present in the mucin layer of the eye increasing the overall mucoadhesive properties and drug retention times.[118] The objective of this research is to explore a mixed-linker approach for incorporating thiol groups in MOFs for ophthalmic drug delivery.

Different approaches can be used to introduce thiol functional groups in MOFs including; (i) post-synthetically modifying (PSM) the open-metal sites (OMSs) of MOFs with thiolated ligands, or (ii) incorporating a thiol-based linker in the MOF structure. As discussed in chapter 2, a PSM process called solvent-assisted ligand incorporation (SALI) was used to introduce two thiolated ligands of interest; thioglycolic acid and mercaptoundecanoic acid. Based on the mucoadhesive characterization results obtained, it suggests that postsynthetic incorporation of thiolated ligands in MOFs, including the number of thiols and accessibility of those thiols, has a moderate effect on the mucoadhesive properties of the MOFs (section 2.4). Previous research in our group involved the use of 2,5-dimercaptoterephthalic acid (BDC-$(SH)_2$) in the synthesis of micron sized UiO-66 and the results demonstrated crystalline and robust structures with excellent mucoadhesive properties (Figure 3.1).[157] The periodic-acid Schiff (PAS) coloration results indicated that 90% of mucins adhered to UiO-66-$(SH)_2$, and fluorescence spectroscopy data confirm the increasing strong collisional and static quenching of the mucins when in contact with the UiO-66-$(SH)_2$.[157] Preliminary drug delivery experiments with the anti-inflammatory drug

Flurbiprofen suggest that UiO-66-$(SH)_2$ is capable of encapsulating the drug, however with loadings lower than the control (non-thiolated) MOFs. The difference in drug loading can be attributed to the accessible surface area and porosity of the MOFs. That is, owing to the thiolated MOFs having a sulfur atom present, the pore window capable of encapsulating drug molecules is reduced due to the large ionic radii of sulfur (1.84 Å). Building upon this previous research, some areas that require improvement are: (i) reducing the crystallite size of the thiolated MOFs to improve cellular uptake and control the overall speed and diffusion *in vivo*, and (ii) finding the right concentration of thiol groups to increase drug loading capacities and minimize blocking of the pore windows, while maximizing mucoadhesions.[157]

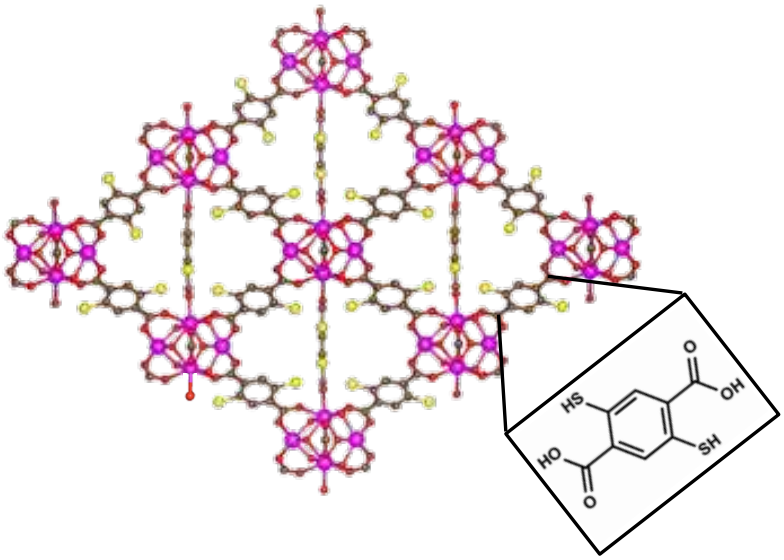

Figure 3.1. UiO-66-$(SH)_2$ with 100% incorporation of the BDC-$(SH)_2$ linker.

Given that enhanced mucoadhesive properties were observed in UiO-66-$(SH)_2$ compared to UiO-66, our approach is to tune the incorporation of BDC-$(SH)_2$ in the UiO-66 structure by synthesizing a series of mixed linker MOFs. More specifically, this will involve (i) synthesizing the mixed linker MOFs based on a protocol recently established for nanosizing UiO-66, and (ii) incorporating different percentages of BDC-$(SH)_2$ compared to BDC in the MOF synthetic protocol in order to improve pore accessibility for the drug molecules which is essential for achieving high drug loadings.

The bulk of this chapter will be focused on the synthesis and characterization of mixed linker nanosized UiO-66 analogues (Figure 3.2) obtained through a *de novo* approach (Figure 3.3).

Furthermore, the mucoadhesive properties of the mixed linker UiO-66-$(SH)_2$ are assessed by a colorimetric assay and fluorescence spectroscopy.

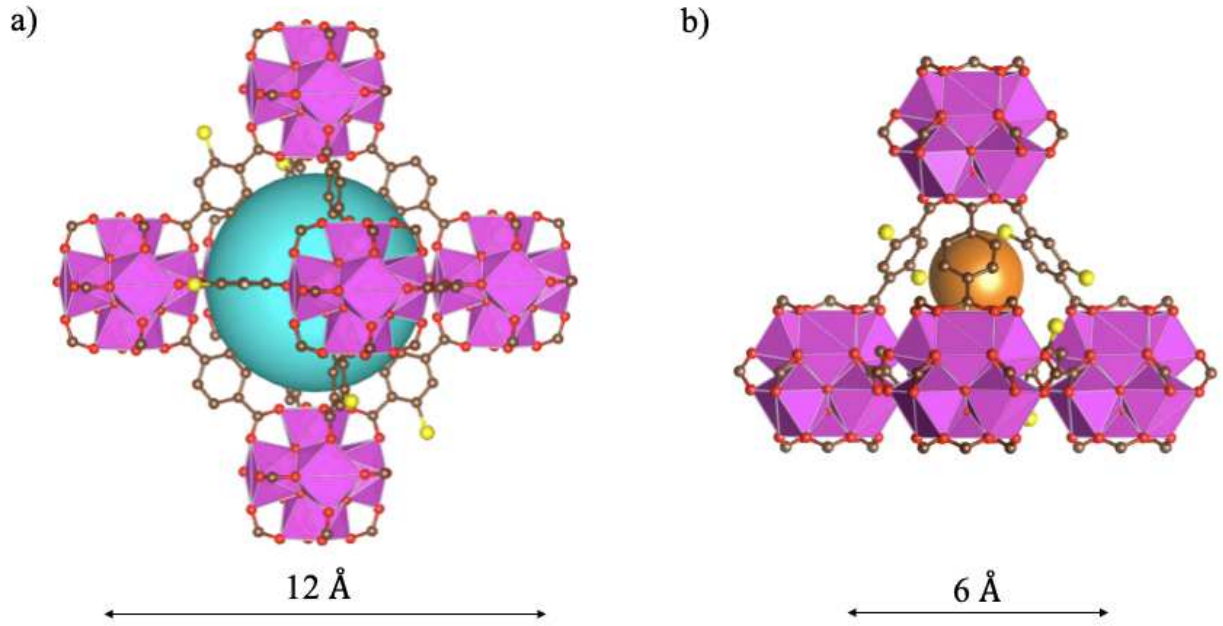

Figure 3.2. Schematic illustration of mixed thiolated UiO-66-$(SH)_2$ cubic structure demonstrated by a) octahedral cages of 12 Å (blue sphere), and b) tetrahedral cages of 6 Å (orange sphere). Zr_6-based metal cluster (magenta), oxygen (red), carbon (brown), and sulfur (yellow).

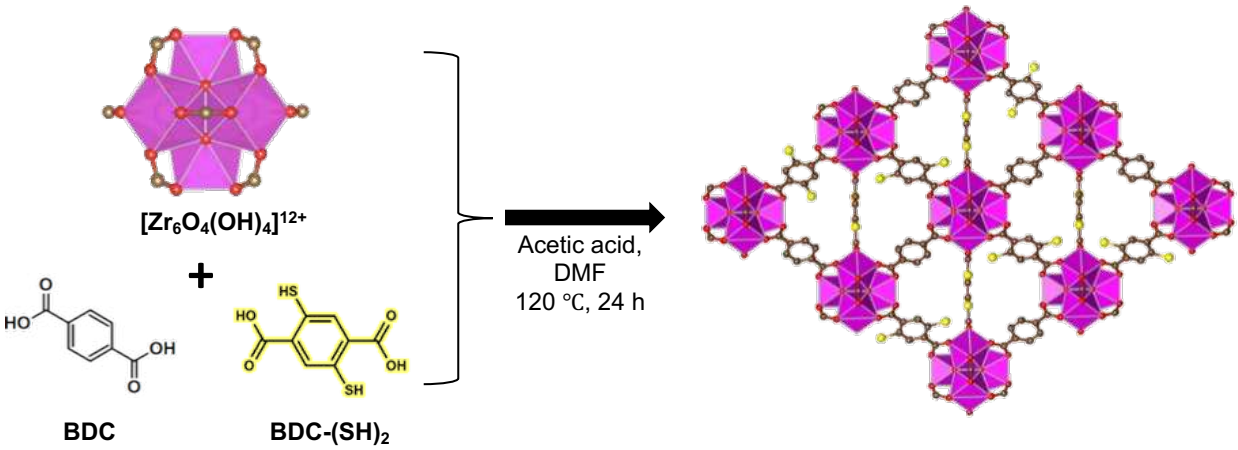

Figure 3.3. Schematic representation of the solvothermal synthesis of mixed thiolated linker UiO-66-$(SH)_2$. Zr_6-based metal cluster (magenta), oxygen (red), carbon (brown), and sulfur (yellow).

3.2. Experimental Procedures

3.2.1. Materials

All chemicals were purchased from commercial suppliers and used with no further purification. Zirconium (IV) chloride ($ZrCl_4$; Alfa Aesar, 99.5%), glacial acetic acid (Fischer Scientific, 99.7%), terephthalic acid (BDC; Acros Organics, 99.5+%), *N,N*-dimethylformamide (DMF; Fischer Chemical Certified ACS, ≥99.8%), acetone (Fischer Chemical Certified ACS, 99.5%), 1,4-diazabicyclo[2.2.2]octane (Tokyo Chemical Industry (TCI), >98.0%), diethyl 2,5-digydroxyterephthalate, (Sigma Aldrich, 97%), dimethylthiocarbamoyl chloride (TCI, >97.0%), *N,N*-dimethylacetamide (DMA; Fisher Chemical Reagent Grade), potassium hydroxide (Alfa Aesar, 85%), deuterated chloroform ($CDCl_3$; Cambridge Isotope Laboratories, 99.8 atom % D with 0.05% v/v tetramethylsilane (TMS)), deuterated sulfuric acid (D_2SO_4; Sigma-Aldrich, 99-98 wt%), deuterated dimethyl sulfoxide (DMSO-d_6; Cambridge Isotope Laboratories, 99.8% D with 0.05% v/v tetramethysilane (TMS)), sodium acetate (Sigma-Aldrich, ≥99.9%), Tris (Tris(Hydroxymethyl) Aminomethane) (Acros Organics, +99%), N-acetyl-L-cysteine (Alfa Aesar, 98+%), and 5,5-dithiobis(2-nitrobenzoic acid) (Alfa Aesar, 99%). 2,5,-dimercapto-1,4-benzenedicarboxylic acid (H_2DMBD) was prepared according to the literature (Figure A.7-A.10).

3.2.2. General Methods

Powder X-ray diffraction (PXRD) results were collected using a benchtop Rigaku Miniflex or a Bruker D2 Phaser (Bruker AXS, Madison, WI, USA) both equipped with a Cu-based (Kα) X-ray source and a nickel filter. The dry powdered samples were packed with a smooth layer onto a silicon wafer zero-background sample holder. Results were collected from 4-40° at 0.02 θ increments in the 2θ-range.

N_2 adsorption-desorption experiments were conducted on a Micromeritics Tristar II Plus instrument equipped with a nitrogen dewar filled with liquid nitrogen at 77 K to obtain surface area and porosity results. A Micromeritics SmartVac prep with a hybrid turbo vacuum pump was used prior to BET analysis to activate the samples at 120 ℃ for 24 h under vacuum conditions.

Dynamic light scattering (DLS) size distribution profiles were collected with a Malvern Panalytical Zetasizer Nano ZSP instrument at 25 ℃ . The MOF samples were sonicated in 18-ohm MilliQ pore water, followed by dilutions with 500 μL aliquots of the MOF suspension in 1.5 mL

of MilliQ pore water. The samples were analyzed in a quartz cuvette with 1 cm path length and 3.50 mL capacity.

Proton nuclear magnetic resonance (^{1}H-NMR) spectra were obtained on a 300 MHz Bruker spectrometer instrument equipped with a Topsin software system. The samples were digested and sonicated with ~ 6 drops of deuterated sulfuric acid, followed by 600 μL of DMSO-d_6. The samples were analyzed at 256 scans and referenced to the residual solvent peaks.

Ultraviolet–visible (UV–vis) absorption analysis was conducted on a Cary 5000 series UV–vis NIR spectrophotometer from Agilent technologies. The solutions were analyzed with a dual beam mode from 200-800 nm and a source changeover wavelength at 350 nm. A two-sided quartz cuvette with a 1 cm path length and maximum volume of 3.50 mL capacity was used to measure the sample solutions.

Scanning electron microscopy (SEM) micrographs were collected on a Phenom ProX SEM benchtop at 12 kV. All samples were first sputter coated with a 5 mm gold (Au) layer by using a Cressington 108 Auto/SE Sputter Coater with MTM-20 high resolution film thickness controller.

Thiol Quantification with Ellman's Test: A 1M TRIS Buffer solution was prepared in a volumetric flask with TRIS base (12.220 g, 101 mmol) and MQ H_2O. The pH of the solution was adjusted to 8.0 by adding hydrochloric acid and further diluted to 100 mL. A 50 mM sodium acetate solution was prepared in a 100 mL volumetric flask by adding sodium acetate (0.4101 g, 5.0 mmol) and MQ H_2O. The pH was adjusted to ~ 4-5 by addition with acetic acid (93.5 μL) and further diluted to 100 mL. The 5,5'-dithiobis(2-nitrobenzoic acid) (DTNB) reagent was prepared by dissolving (8.50 mg, 0.0214 mmol) of DNTB in 10 mL of sodium acetate (50 mM) in a 10 mL volumetric flask. The solution was then sonicated and stored in the fridge. The Ellman's test was followed according to previously reported methods.[158] A calibration curve was prepared with a known N-acetyl-L-cysteine standard starting at 0 μM. The standard samples were prepared by mixing 150 μL of DTNB reagent, 300 μL of TRIS buffer, 2520 μL of MQ H_2O, and 30 μL of N-acetyl-L-cysteine standard for a total cuvette volume of 3000 μL. A calibration curve was prepared with concentrations of standard from 0-60 μM, with 0 μM attributed to the blank with just MQ H_2O. The solution was mixed and incubated for 5 mins at room temperature. Once the yellow colour of the solution was produced, the cuvette was placed into the UV spectrophotometer and

the optical absorbance was measured at 400 nm. The UV–vis was blanked with each sample in between runs.

The mixed thiolated MOF samples were prepared by weighing out the following for the 10%, 30%, 40%, 70%, and 100% thiolated linker samples in separate 15 mL centrifuge tubes; 0.5 mg, 1.7 mg, 4.8 mg, 3.1 mg, and 2.4 mg. To each centrifuge tube, the addition of Ellman's reagents were added (2520 μL of MQ H_2O, 300 μL of TRIS buffer, 150 μL of DTNB reagent, 30 μL of MQ H_2O). The solutions were mixed and incubated for 15 mins at room temperature. Once the yellow colour of the solution was produced, the samples were centrifuged at 7500 rpm for 5 mins. 1.5 mL (2x) of the supernatant was removed and transferred to separate microcentrifuge tubes and further microcentrifuged at 10000 rpm for 10 mins to ensure a clear yellow solution. The supernatants (3.0 mL) were then transferred to the cuvette and placed into the UV spectrophotometer and the optical absorbance was measured at 400 nm. The UV–vis was blanked with each sample in between runs.

3.2.3. Synthesis and Activation of UiO-66-$(SH)_2$ (10%, 30%, 40%, 70%, 100%)

The mixed thiolated UiO-66-$(SH)_2$ were each synthesized solvothermally in seperate 8-dram vials including $ZrCl_4$ (31.0 mg, 0.133 mmol), H_2BDC (28.17 mg, 0.170 mmol for 10%), (18.6 mg, 0.112 mmol for 30%), (12.14 mg, 0.073 mmol for 40%), and (6.20 mg, 0.037 mmol for 70%), followed by H_2BDC-$(SH)_2$ (3.13 mg, 0.0136 mmol for 10%), (12.4 mg, 0.053 mmol for 30%), (18.6 mg, 0.081 mmol for 40%), (34.38 mg, 0.149 mmol for 70%), and (42.97 mg, 0.187 mmol for 100%). In each vial, precursors were dissolved with addition of 7.5 mL of DMF, and 250 μL of acetic acid. The reagents were sonicated for a few minutes, and a slight pale yellow color was produced. The mixture was then heated at 120 ℃ for 24 h. A pale yellow precipitate was collected by centrifugation at 7500 rpm for 5 mins and washed with 5 mL of DMF 3x for 3 subsequent days with soakings overnight, followed by 5 mL of acetone 3x for 3 subsequent days with soakings overnight. The sample was dried under vacuum at 120 ℃ for 24 h.

3.3. Results and Discussion

3.3.1. Characterization of Mixed Linker MOFs

A series of mixed linker UiO-66-$(SH)_2$ is investigated for this study. The mixed linker MOFs were synthesized solvothermally and were further characterized in order to gain better

understanding of the material for this application. Figure 3.4 demonstrates the powder X-ray diffraction patterns for the mixed linker UiO-66-$(SH)_2$ samples, showcasing the overall bulk crystallinity and phase purity, confirming that the overall structure remains the same with increasing incorporation of thiolated linkers.

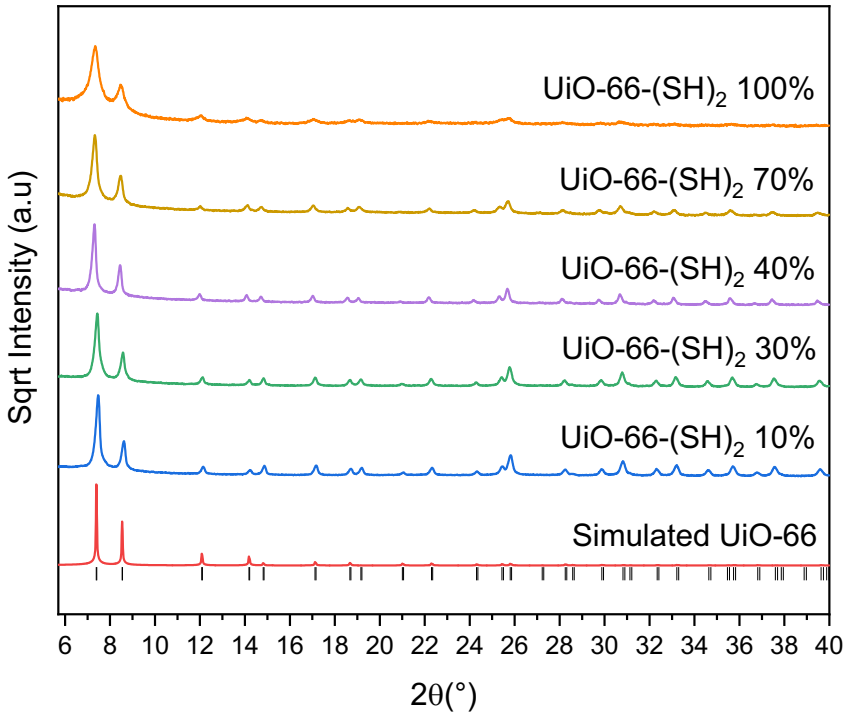

Figure 3.4. PXRD diffractogram of mixed UiO-66-$(SH)_2$ (10%, 30%, 40%, 70%, 100%).

The surface area and porosity of the mixed linker UiO-66-$(SH)_2$ samples were analyzed with N_2 adsorption-desorption experiments at 77 K following the Brunauer-Emmett-Teller (BET) analysis (Figure 3.5). The samples were activated under vacuum at 120 ℃ and the expected reversible Type I(a) isotherms indicating micropores were observed. Specifically, the BET surface area results for the mixed thiolated samples are; 1070 m^2g^{-1}, 910 m^2g^{-1}, 800 m^2g^{-1}, 417 m^2g^{-1}, and 310 m^2g^{-1} for UiO-66-$(SH)_2$ of 10%, 30%, 40%, 70%, and 100%, respectively. Owing to the presence of the sulfur atom from the thiol groups of the BDC-$(SH)_2$, the surface area decreases with increasing BDC-$(SH)_2$ incorporations in the synthesis. This is to be expected due to the large ionic radii of the sulfur atom (1.84 Å), blocking most of the pore aperture of UiO-66, and thereby resulting in a decrease of N_2 uptake in the pores and accessible surface area. Furthermore, surface area is also a gravimetric measurement where the presence of increased sulfur from the thiolated

linker increases the mass of the MOF which potentially blocks access to the pores and the accessible surface area decreases.

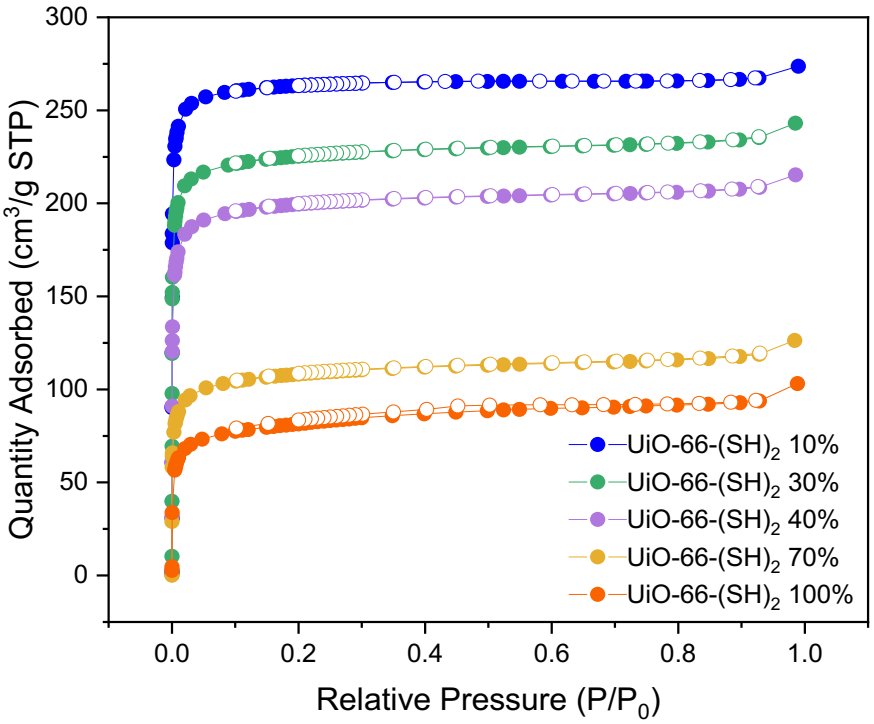

Figure 3.5. N_2 adsorption-desorption isotherms of mixed UiO-66-$(SH)_2$ (10%, 30%, 40%, 70%, 100%).

The proton nuclear magnetic resonance (^{1}H-NMR) spectroscopy of the digested mixed thiolated UiO-66 indicate the linker purity, and the incorporation of the thiolated BDC-$(SH)_2$ in order to quantify the ratio of BDC-$(SH)_2$:BDC in the resulting MOFs. Figure 3.6a-d indicates a signal at ~ 7.9 ppm assignable to the phenyl protons of the BDC linker, and a signal at ~ 8.1 ppm assignable to the phenyl protons of the BDC-$(SH)_2$ linker. The spectra were normalized to 4 BDC protons per linker, and as a result, the proton signals of the BDC-$(SH)_2$ increase gradually with increasing incorporation. In addition, Figure 3.6e shows only the signal at 8.2 ppm of the phenyl protons attributed to the full incorporation of the BDC-$(SH)_2$ in the synthesis. The ratios of phenyl protons from BDC-$(SH)_2$ to those of BDC for each mixed thiolated sample are; 0.26:4, 0.75:4, 1.33:4, 5.20:4 which further translates to 10%, 30%, 40%, 70% incorporation, with the addition of the 100% incorporation.

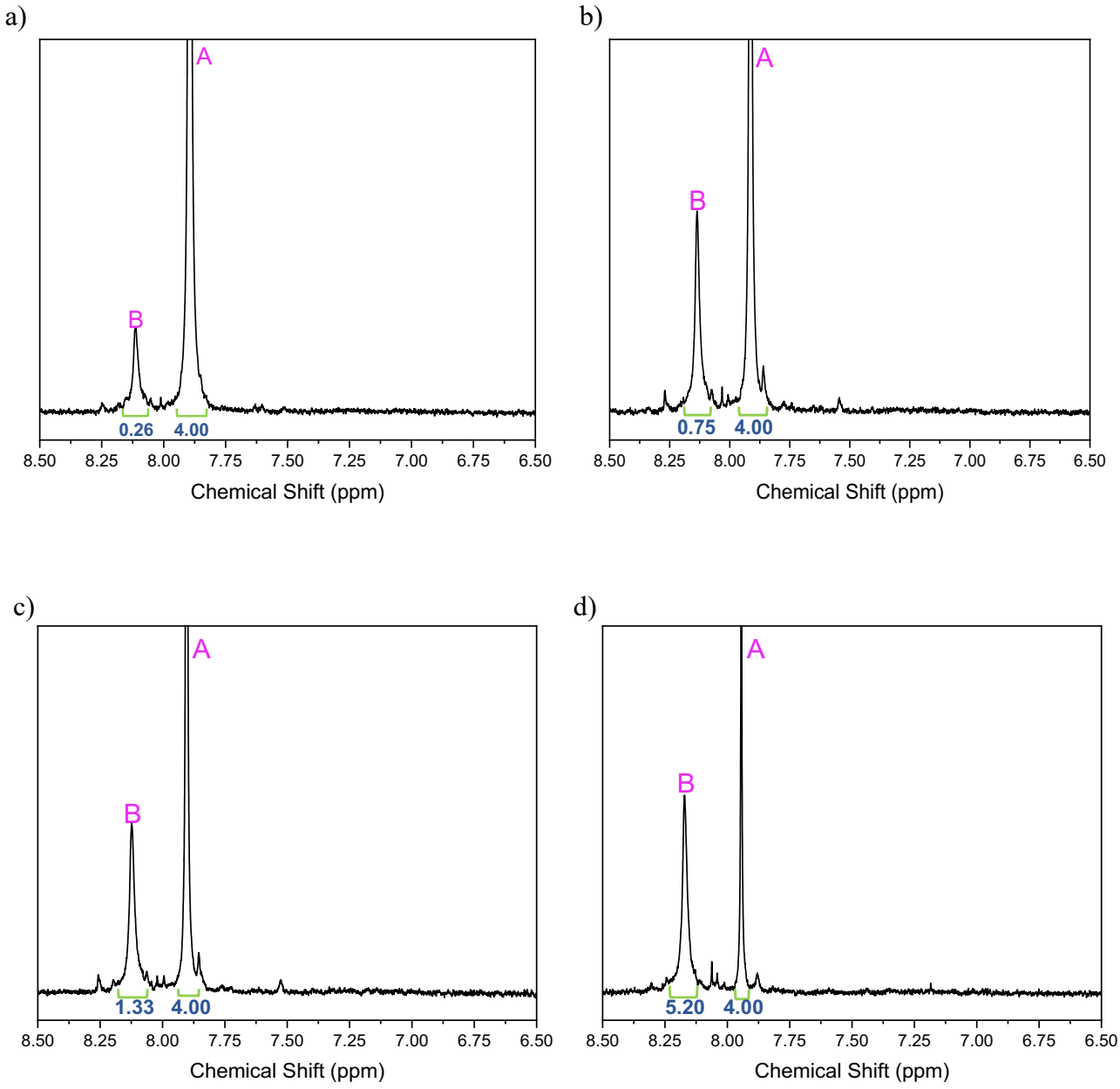
a)
A
B
0.26
4.00
8.50 8.25 8.00 7.75 7.50 7.25 7.00 6.75 6.50
Chemical Shift (ppm)
b)
A
B
0.75
4.00
8.50 8.25 8.00 7.75 7.50 7.25 7.00 6.75 6.50
Chemical Shift (ppm)
c)
A
B
1.33
4.00
8.50 8.25 8.00 7.75 7.50 7.25 7.00 6.75 6.50
Chemical Shift (ppm)
d)
A
B
5.20
4.00
8.50 8.25 8.00 7.75 7.50 7.25 7.00 6.75 6.50
Chemical Shift (ppm)

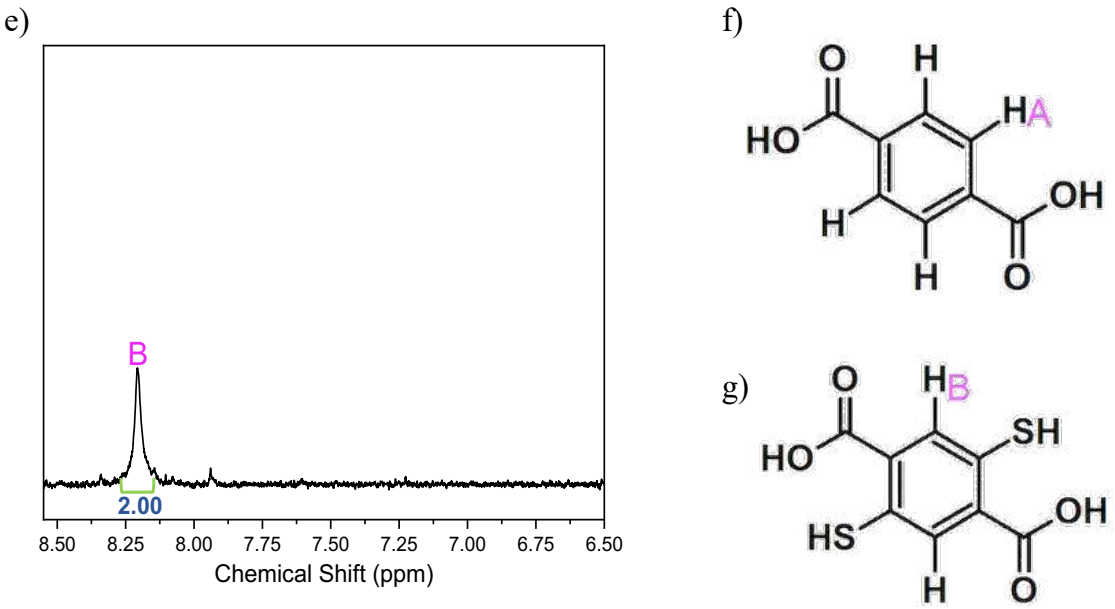

Figure 3.6. ^{1}H-NMR spectra of the mixed linker UiO-66-$(SH)_2$ for a) 10%, b) 30%, c) 40%, d) 70%, and e), 100%. Figures f) and g) represent the non-thiolated BDC linker, and thiolated BDC-$(SH)_2$ linker, respectively. All samples were digested in D_2SO_4 and dissolved in DMSO-d_6 prior to analysis.

The particle sizes of the mixed linker UiO-66-$(SH)_2$ were measured with DLS, showing average particle sizes of 233 nm, 262 nm, 304 nm, 193 nm, and 145 nm respectively for UiO-66-$(SH)_2$ 10%, 30%, 40%, 70%, and 100%. The increasing percent of BDC-$(SH)_2$ leads to smaller crystallites that are more aggregated and have less well-defined morphology as shown by the high PDI of the DLS plots (Figure 3.7) and the SEM micrographs (Figure 3.8). This may be attributed to the increased number of disulfide (S-S) linkages, interparticle S-S bonding when increased ratios of thiolated ligand are added, and the effect of the MOFs being nanosized.[171, 172]

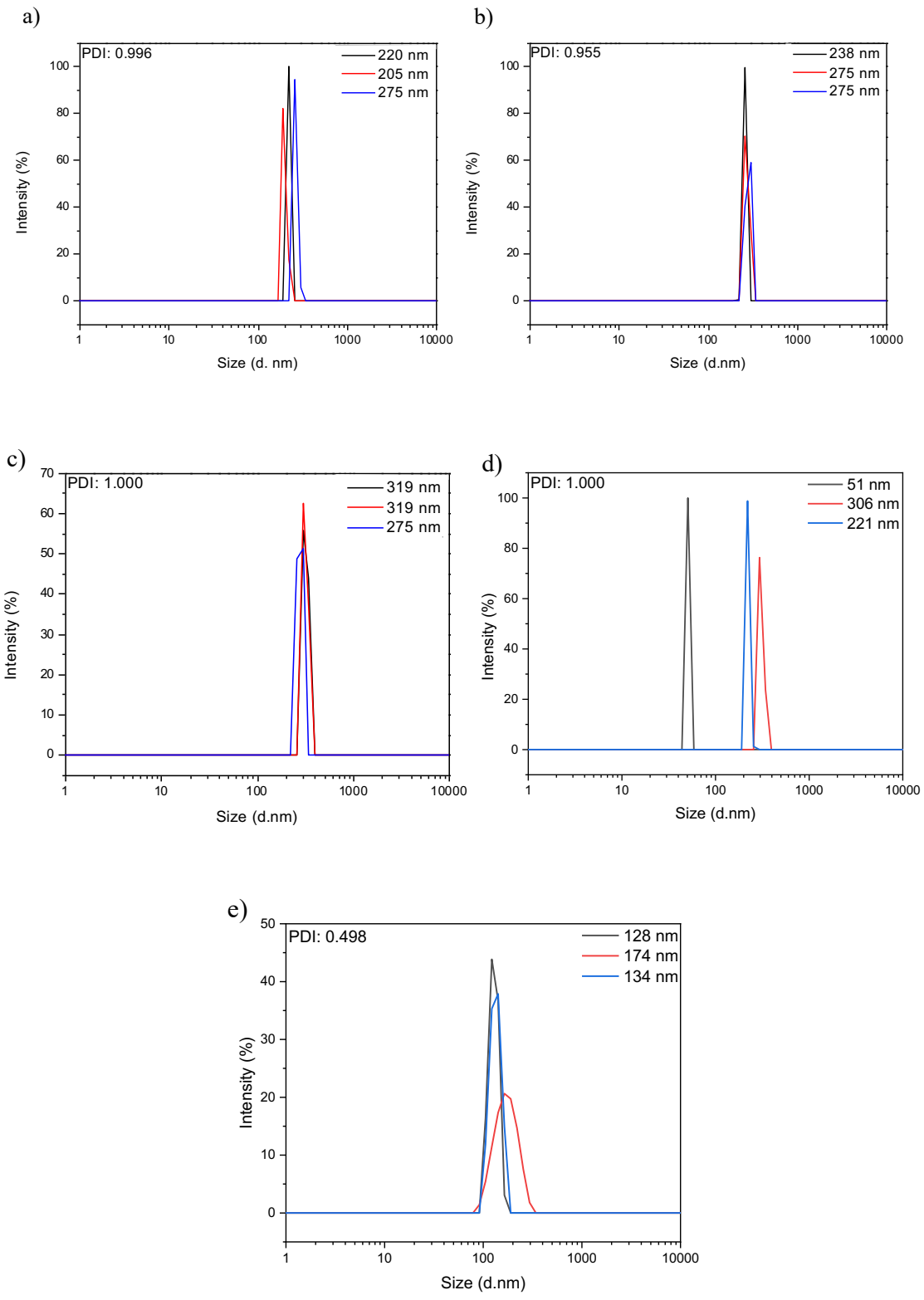

Figure 3.7. DLS plots of mixed thiolated UiO-66-$(SH)_2$ for a) 10%, b) 30%, c) 40%, d) 70%, and e) 100%.

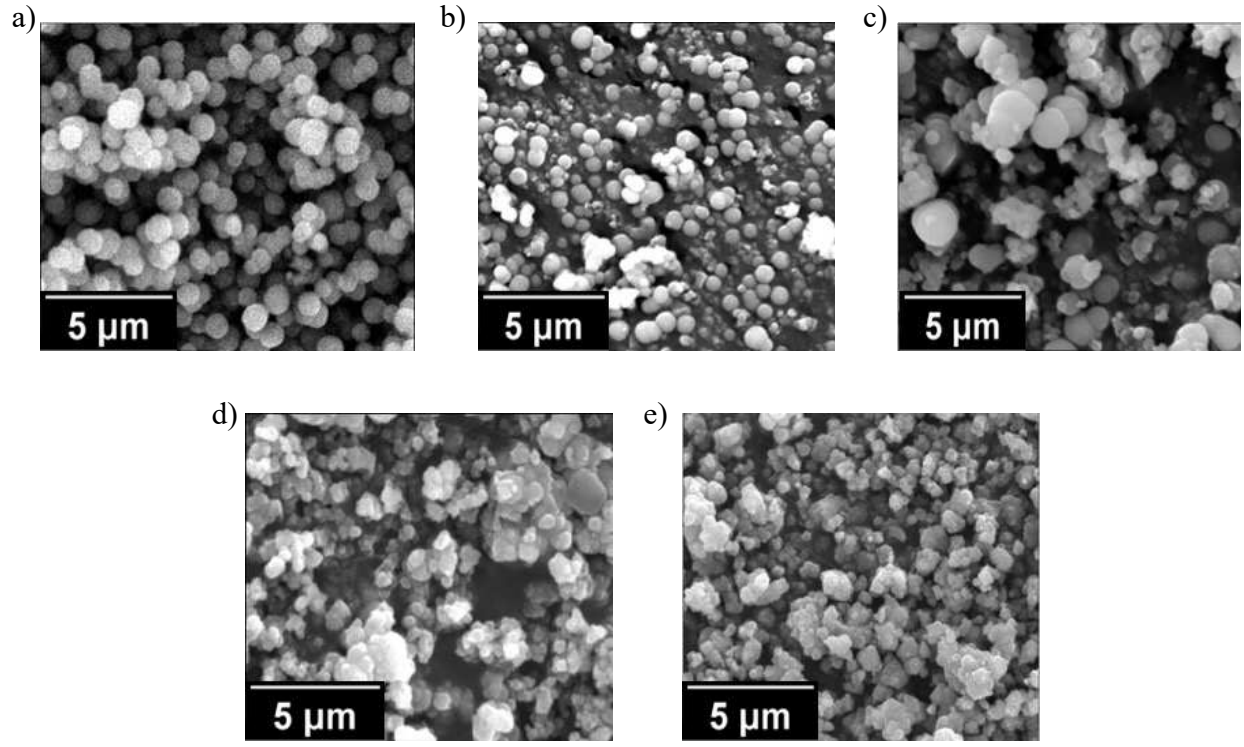

Figure 3.8. SEM micrographs of mixed thiolated UiO-66-$(SH)_2$ for a) 10%, b) 30%, c) 40%, d) 70%, and e) 100%.

3.4. Mucoadhesion Characterization

3.4.1. Thiol Quantification by UV–visible Spectroscopy

In order to quantify the number of thiol groups present on the surface of the mixed linker MOFs, a thiol quantification by Ellman's test is performed and analyzed by UV–visible spectroscopy. Refer to section 2.4.1 for detailed explanation on this characterization technique. Table 3.1 showcases the results obtained comparing the moles of thiol by ^{1}H-NMR and UV–vis spectroscopy for the mixed thiolated MOFs (10%, 30%, 40%, 70%, 100%). The moles of thiol determined by ^{1}H-NMR spectroscopy represent total number of moles of thiol in the MOF samples, whereas the moles of thiol determined by UV–Vis spectroscopy represent the number of thiol groups accessible on the external surface of the MOF. It is thus expected to observe a lower amount of moles of thiol by UV–Vis spectroscopy and a higher amount of moles of thiol determined by ^{1}H-NMR spectroscopy. In addition, the DTNB reagent with dimensions of ~ 17 Å x 6 Å is too large to be encapsulated in the pores of the MOF, much like the mucins.

Table 3.1. Theoretical and experimental moles of thiol determined by ^{1}H-NMR and UV–Vis respectively, for the mixed thiolated MOFs calculated based on the absorbance of TNB at 400 nm.

Mixed Thiolated Sample (%)	Moles of Thiol by ^{1}H-NMR/mg of MOF	Moles of Thiol by UV–Vis (surface thiols only)/mg of MOF
10	7.04×10^{-7}	5.00×10^{-8}
30	2.02×10^{-6}	1.60×10^{-8}
40	2.55×10^{-6}	9.00×10^{-9}
70	4.39×10^{-6}	2.30×10^{-8}
100	5.83×10^{-6}	4.80×10^{-8}

As expected, the total moles of thiol in the MOF increases consistently as more thiolated linker is incorporated. In addition, when comparing the moles of thiols between ^{1}H-NMR and UV–vis spectroscopy, there are less moles of thiol on the surface of the MOF compared to throughout the entire structure. Given that the moles of surface thiols determined by UV–vis spectroscopy do not demonstrate a trend, it suggests that the distribution of BDC vs BDC-$(SH)_2$ linkers throughout the MOFs (surface vs interior) is variable.

3.4.2. Periodic-Acid/Schiff's Reagent Coloration Protocol

Described as a colorimetric quantification process, PAS coloration assesses the percentage of mucins retained by the mixed linker MOF samples determined by UV–Vis spectroscopy. Refer to Section 2.4.2. for detailed explanation on this characterization technique.

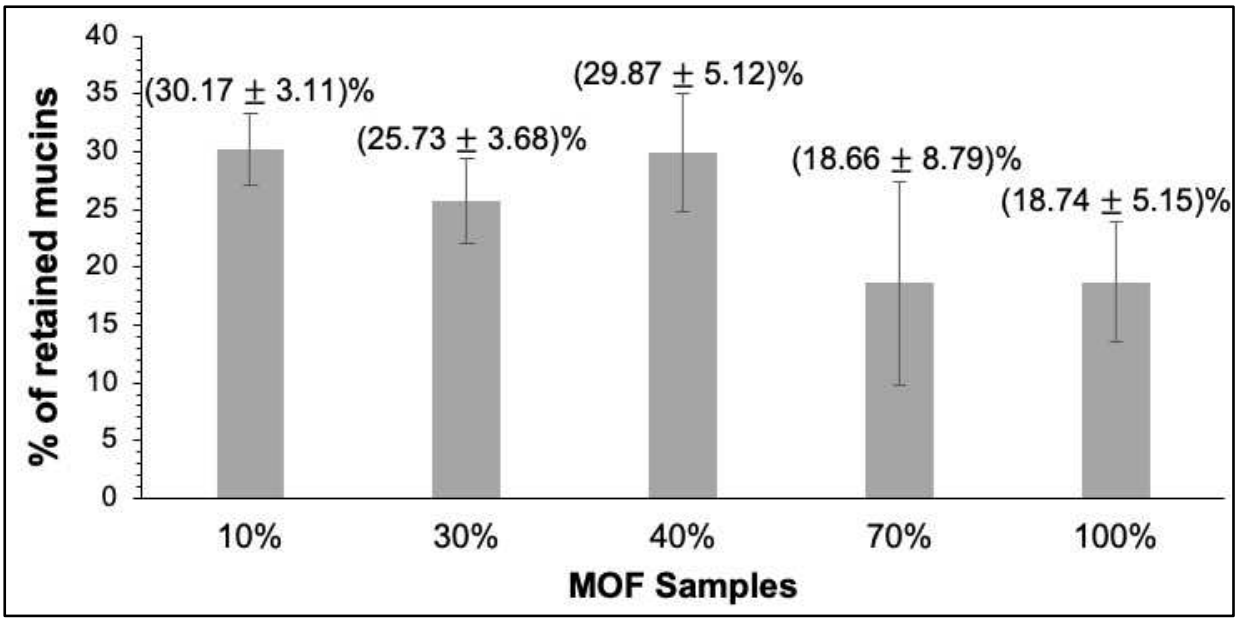

Figure 3.9. Periodic Acid-Schiff (PAS) colorimetric quantification representing % mucins retained to the mixed thiolated MOFs. 0.1 mg/mL of MOF was used in each case to prevent aggregation and to observe a difference in the retained mucins.

Based on the PAS coloration data (Figure 3.9), the MOFs are highly mucoadhesive. Although there is no trend observed for the percentage of retained mucins with increasing percentage of thiolated linker, this is consistent with the Ellman's test result suggesting that there is no trend in the number of accessible surface thiol groups. In other words, the number of mucins able to interact with the different thiol groups on the MOFs should be directly related to the number of available surface thiols. Therefore, if we observe the same order of magnitude of thiols on the periphery of the samples (observed with thiol quantification results in Table 3.1), then the % of retained mucins on all the samples should also be similar. The mucins are large proteins, highly glycosylated with an extended protein structure that can protrude 200-500 nm above the cell surface, making it too large to fit into the pores of the MOFs, confirming that it is only the surface thiols capable of interacting with the mucins. This suggests that by having a similar concentration of accessible surface thiols among all mixed thiolated samples the mucoadhesion is 20-30% on average. Given that the 10% mixed linker sample shows the highest mucoadhesion, having less thiols overall but more accessible surface thiols than other samples, it may be preferrable for the final application. It is possible that having less thiols in the MOFs overall leads to less S-S bonding and aggregation between MOF crystallites, ultimately leading to the same (or higher) number of

accessible thiols on the surface compared to the 100% thiolated sample. Owing to the fluorescent interferences from the MOF (Figure A.11), the fluorescence spectroscopy protocol cannot be used to quantify the strength of the mucoadhesion interaction for these samples.

3.5. Conclusion

In conclusion, mixed linker UiO-66-$(SH)_2$ was synthesized and characterized, and offers a possible solution for use in ophthalmic drug delivery applications. The crystalline framework and phase purity of mixed linker UiO-66-$(SH)_2$ is confirmed by PXRD and the surface area and porosity is confirmed by N_2 sorption experiments. Particle size analysis with DLS and SEM suggest that the samples are aggregated, which may be caused by disulfide bonding between MOF crystallites when more thiolated linker is added. The PAS coloration data suggests that by having a similar concentration of accessible surface thiols on all the mixed linker MOFs, the mucoadhesion does not change significantly and results in 20-30% mucoadhesion. Therefore, it is possible that having less thiols present in the mixed thiolated MOFs, (i.e., 10% mixed thiolated MOF), it can be beneficial to ensure minimal particle aggregation with high mucoadhesion and increased drug delivery capacity.

Chapter 4

Conclusions and Future Outlooks

4.1. Conclusions

The research explores synthetic approaches for enhancing the mucoadhesive properties in metal–organic frameworks (MOFs) towards their use as drug vectors for ophthalmic drug delivery. MOFs offer a novel and alternative platform for ophthalmic drug delivery with the potential to reduce the frequency of drug administration and increase drug retention times for improved patient experience. The potential of Zr-based MOFs for ophthalmic drug delivery was explored, including synthetic methods to expand the library of MOFs for this application by post-synthetic modification of open-metal sites in MOFs with thiolated ligands, or through mixed-linker MOFs. The design and synthesis of nanosized Zr-based MOFs (MOF-808, UiO-66, UiO-67, and a series of mixed linker UiO-66-$(SH)_2$) has been successfully achieved and the materials fully characterized, demonstrating crystallinity and accessible surface areas and pores. The mucoadhesive properties of all MOFs were studied using PAS coloration and when possible, fluorescence spectroscopy. All MOFs studied herein exhibit mucoadhesive properties, with the number of accessible thiol groups on the MOF surface playing a notable role in the degree of mucoadhesion.

4.2. Future Outlooks

Based on the results in this thesis, as well as previous work in the group, incorporating thiol groups in MOFs appears to be a valid strategy for achieving strong mucoadhesion. In some cases, such as that of MOF-808, thiol groups are not necessary to improve mucoadhesion, although the exact nature of the interaction between MOF-808 and mucins is not clear. Moving forward, the key is to find a balance between mucoadhesion properties (which may include the addition of thiol groups) and drug loading capacity. That being said, synthesizing an organic linker with only one thiol group, such as BDC-SH instead of two (i.e., BDC-$(SH)_2$) may help with the incorporation of thiols while maintaining access to the MOF pores for the drug delivery. Synthesizing mixed linker UiO-67-$(SH)_2$ incorporating both biphenyl-4,4-dicarboxylic acid and increasing incorporations of 3,3'-dimercapto-1,4-benzenedicarboxylic acid may also be of interest for improving the accessible pores for the drug delivery due to the use of a longer linker. In addition, determining a synthetic

protocol for thiolating the tritopic 1,3,5-benzenetricarboxylic acid of MOF-808 is of interest to have a thiol-functionalized Zr-based MOF library to compare the effect of larger pore sizes on mucoadhesion and drug loading.

In order to fully reach the objectives on the overall outlook of this project, further efforts should be geared towards studying the post-synthetic surface functionalization of the thiolated MOFs with polyethylene glycol (PEG) in order to improve the biocompatibility and stability of Zr-based MOFs in phosphate buffers and biological environments. Additionally, through the use of reticular chemistry, the pore sizes can be tailored to encapsulate and deliver a variety of ophthalmic drugs for glaucoma such as bimatoprost (~ 15 Å x 9 Å) and travoprost (~ 13 Å x 10 Å).

Lastly, owing to the high modularity of MOFs, the metal nodes can be tuned to include rare-earth metals or lanthanoids such as Eu(III) and Tb(III), to obtain materials with metal-based luminescence properties and extend the applications of MOFs to other areas of ophthalmic therapy such as neurotransmitter detection and imaging.

References

(1) Bowman-James, K. Alfred Werner Revisited: The Coordination Chemistry of Anions. *Acc. Chem. Res.* **2005**, *38* (8), 671–678. https://doi.org/10.1021/ar040071t.

(2) Kitagawa, S.; Kitaura, R.; Noro, S. Functional Porous Coordination Polymers. *Angew. Chem. Intl. Edit.* **2004**, *43* (18), 2334–2375. https://doi.org/10.1002/anie.200300610.

(3) Tomic, E. A. Thermal Stability of Coordination Polymers. *J. Appl. Polym. Sci.* **1965**, *9* (11), 3745–3752. https://doi.org/10.1002/app.1965.070091121.

(4) Hoskins, B. F.; Robson, R. Design and Construction of a New Class of Scaffolding-like Materials Comprising Infinite Polymeric Frameworks of 3D-Linked Molecular Rods. A Reappraisal of the Zinc Cyanide and Cadmium Cyanide Structures and the Synthesis and Structure of the Diamond-Related Frameworks $[N(CH_3)_4][CuIZnII(CN)_4]$ and CuI[4,4',4'',4'''-Tetracyanotetraphenylmethane]$BF_4.XC_6H_5NO_2$. *J. Am. Chem. Soc.* **1990**, *112* (4), 1546–1554. https://doi.org/10.1021/ja00160a038.

(5) Yaghi, O. M.; Li, H. Hydrothermal Synthesis of a Metal-Organic Framework Containing Large Rectangular Channels. *J. Am. Chem. Soc.* **1995**, *117* (41), 10401–10402. https://doi.org/10.1021/ja00146a033.

(6) Yaghi, O. M.; Li, G.; Li, H. Selective Binding and Removal of Guests in a Microporous Metal–Organic Framework. *Nature* **1995**, *378* (6558), 703–706. https://doi.org/10.1038/378703a0.

(7) Li, H.; Eddaoudi, M.; O'Keeffe, M.; Yaghi, O. M. Design and Synthesis of an Exceptionally Stable and Highly Porous Metal-Organic Framework. *Nature* **1999**, *402* (6759), 276–279. https://doi.org/10.1038/46248.

(8) Batten, S. R.; Champness, N.R.; Chen, X.-M.; Garcia-Martinez, J.; Kitagawa, S.; Öhrström, L.; O'Keeffe, M.; Paik Suh, M.; Reedijk, J. Coordination Polymers , Metal–Organic Frameworks and the Need for Terminology Guidelines. *Cryst. Eng. Comm.* **2012**, *14* (9), 3001–3004. https://doi.org/10.1039/C2CE06488J.

(9) Batten, S. R.; Champness, N. R.; Chen, X.-M.; Garcia-Martinez, J.; Kitagawa, S.; Öhrström, L.; O'Keeffe, M.; Suh, M. P.; Reedijk, J. Terminology of metal–organic frameworks and

coordination polymers (IUPAC Recommendations 2013). *Pure Appl. Chem.* **2013**, *85* (8), 1715–1724. https://doi.org/10.1351/PAC-REC-12-11-20.

(10) Yuan, S.; Qin, J.-S.; Lollar, C. T.; Zhou, H.-C. Stable Metal–Organic Frameworks with Group 4 Metals: Current Status and Trends. *ACS Cent. Sci.* **2018**, *4* (4), 440–450. https://doi.org/10.1021/acscentsci.8b00073.

(11) Jiang, H.-L.; Makal, T. A.; Zhou, H.-C. Interpenetration Control in Metal–Organic Frameworks for Functional Applications. *Coord. Chem. Rev.* **2013**, *257* (15–16), 2232–2249. https://doi.org/10.1016/j.ccr.2013.03.017.

(12) Rosi, N. L.; Kim, J.; Eddaoudi, M.; Chen, B.; O'Keeffe, M.; Yaghi, O. M. Rod Packings and Metal−Organic Frameworks Constructed from Rod-Shaped Secondary Building Units. *J. Am. Chem. Soc.* **2005**, *127* (5), 1504–1518. https://doi.org/10.1021/ja045123o.

(13) Li, J-R.; Kuppler, R.J.; Zhou, H-C. Selective gas adsorption and separation in metal–organic frameworks. *Chem. Soc. Rev.* **2009***, 38,* 1477–1504. https://doi.org/10.1039/b802426j.

(14) Li, H.; Li, L.; Lin, R-B.; Zhou, W.; Zhang, Z.; Xiang, S.; Chem, B. Porous metal-organic frameworks for gas storage and separation: Status and challenges *Energy Chem*. **2019**, *1*(1), 100006(1-39). https://doi.org/10.1016/j.enchem.

(15) D'Alessandro, D. M.; Smit, B.; Long, J. R. Carbon Dioxide Capture: Prospects for New Materials. *Angew. Chem. Int. Ed. Engl.* **2010**, *49* (35), 6058–6082. https://doi.org/10.1002/anie.201000431.

(16) Horcajada, P.; Serre, C.; Vallet-Regí, M.; Sebban, M.; Taulelle, F.; Férey, G. Metal-Organic Frameworks as Efficient Materials for Drug Delivery. *Angew. Chem. Int. Ed. Engl.* **2006**, *45* (36), 5974–5978. https://doi.org/10.1002/anie.200601878.

(17) Lawson, H. D.; Walton, S. P.; Chan, C. Metal–Organic Frameworks for Drug Delivery: A Design Perspective. *ACS Appl. Mater. Interfaces.* **2021**, *13* (6), 7004–7020. https://doi.org/10.1021/acsami.1c01089.

(18) Isaeva, V. I.; Kustov, L. M. The Application of Metal-Organic Frameworks in Catalysis (Review). *Pet. Chem.* **2010**, *50* (3), 167–180. https://doi.org/10.1134/S0965544110030011.

(19) Xu, C.; Fang, R.; Luque, R.; Chen, L.; Li, Y. Functional Metal–Organic Frameworks for Catalytic Applications. *Coord. Chem. Rev.* **2019**, *388*, 268–292. https://doi.org/10.1016/j.ccr.2019.03.005.

(20) Bhattacharjee, S.; Lee, Y.-R.; Puthiaraj, P.; Cho, S.-M.; Ahn, W.-S. Metal–Organic Frameworks for Catalysis. *Catal. Surv. Asia.* **2015**, *19* (4), 203–222. https://doi.org/10.1007/s10563-015-9195-1.

(21) Gao, Q.; Xu, J.; Bu, X.-H. Recent Advances about Metal–Organic Frameworks in the Removal of Pollutants from Wastewater. *Coord. Chem. Rev.* **2019**, *378*, 17–31. https://doi.org/10.1016/j.ccr.2018.03.015.

(22) Rojas, S.; Horcajada, P. Metal–Organic Frameworks for the Removal of Emerging Organic Contaminants in Water. *Chem. Rev*. **2020**, *120* (16) 8378–8415.https://doi.org/10.1021/acs.chemrev.9b00797.

(23) Howarth, A.J.; Liu, Y.; Hupp, J.T.; Farha, O.K. Metal–organic frameworks for applications in remediation of oxyanion/cation-contaminated water. *Cryst. Eng. Comm.* **2015**, *17*, 7245–7253. https://doi.org/1039/C5CE01428J.

(24) Liu, Y.; Howarth, A. J.; Vermeulen, N. A.; Moon, S.-Y.; Hupp, J. T.; Farha, O. K. Catalytic Degradation of Chemical Warfare Agents and Their Simulants by Metal-Organic Frameworks. *Coord. Chem. Rev.* **2017**, *346*, 101–111. https://doi.org/10.1016/j.ccr.2016.11.008.

(25) Mondloch, J. E.; Katz, M. J.; Isley III, W. C.; Ghosh, P.; Liao, P.; Bury, W.; Wagner, G. W.; Hall, M. G.; DeCoste, J. B.; Peterson, G. W.; Snurr, R. Q.; Cramer, C. J.; Hupp, J. T.; Farha, O. K. Destruction of Chemical Warfare Agents Using Metal–Organic Frameworks. *Nature Mater*. **2015**, *14* (5), 512–516. https://doi.org/10.1038/nmat4238.

(26) Kim, D.; Liu, X.; Lah, M. S. Topology Analysis of Metal–Organic Frameworks Based on Metal–Organic Polyhedra as Secondary or Tertiary Building Units. *Inorg. Chem. Front.* **2015**, *2* (4), 336–360. https://doi.org/10.1039/C4QI00236A.

(27) Yaghi, O. M.; O'Keeffe, M.; Ockwig, N. W.; Chae, H. K.; Eddaoudi, M.; Kim, J. Reticular Synthesis and the Design of New Materials. *Nature* **2003**, *423* (6941), 705–714. https://doi.org/10.1038/nature01650.

(28) O'Keeffe, M.; Peskov, M. A.; Ramsden, S. J.; Yaghi, O. M. The Reticular Chemistry Structure Resource (RCSR) Database of, and Symbols for, Crystal Nets. *Acc. Chem. Res.* **2008**, *41* (12), 1782–1789. https://doi.org/10.1021/ar800124u.

(29) Kökçam-Demir, Ü.; Goldman, A.; Esrafili, L.; Gharib, M.; Morsali, A.; Weingart, O.; Janiak, C. Coordinatively Unsaturated Metal Sites (Open Metal Sites) in Metal–Organic Frameworks: Design and Applications. *Chem. Soc. Rev.* **2020**, *49* (9), 2751–2798. https://doi.org/10.1039/C9CS00609E.

(30) Chiu, S.S.-Y.; Lo, S.M.-F.; Charmant, J.P.H.; Orpen, A.G.; Williams, I.D. A Chemically Functionalizable Nanoporous Material $[Cu_3(TMA)_2(H_2O)_3]n$. *Science*. **1999**, 283, 1148–1150. https://doi.org/10.1126/science.283.5405.1148.

(31) Kalaj, M.; Cohen, S. M. Postsynthetic Modification: An Enabling Technology for the Advancement of Metal–Organic Frameworks. *ACS Cent. Sci.* **2020**, *6* (7), 1046–1057. https://doi.org/10.1021/acscentsci.0c00690.

(32) Wang, Z.; M. Cohen, S. Postsynthetic Modification of Metal–Organic Frameworks. *Chem .Soc. Rev.* **2009**, *38* (5), 1315–1329. https://doi.org/10.1039/B802258P.

(33) Tanabe, K. K.; Cohen, S. M. Postsynthetic Modification of Metal–Organic Frameworks—a Progress Report. *Chem. Soc. Rev.* **2011**, *40* (2), 498–519. https://doi.org/10.1039/C0CS00031K.

(34) Marshall, R. J.; Forgan, R. S. Postsynthetic Modification of Zirconium Metal-Organic Frameworks. *Eur. J. Inorg. Chem.* **2016**, *2016* (27), 4310–4331. https://doi.org/10.1002/ejic.201600394.

(35) Karagiaridi, O.; Bury, W.; Mondloch, J. E.; Hupp, J. T.; Farha, O. K. Solvent-Assisted Linker Exchange: An Alternative to the *De Novo* Synthesis of Unattainable Metal–Organic Frameworks. *Angew. Chem. Int. Edit.* **2014**, *53* (18), 4530–4540. https://doi.org/10.1002/anie.201306923.

(36) Howarth, A. J.; Peters, A. W.; Vermeulen, N. A.; Wang, T. C.; Hupp, J. T.; Farha, O. K. Best Practices for the Synthesis, Activation, and Characterization of Metal–Organic Frameworks. *Chem. Mater.* **2017**, *29* (1), 26–39. https://doi.org/10.1021/acs.chemmater.6b02626.

(37) Deria, P.; Mondloch, J. E.; Karagiaridi, O.; Bury, W.; Hupp, J. T.; Farha, O. K. Beyond Post-Synthesis Modification: Evolution of Metal–Organic Frameworks via Building Block Replacement. *Chem. Soc. Rev.* **2014**, *43* (16), 5896–5912. https://doi.org/10.1039/C4CS00067F.

(38) Deria, P.; Bury, W.; Hod, I.; Kung, C.-W.; Karagiaridi, O.; Hupp, J. T.; Farha, O. K. MOF Functionalization via Solvent-Assisted Ligand Incorporation: Phosphonates vs Carboxylates. *Inorg. Chem.* **2015**, *54* (5), 2185–2192. https://doi.org/10.1021/ic502639v.

(39) Deria, P.; Bury, W.; Hupp, J. T.; Farha, O. K. Versatile Functionalization of the NU-1000 Platform by Solvent-Assisted Ligand Incorporation. *Chem. Commun.* **2014**, *50* (16), 1965. https://doi.org/10.1039/c3cc48562e.

(40) Farha, O. K.; Hupp, J. T.; Deria, P. Metal-Organic Framework Compounds with Ligand-Functionalized Metal Nodes. US9610560B2, April 4, 2017. https://patents.google.com/patent/US9610560B2/en (accessed 2023-04-16).

(41) Deria, P.; Mondloch, J. E.; Tylianakis, E.; Ghosh, P.; Bury, W.; Snurr, R. Q.; Hupp, J. T.; Farha, O. K. Perfluoroalkane Functionalization of NU-1000 via Solvent-Assisted Ligand Incorporation: Synthesis and CO_2 Adsorption Studies. *J. Am. Chem. Soc.* **2013**, *135* (45), 16801–16804. https://doi.org/10.1021/ja408959g.

(42) Bai, Y.; Dou, Y.; Xie, L.-H.; Rutledge, W.; Li, J.-R.; Zhou, H.-C. Zr-Based Metal–Organic Frameworks: Design, Synthesis, Structure, and Applications. *Chem. Soc. Rev.* **2016**, *45* (8), 2327–2367. https://doi.org/10.1039/C5CS00837A.

(43) Furukawa, H.; Gándara, F.; Zhang, Y.-B.; Jiang, J.; Queen, W. L.; Hudson, M. R.; Yaghi, O. M. Water Adsorption in Porous Metal–Organic Frameworks and Related Materials. *J. Am. Chem. Soc.* **2014**, *136* (11), 4369–4381. https://doi.org/10.1021/ja500330a.

(44) Moon, S.-Y.; Liu, Y.; Hupp, J. T.; Farha, O. K. Instantaneous Hydrolysis of Nerve-Agent Simulants with a Six-Connected Zirconium-Based Metal–Organic Framework. *Angew. Chem.* **2015**, *127* (23), 6899–6903. https://doi.org/10.1002/ange.201502155.

(45) Aunan, E.; Affolter, C. W.; Olsbye, U.; Lillerud, K. P. Modulation of the Thermochemical Stability and Adsorptive Properties of MOF-808 by the Selection of Non-Structural Ligands. *Chem. Mater.* **2021**, *33* (4), 1471–1476. https://doi.org/10.1021/acs.chemmater.0c04823.

(46) Dai, S.; Simms, C.; Dovgaliuk, I.; Patriarche, G.; Tissot, A.; Parac-Vogt, T. N.; Serre, C. Monodispersed MOF-808 Nanocrystals Synthesized via a Scalable Room-Temperature Approach for Efficient Heterogeneous Peptide Bond Hydrolysis. *Chem. Mater.* **2021**, *33* (17), 7057–7066. https://doi.org/10.1021/acs.chemmater.1c02174.

(47) Suárez-Ardila, C.; Molina, V.; D.R.; Alem, H.; Baldovino-Medrano, V.G.; Ramírez-Caballero, G.E. Synthesis of Ordered Microporous/Macroporous MOF-808 through Modulator-Induced Defect Formation, and Surfactant Self-Assembly Strategies. *Mater. Sci.* **2020**, *22* (22). https://doi.org/10.26434/chemrxiv.10316924.v1.

(48) Winarta, J.; Shan, B.; Mcintyre, S. M.; Ye, L.; Wang, C.; Liu, J.; Mu, B. A Decade of UiO-66 Research: A Historic Review of Dynamic Structure, Synthesis Mechanisms, and Characterization Techniques of an Archetypal Metal–Organic Framework. *Crys. Growth Des.* **2020**, *20* (2), 1347–1362. https://doi.org/10.1021/acs.cgd.9b00955.

(49) Garibay, S. J.; Cohen, S. M. Isoreticular Synthesis and Modification of Frameworks with the UiO-66 Topology. *Chem. Commun.* **2010**, *46* (41), 7700. https://doi.org/10.1039/c0cc02990d.

(50) Cavka, J. H.; Jakobsen, S.; Olsbye, U.; Guillou, N.; Lamberti, C.; Bordiga, S.; Lillerud, K. P. A New Zirconium Inorganic Building Brick Forming Metal Organic Frameworks with Exceptional Stability. *J. Am. Chem. Soc.* **2008**, *130* (42), 13850–13851. https://doi.org/10.1021/ja8057953.

(51) Wu, H.; Chua, Y. S.; Krungleviciute, V.; Tyagi, M.; Chen, P.; Yildirim, T.; Zhou, W. Unusual and Highly Tunable Missing-Linker Defects in Zirconium Metal–Organic Framework UiO-66 and Their Important Effects on Gas Adsorption. *J. Am. Chem. Soc.* **2013**, *135* (28), 10525–10532. https://doi.org/10.1021/ja404514r.

(52) Trickett, C. A.; Gagnon, K. J.; Lee, S.; Gándara, F.; Bürgi, H.-B.; Yaghi, O. M. Definitive Molecular Level Characterization of Defects in UiO-66 Crystals. *Angew. Chem. Int. Edit.* **2015**, *54* (38), 11162–11167. https://doi.org/10.1002/anie.201505461.

(53) Katz, M. J.; Brown, Z. J.; Colón, Y. J.; Siu, P. W.; Scheidt, K. A.; Snurr, R. Q.; Hupp, J. T.; Farha, O. K. A Facile Synthesis of UiO-66, UiO-67 and Their Derivatives. *Chem. Commun.* **2013**, *49* (82), 9449. https://doi.org/10.1039/c3cc46105j.

(54) Kaur, G.; Øien-Ødegaard, S.; Lazzarini, A.; Chavan, S. M.; Bordiga, S.; Lillerud, K. P.; Olsbye, U. Controlling the Synthesis of Metal–Organic Framework UiO-67 by Tuning Its Kinetic Driving Force. *Crys. Growth Des.* **2019**, *19* (8), 4246–4251. https://doi.org/10.1021/acs.cgd.9b00916.

(55) Chavan, S.; Vitillo, J. G.; Gianolio, D.; Zavorotynska, O.; Civalleri, B.; Jakobsen, S.; Nilsen, M. H.; Valenzano, L.; Lamberti, C.; Lillerud, K. P.; Bordiga, S. H_2 Storage in Isostructural UiO-67 and UiO-66 MOFs. *Phys. Chem. Chem. Phys.* **2012**, *14* (5), 1614–1626. https://doi.org/10.1039/C1CP23434J.

(56) Fan, W.; Zhang, X.; Kang, Z.; Liu, X.; Sun, D. Isoreticular Chemistry within Metal–Organic Frameworks for Gas Storage and Separation. *Coord. Chem. Rev.* **2021**, *443*, 213968. https://doi.org/10.1016/j.ccr.2021.213968.

(57) Eddaoudi, M.; Kim, J.; Rosi, N.; Vodak, D.; Wachter, J.; O'Keeffe, M.; Yaghi, O. M. Systematic Design of Pore Size and Functionality in Isoreticular MOFs and Their Application in Methane Storage. *Science* **2002**, *295* (5554), 469–472. https://doi.org/10.1126/science.1067208.

(58) Mai, Z.; Liu, D. Synthesis and Applications of Isoreticular Metal–Organic Frameworks IRMOFs- *n* (*n* = 1, 3, 6, 8). *Crys. Growth Des.* **2019**, *19* (12), 7439–7462. https://doi.org/10.1021/acs.cgd.9b00879.

(59) Lee, J.; Farha, O. K.; Roberts, J.; Scheidt, K. A.; Nguyen, S. T.; Hupp, J. T. Metal–Organic Framework Materials as Catalysts. *Chem. Soc. Rev.* **2009**, *38* (5), 1450. https://doi.org/10.1039/b807080f.

(60) Jiao, L.; Wang, Y.; Jiang, H.-L.; Xu, Q. Metal–Organic Frameworks as Platforms for Catalytic Applications. *Adv. Mat.* **2018**, *30* (37), 1703663. https://doi.org/10.1002/adma.201703663.

(61) Varnaseri, N.; Rouhani, F.; Ramazani, A.; Morsali, A. Size and Function Influence Study on Enhanced Catalytic Performance of a Cooperative MOF for Mild, Green and Fast C–C Bond Formation. *Dalton Trans.* **2020**, *49* (10), 3234–3242. https://doi.org/10.1039/D0DT00433B.

(62) Liu, S.; Sun, L.; Xu, F.; Zhang, J.; Jiao, C.; Li, F.; Li, Z.; Wang, S.; Wang, Z.; Jiang, X.; Zhou, H.; Yang, L.; Schick, C. Nanosized Cu-MOFs Induced by Graphene Oxide and

Enhanced Gas Storage Capacity. *Energy Environ. Sci.* **2013**, *6* (3), 818. https://doi.org/10.1039/c3ee23421e.

(63) Zhao, X.; Wang, Y.; Li, D.-S.; Bu, X.; Feng, P. Metal–Organic Frameworks for Separation. *Adv. Mat.* **2018**, *30* (37), 1705189. https://doi.org/10.1002/adma.201705189.

(64) Yang, J.; Wang, H.; Liu, J.; Ding, M.; Xie, X.; Yang, X.; Peng, Y.; Zhou, S.; Ouyang, R.; Miao, Y. Recent Advances in Nanosized Metal Organic Frameworks for Drug Delivery and Tumor Therapy. *RSC Adv.* **2021**, *11* (6), 3241–3263. https://doi.org/10.1039/D0RA09878G.

(65) Horcajada, P.; Gref, R.; Baati, T.; Allan, P. K.; Maurin, G.; Couvreur, P.; Férey, G.; Morris, R. E.; Serre, C. Metal–Organic Frameworks in Biomedicine. *Chem. Rev.* **2012**, *112* (2), 1232–1268. https://doi.org/10.1021/cr200256v.

(66) Abánades Lázaro, I.; Forgan, R. S. Application of Zirconium MOFs in Drug Delivery and Biomedicine. *Coord. Chem. Rev.* **2019**, *380*, 230–259. https://doi.org/10.1016/j.ccr.2018.09.009.

(67) Wu, M.-X.; Yang, Y.-W. Metal–Organic Framework (MOF)-Based Drug/Cargo Delivery and Cancer Therapy. *Adv. Mat.* **2017**, *29* (23), 1606134. https://doi.org/10.1002/adma.201606134.

(68) Cai, X.; Xie, Z.; Li, D.; Kassymova, M.; Zang, S.-Q.; Jiang, H.-L. Nano-Sized Metal-Organic Frameworks: Synthesis and Applications. *Coord. Chem. Rev.* **2020**, *417*, 213366. https://doi.org/10.1016/j.ccr.2020.213366.

(69) Khan, N. A.; Hasan, Z.; Jhung, S. H. Beyond Pristine Metal-Organic Frameworks: Preparation and Application of Nanostructured, Nanosized, and Analogous MOFs. *Coord. Chem. Rev.* **2018**, *376*, 20–45. https://doi.org/10.1016/j.ccr.2018.07.016.

(70) Majewski, M. B.; Noh, H.; Islamoglu, T.; Farha, O. K. NanoMOFs: Little Crystallites for Substantial Applications. *J. Mater. Chem. A* **2018**, *6* (17), 7338–7350. https://doi.org/10.1039/C8TA02132E.

(71) Lan, X.; Huang, N.; Wang, J.; Wang, T. A General and Facile Strategy for Precisely Controlling the Crystal Size of Monodispersed Metal–Organic Frameworks *via* Separating the Nucleation and Growth. *Chem. Commun.* **2018**, *54* (6), 584–587. https://doi.org/10.1039/C7CC08244D.

(72) Marshall, C. R.; Staudhammer, S. A.; Brozek, C. K. Size Control over Metal–Organic Framework Porous Nanocrystals. *Chem. Sci.* **2019**, *10* (41), 9396–9408. https://doi.org/10.1039/C9SC03802G.

(73) Stock, N.; Biswas, S. Synthesis of Metal-Organic Frameworks (MOFs): Routes to Various MOF Topologies, Morphologies, and Composites. *Chem. Rev.* **2012**, *112* (2), 933–969. https://doi.org/10.1021/cr200304e.

(74) Ni, Z.; Masel, R. I. Rapid Production of Metal−Organic Frameworks via Microwave-Assisted Solvothermal Synthesis. *J. Am. Chem. Soc.* **2006**, *128* (38), 12394–12395. https://doi.org/10.1021/ja0635231.

(75) Hartmann, M.; Kunz, S.; Himsl, D.; Tangermann, O.; Ernst, S.; Wagener, A. Adsorptive Separation of Isobutene and Isobutane on Cu_3 $(BTC)_2$. *Langmuir.* **2008**, *24* (16), 8634–8642. https://doi.org/10.1021/la8008656.

(76) Qi, F.; S. Stein, R.; Friščić, T. Mimicking Mineral Neogenesis for the Clean Synthesis of Metal–Organic Materials from Mineral Feedstocks: Coordination Polymers, MOFs and Metal Oxide Separation. *Green Chem.* **2014**, *16* (1), 121–132. https://doi.org/10.1039/C3GC41370E.

(77) Sun, Y.; Zhou, H.-C. Recent Progress in the Synthesis of Metal–Organic Frameworks. *Sci. Technol. Adv. Mat.* **2015**, *16* (5), 054202. https://doi.org/10.1088/1468-6996/16/5/054202.

(78) Seetharaj, R.; Vandana, P. V.; Arya, P.; Mathew, S. Dependence of Solvents, PH, Molar Ratio and Temperature in Tuning Metal Organic Framework Architecture. *Arab. J. Chem.* **2019**, *12* (3), 295–315. https://doi.org/10.1016/j.arabjc.2016.01.003.

(79) Karagiaridi, O.; Bury, W.; Sarjeant, A. A.; Hupp, J. T.; Farha, O. K. Synthesis and Characterization of Functionalized Metal-Organic Frameworks. *J. Vis. Exp.* **2014**, No. 91, 52094. https://doi.org/10.3791/52094.

(80) Jiang, D.; Huang, C.; Zhu, J.; Wang, P.; Liu, Z.; Fang, D. Classification and Role of Modulators on Crystal Engineering of Metal Organic Frameworks (MOFs). *Coord. Chem. Rev.* **2021**, *444*, 214064. https://doi.org/10.1016/j.ccr.2021.214064.

(81) S. Forgan, R. Modulated Self-Assembly of Metal–Organic Frameworks. *Chem. Sci.* **2020**, *11* (18), 4546–4562. https://doi.org/10.1039/D0SC01356K.

(82) Mondloch, J. E.; Karagiaridi, O.; Farha, O. K.; Hupp, J. T. Activation of Metal–Organic Framework Materials. *Cryst. Eng. Comm.* **2013**, *15* (45), 9258. https://doi.org/10.1039/c3ce41232f.

(83) Mondloch, J. E.; Katz, M. J.; Planas, N.; Semrouni, D.; Gagliardi, L.; Hupp, J. T.; Farha, O. K. Are Zr_6-Based MOFs Water Stable? Linker Hydrolysis vs. Capillary-Force-Driven Channel Collapse. *Chem. Commun.* **2014**, *50* (64), 8944. https://doi.org/10.1039/C4CC02401J.

(84) Della Rocca, J.; Liu, D.; Lin, W. Nanoscale Metal–Organic Frameworks for Biomedical Imaging and Drug Delivery. *Acc. Chem. Res.* **2011**, *44* (10), 957–968. https://doi.org/10.1021/ar200028a.

(85) Chen, X.; Zhuang, Y.; Rampal, N.; Hewitt, R.; Divitini, G.; O'Keefe, C. A.; Liu, X.; Whitaker, D. J.; Wills, J. W.; Jugdaohsingh, R.; Powell, J. J.; Yu, H.; Grey, C. P.; Scherman, O. A.; Fairen-Jimenez, D. Formulation of Metal–Organic Framework-Based Drug Carriers by Controlled Coordination of Methoxy PEG Phosphate: Boosting Colloidal Stability and Redispersibility. *J. Am. Chem. Soc.* **2021**, *143* (34), 13557–13572. https://doi.org/10.1021/jacs.1c03943.

(86) Singh, N.; Qutub, S.; Khashab, N. M. Biocompatibility and Biodegradability of Metal Organic Frameworks for Biomedical Applications. *J. Mater. Chem. B.* **2021**, *9* (30), 5925–5934. https://doi.org/10.1039/D1TB01044A.

(87) Roth Stefaniak, K.; Epley, C. C.; Novak, J. J.; McAndrew, M. L.; Cornell, H. D.; Zhu, J.; McDaniel, D. K.; Davis, J. L.; Allen, I. C.; Morris, A. J.; Grove, T. Z. Photo-Triggered Release of 5-Fluorouracil from a MOF Drug Delivery Vehicle. *Chem. Commun.* **2018**, *54* (55), 7617–7620. https://doi.org/10.1039/C8CC01601A.

(88) El-Bindary, M. A.; El-Desouky, M. G.; El-Bindary, A. A. Metal–Organic Frameworks Encapsulated with an Anticancer Compound as Drug Delivery System: Synthesis, Characterization, Antioxidant, Anticancer, Antibacterial, and Molecular Docking Investigation. *Appl. Organomet. Chem.* **2022**, *36* (5), e6660. https://doi.org/10.1002/aoc.6660.

(89) He, L.; Shang, M.; Chen, Z.; Yang, Z. Metal-Organic Frameworks Nanocarriers for Functional Nucleic Acid Delivery in Biomedical Applications. *Chem. Rec.* **2023**, *23*, e202300018 (1–15). https://doi.org/10.1002/tcr.202300018.

(90) Moharramnejad, M.; Ehsani, A.; Shahi, M.; Gharanli, S.; Saremi, H.; Malekshah, R. E.; Basmenj, Z. S.; Salmani, S.; Mohammadi, M. MOF as Nanoscale Drug Delivery Devices: Synthesis and Recent Progress in Biomedical Applications. *J. Drug Deliv. Sci. Technol.* **2023**, *81*, 104285. https://doi.org/10.1016/j.jddst.2023.104285.

(91) *Zero-Background sample holders for XRD applications | Labx Ad 14263754*. https://www.labx.com/item/zero-background-sample-holders-for-xrd-applications/14263754 (accessed 2023-04-04).

(92) Hafizovic, J.; Bjørgen, M.; Olsbye, U.; Dietzel, P. D. C.; Bordiga, S.; Prestipino, C.; Lamberti, C.; Lillerud, K. P. The Inconsistency in Adsorption Properties and Powder XRD Data of MOF-5 Is Rationalized by Framework Interpenetration and the Presence of Organic and Inorganic Species in the Nanocavities. *J. Am. Chem. Soc.* **2007**, *129* (12), 3612–3620. https://doi.org/10.1021/ja0675447.

(93) Makulski, W. Explorations of Magnetic Properties of Noble Gases: The Past, Present, and Future. *Magnetochemistry* **2020**, *6* (4), 65. https://doi.org/10.3390/magnetochemistry6040065.

(94) Pollack, G. L. The Solid State of Rare Gases. *Rev. Mod. Phys.* **1964**, *36* (3), 748–791. https://doi.org/10.1103/RevModPhys.36.748.

(95) Mikhail, R. S.; Brunauer, S. Surface Area Measurements by Nitrogen and Argon Adsorption. *J. Colloid Interf. Sci.* **1975**, *52* (3), 572–577. https://doi.org/10.1016/0021-9797(75)90282-9.

(96) Thommes, M.; Kaneko, K.; Neimark, A. V.; Olivier, J. P.; Rodriguez-Reinoso, F.; Rouquerol, J.; Sing, K. S. W. Physisorption of Gases, with Special Reference to the Evaluation of Surface Area and Pore Size Distribution (IUPAC Technical Report). *Pure Appl. Chem.* **2015**, *87* (9–10), 1051–1069. https://doi.org/10.1515/pac-2014-1117.

(97) Yahia, M. B.; Torkia, Y. B.; Knani, S.; Hachicha, M. A.; Khalfaoui, M.; Lamine, A. B. Models for Type VI Adsorption Isotherms from a Statistical Mechanical Formulation. *Adsorpt. Sci. Technol.* **2013**, *31* (4), 341–357. https://doi.org/10.1260/0263-6174.31.4.341.

(98) Kupgan, G.; Liyana-Arachchi, T. P.; Colina, C. M. NLDFT Pore Size Distribution in Amorphous Microporous Materials. *Langmuir.* **2017**, *33* (42), 11138–11145. https://doi.org/10.1021/acs.langmuir.7b01961.

(99) Wang, T. C.; Vermeulen, N. A.; Kim, I. S.; Martinson, A. B. F.; Stoddart, J. F.; Hupp, J. T.; Farha, O. K. Scalable Synthesis and Post-Modification of a Mesoporous Metal-Organic Framework Called NU-1000. *Nat. Protoc.* **2016**, *11* (1), 149–162. https://doi.org/10.1038/nprot.2016.001.

(100) Hoffmann, H.; Debowski, M.; Müller, P.; Paasch, S.; Senkovska, I.; Kaskel, S.; Brunner, E. Solid-State NMR Spectroscopy of Metal–Organic Framework Compounds (MOFs). *Materials.* **2012**, *5* (12), 2537–2572. https://doi.org/10.3390/ma5122537.

(101) Sutrisno, A.; Huang, Y. Solid-State NMR: A Powerful Tool for Characterization of Metal–Organic Frameworks. *Solid State Nuclear Magnetic Resonance.* **2013**, *49–50*, 1–11. https://doi.org/10.1016/j.ssnmr.2012.09.003.

(102) Lucier, B. E. G.; Chen, S.; Huang, Y. Characterization of Metal–Organic Frameworks: Unlocking the Potential of Solid-State NMR. *Acc. Chem. Res.* **2018**, *51* (2), 319–330. https://doi.org/10.1021/acs.accounts.7b00357.

(103) Zhang, H.; Wang, X.; Wang, J.; Chen, Q.; Huang, H.; Huang, L.; Cao, S.; Ma, X. UV–Visible Diffuse Reflectance Spectroscopy Used in Analysis of Lignocellulosic Biomass Material. *Wood Sci. Technol.* **2020**, *54* (4), 837–846. https://doi.org/10.1007/s00226-020-01199-w.

(104) Perkampus, H.-H. *UV-VIS Spectroscopy and Its Applications*; Springer Science & Business Media, 2013.

(105) Armaroli, T.; Bécue, T.; Gautier, S. Diffuse Reflection Infrared Spectroscopy (Drifts): Application to the in Situ Analysis of Catalysts. *Oil & Gas Science and Technology - Rev. IFP* **2004**, *59* (2), 215–237. https://doi.org/10.2516/ogst:2004016.

(106) Hadjiivanov, K. I.; Panayotov, D. A.; Mihaylov, M. Y.; Ivanova, E. Z.; Chakarova, K. K.; Andonova, S. M.; Drenchev, N. L. Power of Infrared and Raman Spectroscopies to Characterize Metal-Organic Frameworks and Investigate Their Interaction with Guest

Molecules. *Chem. Rev.* **2021**, *121* (3), 1286–1424. https://doi.org/10.1021/acs.chemrev.0c00487.

(107) Stetefeld, J.; McKenna, S. A.; Patel, T. R. Dynamic Light Scattering: A Practical Guide and Applications in Biomedical Sciences. *Biophys. Rev.* **2016**, *8* (4), 409–427. https://doi.org/10.1007/s12551-016-0218-6.

(108) Schaate, A.; Roy, P.; Godt, A.; Lippke, J.; Waltz, F.; Wiebcke, M.; Behrens, P. Modulated Synthesis of Zr-Based Metal-Organic Frameworks: From Nano to Single Crystals. *Chem. Eur. J.* **2011**, *17* (24), 6643–6651. https://doi.org/10.1002/chem.201003211.

(109) Gudkov, S. V.; Baimler, I. V.; Uvarov, O. V.; Smirnova, V. V.; Volkov, M. Y.; Semenova, A. A.; Lisitsyn, A. B. Influence of the Concentration of Fe and Cu Nanoparticles on the Dynamics of the Size Distribution of Nanoparticles. *Frontiers in Physics.* **2020**, *8,* 622551 (1–7). https://doi.org/10.3389/fphy.2020.622551.

(110) Danaei, M.; Dehghankhold, M.; Ataei, S.; Hasanzadeh Davarani, F.; Javanmard, R.; Dokhani, A.; Khorasani, S.; Mozafari, M. R. Impact of Particle Size and Polydispersity Index on the Clinical Applications of Lipidic Nanocarrier Systems. *Pharmaceutics.* **2018**, *10* (2), 57. https://doi.org/10.3390/pharmaceutics10020057.

(111) Bendersky, L. A.; Gayle, F. W. Electron Diffraction Using Transmission Electron Microscopy. *J. Res. Natl. Inst. Stand Technol.* **2001**, *106* (6), 997–1012. https://doi.org/10.6028/jres.106.051.

(112) D'Alfonso, A. J.; Freitag, B.; Klenov, D.; Allen, L. J. Atomic-Resolution Chemical Mapping Using Energy-Dispersive x-Ray Spectroscopy. *Phys. Rev. B.* **2010**, *81* (10), 100101. https://doi.org/10.1103/PhysRevB.81.100101.

(113) Hofer, F.; Schmidt, F. P.; Grogger, W.; Kothleitner, G. Fundamentals of Electron Energy-Loss Spectroscopy. *IOP Conf. Ser.: Mater. Sci. Eng.* **2016**, *109* (1), 012007. https://doi.org/10.1088/1757-899X/109/1/012007.

(114) Nieri, P.; Carpi, S.; Fogli, S.; Polini, B.; Breschi, M. C.; Podestà, A. Cholinesterase-like Organocatalysis by Imidazole and Imidazole-Bearing Molecules. *Sci. Rep.* **2017**, *7* (1), 45760. https://doi.org/10.1038/srep45760.

(115) Habeeb, A.F.S.A. Reaction of protein sulfhydryl groups with Ellman's reagent. *Meth. Enzymol*. **1972**, *25*, 457–464. https://doi.org/10.1016/S0076-6879(72)25041-8.

(116) Wong, T.Y.; Hyman, L. Population-Based Studies in Ophthalmology. *Am. J. Ophthal.* **2008**, *146* (5), 656–663. https://doi.org/10.1016/j.ajo.2008.07.048.

(117) Popov, A. Mucus-Penetrating Particles and the Role of Ocular Mucus as a Barrier to Micro- and Nanosuspensions. *J. Ocul. Pharmacol. Th*. **2020**, *36* (6), 366–375. https://doi/full/10.1089/jop.2020.0022.

(118) Ouellette, M.; Masse, F.; Lefebvre-Demers, M.; Maestracci, Q.; Grenier, P.; Millar, R.; Bertrand, N.; Prieto, M.; Boisselier, É. Insights into Gold Nanoparticles as a Mucoadhesive System. *Sc.i Rep.* **2018**, *8* (1), 14357. https://doi.org/10.1038/s41598-018-32699-2.

(119) Mantelli, F.; Argüeso, P. Functions of Ocular Surface Mucins in Health and Disease. *Current Opinion in Allergy & Clinical Immunology* **2008**, *8* (5), 477–483. https://doi.org/10.1097/ACI.0b013e32830e6b04.

(120) Hodges, R. R.; Dartt, D. A. Tear Film Mucins: Front Line Defenders of the Ocular Surface; Comparison with Airway and Gastrointestinal Tract Mucins. *Exp. Eye Res.* **2013**, *117*, 62–78. https://doi.org/10.1016/j.exer.2013.07.027.

(121) Bansil, R.; Turner, B. S. The Biology of Mucus: Composition, Synthesis and Organization. *Adv. Drug Deliver. Rev.* **2018**, *124*, 3–15. https://doi.org/10.1016/j.addr.2017.09.023.

(122) Mansuri, S.; Kesharwani, P.; Jain, K.; Tekade, R. K.; Jain, N. K. Mucoadhesion: A Promising Approach in Drug Delivery System. *React. Funct. Polym.* **2016**, *100*, 151–172. https://doi.org/10.1016/j.reactfunctpolym.2016.01.011.

(123) Khutoryanskiy, V. V. Advances in Mucoadhesion and Mucoadhesive Polymers. *Macromol. Biosci.* **2011**, *11* (6), 748–764. https://doi.org/10.1002/mabi.201000388.

(124) Kilcoyne, M.; Gerlach, J. Q.; Farrell, M. P.; Bhavanandan, V. P.; Joshi, L. Periodic Acid–Schiff's Reagent Assay for Carbohydrates in a Microtiter Plate Format. *Anal. Biochem.* **2011**, *416* (1), 18–26. https://doi.org/10.1016/j.ab.2011.05.006.

(125) Robins, J. H.; Abrams, G. D.; Pincock, J. A. The Structure of Schiff Reagent Aldehyde Adducts and the Mechanism of the Schiff Reaction as Determined by Nuclear Magnetic

Resonance Spectroscopy. *Can. J. Chem.* **1980**, *58* (4), 339–347. https://doi.org/10.1139/v80-055.

(126) Patel, A.; Cholkar, K.; Agrahari, V.; Mitra, A. K. Ocular Drug Delivery Systems: An Overview. *World J. Pharmacol*. **2013**, *2* (2), 47–64. https://doi.org/10.5497/wjp.v2.i2.47.

(127) Liu, Y.-C.; Wilkins, M.; Kim, T.; Malyugin, B.; Mehta, J. S. Cataracts. *The Lancet.* **2017**, *390* (10094), 600–612. https://doi.org/10.1016/S0140-6736(17)30544-5.

(128) *Cataracts - Symptoms, Causes, Diagnosis & Treatment*. https://www.visioncenter.org/conditions/cataracts/ (accessed 2023-04-20).

(129) *Cataract*. https://www.aoa.org/healthy-eyes/eye-and-vision-conditions/cataract?sso=y (accessed 2023-01-22).

(130) Gupta, V. B.; Rajagopala, M.; Ravishankar, B. Etiopathogenesis of Cataract: An Appraisal. *Indian J. Ophthalmol.* **2014**, *62* (2), 103–110. https://doi.org/10.4103/0301-4738.121141.

(131) Yu, X.; Lyu, D.; Dong, X.; He, J.; Yao, K. Hypertension and Risk of Cataract: A Meta-Analysis. *PLoS One.* **2014**, *9* (12), e114012. https://doi.org/10.1371/journal.pone.0114012.

(132) Li, Q.; Weng, J.; Wong, S. N.; Thomas Lee, W. Y.; Chow, S. F. Nanoparticulate Drug Delivery to the Retina. *Mol. Pharmaceutics.* **2021**, *18* (2), 506–521. https://doi.org/10.1021/acs.molpharmaceut.0c00224.

(133) Cheng, K-J.; Hsieh, C-M.; Nepali, K.; Liou, J-P. Ocular Disease Therapeutics: Design and Delivery of Drugs for Diseases of the Eye. *J. Med. Chem*. **2020**, *63*, 10533–10593. https://doi/full/10.1021/acs.jmedchem.9b01033.

(134) *Ocular Drug Delivery: Advances, Challenges and Applications*; Addo, R. T., Ed.; Springer International Publishing: Cham, 2016. https://doi.org/10.1007/978-3-319-47691-9.

(135) *How the Eyes Work | National Eye Institute*. https://www.nei.nih.gov/learn-about-eye-health/healthy-vision/how-eyes-work (accessed 2023-01-23).

(136) *Pupil of the Eye: Definition, Anatomy & Function*. Cleveland Clinic. https://my.clevelandclinic.org/health/body/24317-pupil-of-the-eye (accessed 2023-04-20).

(137) Ruan, X.; Liu, Z.; Luo, L.; Liu, Y. The Structure of the Lens and Its Associations with the Visual Quality. *BMJ Open Ophth.* **2020**, *5* (1), e000459. https://doi.org/10.1136/bmjophth-2020-000459.

(138) Matossian, C.; Temple University School of Medicine, Philadelphia, PA, USA. Noncompliance with Prescribed Eyedrop Regimens Among Patients Undergoing Cataract Surgery—Prevalence, Consequences, and Solutions. *US Ophthal. Rev.* **2020**, *13* (1), 18. https://doi.org/10.17925/USOR.2020.13.1.18.

(139) Yavuz, B.; Bozdağ Pehlivan, S.; Ünlü, N. Dendrimeric Systems and Their Applications in Ocular Drug Delivery. *Sci. World J.* **2013**, *2013*, 1–13. https://doi.org/10.1155/2013/732340.

(140) Morrison, P. W.; Khutoryanskiy, V. V. Advances in Ophthalmic Drug Delivery. *Ther. Deliv.* **2014**, *5* (12), 1297–1315. https://doi.org/10.4155/tde.14.75.

(141) Omerović, N.; Vranić, E. Application of Nanoparticles in Ocular Drug Delivery Systems. *Health Technol.* **2020**, *10* (1), 61–78. https://doi.org/10.1007/s12553-019-00381-w.

(142) Dartt, D.; Willcox, M. Complexity of the Tear Film: Importance in Homeostasis and Dysfunction during Disease. *Exp. Eye Res.* **2013**, *117*, 1–3. https://doi.org/10.1016/j.exer.2013.10.008.

(143) Yoshida, M.; Yamaguchi, M.; Sato, A.; Tabuchi, N.; Kon, R.; limura, K-i. Role of Endogenous Ingredients in Meibum and Film Structures on Stability of the Tear Film Lipid Layer against Lateral Compression. *Langmuir*, **2019**, *35* (25), 8445–8451. https://doi.org/10.1021/acs.langmuir.9b01114.

(144) Hoffman, R. S.; Braga-Mele, R.; Donaldson, K.; Emerick, G.; Henderson, B.; Kahook, M.; Mamalis, N.; Miller, K. M.; Realini, T.; Shorstein, N. H.; Stiverson, R. K.; Wirostko, B. Cataract Surgery and Nonsteroidal Antiinflammatory Drugs. *J. Cataract Refract. Surg.* **2016**, *42* (9), 1368–1379. https://doi.org/10.1016/j.jcrs.2016.06.006.

(145) *What Is the Role of Cyclooxygenase (COX) in the Body?*. GoodRx. https://www.goodrx.com/healthcare-access/medication-education/cyclooxygenase (accessed 2023-02-27).

(146) Blazaki, S.; Tsika, C.; Tzatzarakis, M.; Naoumidi, E.; Tsatsakis, A.; Tsatsanis, C.; Tsilimbaris, M. K. Pharmacokinetics and Efficacy of Intraocular Flurbiprofen. *Graefes Arch.*

Clin. Exp. Ophthalmol. **2017**, *255* (12), 2375–2380. https://doi.org/10.1007/s00417-017-3812-9.

(147) AL Haydar, M.; Abid, H. R.; Sunderland, B.; Wang, S. Metal Organic Frameworks as a Drug Delivery System for Flurbiprofen. *Drug Des. Devel. Ther.* **2017**, *11*, 2685–2695. https://doi.org/10.2147/DDDT.S145716.

(148) Rojas, S.; Colinet, I.; Cunha, D.; Hidalgo, T.; Salles, F.; Serre, C.; Guillou, N.; Horcajada, P. Toward Understanding Drug Incorporation and Delivery from Biocompatible Metal–Organic Frameworks in View of Cutaneous Administration. *ACS Omega.* **2018**, *3* (3), 2994–3003. https://doi.org/10.1021/acsomega.8b00185.

(149) Kim, S.-N.; Park, C. G.; Huh, B. K.; Lee, S. H.; Min, C. H.; Lee, Y. Y.; Kim, Y. K.; Park, K. H.; Choy, Y. B. Metal-Organic Frameworks, NH_2-MIL-88(Fe), as Carriers for Ophthalmic Delivery of Brimonidine. *Acta Biomater.* **2018**, *79*, 344–353. https://doi.org/10.1016/j.actbio.2018.08.023.

(150) Ma, S.; Zhou, H.-C. A Metal−Organic Framework with Entatic Metal Centers Exhibiting High Gas Adsorption Affinity. *J. Am. Chem. Soc.* **2006**, *128* (36), 11734–11735. https://doi.org/10.1021/ja063538z.

(151) Ding, M.; Flaig, R. W.; Jiang, H.-L.; Yaghi, O. M. Carbon Capture and Conversion Using Metal–Organic Frameworks and MOF-Based Materials. *Chem. Soc. Rev.* **2019**, *48* (10), 2783–2828. https://doi.org/10.1039/C8CS00829A.

(152) Zhang, Y.; Fang, F.; Li, L.; Zhang, J. Self-Assembled Organic Nanomaterials for Drug Delivery, Bioimaging, and Cancer Therapy. *ACS Biomater. Sci. Eng.* **2020**, *6* (9), 4816–4833. https://doi.org/10.1021/acsbiomaterials.0c00883.

(153) Khan, A. B.; Mahamana, R.; Pal, E. Review on Mucoadhesive Drug Delivery System: Novel Approaches in Modern Era. *RGUHS J. Pharm. Sci.* **2015**, *4* (4), 128–141. https://doi.org/10.5530/rjps.2014.4.2.

(154) Bayer, I. S. Recent Advances in Mucoadhesive Interface Materials, Mucoadhesion Characterization, and Technologies. *Adv. Mat. Inter.* **2022**, *9* (18), 2200211. https://doi.org/10.1002/admi.202200211.

(155) Wagner, C.E.; Turner, B.S.; Rubenstein, M.; McKinley, G.H.; Ribbeck, K. A Rheological Study of the Association and Dynamics of MUC5AC Gels. *Biomacromolecules*. **2017**, *18* (11), 3654–3664. https://doi.org/10.1021/acs.biomac.7b00809.

(156) Yafout, M.; Ousaid, A.; Khayati, Y.; El Otmani, I. S. Gold Nanoparticles as a Drug Delivery System for Standard Chemotherapeutics: A New Lead for Targeted Pharmacological Cancer Treatments. *Sci. Afr.* **2021**, *11*, e00685. https://doi.org/10.1016/j.sciaf.2020.e00685.

(157) Marino, P. Sustainable Synthesis of Metal–Organic Frameworks for Applications in Ophthalmic Drug Delivery. M.S. Thesis, Concordia University, Montreal, QC, 2021. https://spectrum.library.concordia.ca/id/eprint/990140/ (accessed 2023-06-15).

(158) Gold Biotechnology, Ellman's Test Protocol. https://www.goldbio.com/documents/2359/Ellmans+Test+Protocol.pdf (accessed on 2023-04-21).

(159) Wang, S.; Morris, W.; Liu, Y.; McGuirk, C. M.; Zhou, Y.; Hupp, J. T.; Farha, O. K.; Mirkin, C. A. Surface-Specific Functionalization of Nanoscale Metal–Organic Frameworks. *Angew. Chem. Int. Edit.* **2015**, *54* (49), 14738–14742. https://doi.org/10.1002/anie.201506888.

(160) Diring, S.; Furukawa, S.; Takashima, Y.; Tsuruoka, T.; Kitagawa, S. Controlled Multiscale Synthesis of Porous Coordination Polymer in Nano/Micro Regimes. *Chem. Mater.* **2010**, *22* (16), 4531–4538. https://doi.org/10.1021/cm101778g.

(161) Niklas. *Particle Size of Metal-Organic Frameworks: Is it size that matters?* https://blog.novomof.com/blog/particle-size-of-metal-organic-frameworks (accessed 2023-04-11).

(162) Hou, J.; Sapnik, A. F.; Bennett, T. D. Metal–Organic Framework Gels and Monoliths. *Chem. Sci.* **2020**, *11* (2), 310–323. https://doi.org/10.1039/C9SC04961D.

(163) SITNFlash. *Biological Roles of Water: Why is water necessary for life?*. Science in the News. https://sitn.hms.harvard.edu/uncategorized/2019/biological-roles-of-water-why-is-water-necessary-for-life/ (accessed 2023-06-17).

(164) Fang, Z.; Bueken, B.; De Vos, D. E.; Fischer, R. A. Defect-Engineered Metal–Organic Frameworks. *Angew. Chem. Int. Edit.* **2015**, *54* (25), 7234–7254. https://doi.org/10.1002/anie.201411540.

(165) Ploetz, E.; Engelke, H.; Lächelt, U.; Wuttke, S. The Chemistry of Reticular Framework Nanoparticles: MOF, ZIF, and COF Materials. *Adv. Funct. Mater.* **2020**, *30* (41), 1909062. https://doi.org/10.1002/adfm.201909062.

(166) Yang, D.; Gaggioli, C. A.; Ray, D.; Babucci, M.; Gagliardi, L.; Gates, B. C. Tuning Catalytic Sites on Zr_6O_8 Metal-Organic Framework Nodes via Ligand and Defect Chemistry Probed with Tert-Butyl Alcohol Dehydration to Isobutylene. *J. Am. Chem. Soc.* **2020**, *142* (17), 8044–8056. https://doi.org/10.1021/jacs.0c03175.

(167) Cirujano, F.G.; Xamena, F.X.L. Tuning the Catalytic Properties of UiO-66 Metal–Organic Frameworks: From Lewis to Defect-Induced Brønsted Acidity. *J. Phys. Chem. Lett*. **2020**, *11* (12), 4879–4890. https://doi.org/10.1021/acs.jpclett.0c00.

(168) Li, P.; Modica, J. A.; Howarth, A. J.; Vargas L., E.; Moghadam, P. Z.; Snurr, R. Q.; Mrksich, M.; Hupp, J. T.; Farha, O. K. Toward Design Rules for Enzyme Immobilization in Hierarchical Mesoporous Metal-Organic Frameworks. *Chem.* **2016**, *1* (1), 154–169. https://doi.org/10.1016/j.chempr.2016.05.001.

(169) Shastri, D.; Shelat, P.; Shukla, A.; Patel, P. Ophthalmic Drug Delivery System: Challenges and Approaches. *Syst. Rev. Pharm.* **2010**, *1* (2), 113. https://doi.org/10.4103/0975-8453.75042.

(170) He, S.; Wu, L.; Li, X.; Sun, H.; Xiong, T.; Liu, J.; Huang, C.; Xu, H.; Sun, H.; Chen, W.; Gref, R.; Zhang, J. Metal-organic frameworks for advanced drug delivery. *Acta Pharm. Sinic. B*. **2021**, *11* (8), 2362–2395. https://doi.org/10.1016/j.apsb.2021.03.019.

(171) Chowdhury, S.; Sharma, P.; Rathi, P.; Siril, P. F. Direct One-Pot Synthesis of Highly Tunable Mixed-Linker UiO-66-(SH)2 Metal-Organic Frameworks: Enroute Toward Robust Sulfonic Acid Tagged UiO-66 Architectures; preprint; Chem. **2022**. https://doi.org/10.26434/chemrxiv-2022-35rk2.

(172) Moon, S.; Tanaka, S.; Sekino, T. Crystal Growth of Thiol-Stabilized Gold Nanoparticles by Heat-Induced Coalescence. *Nanoscale Res. Lett.* **2010**, *5* (5), 813. https://doi.org/10.1007/s11671-010-9565-6.

Appendix

a)

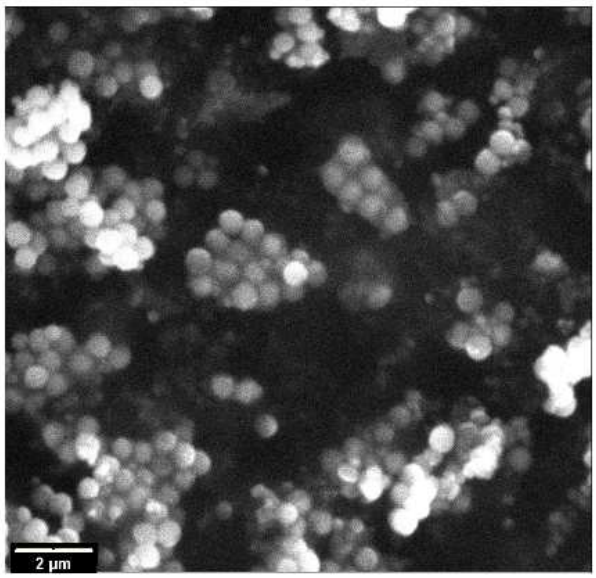

b)

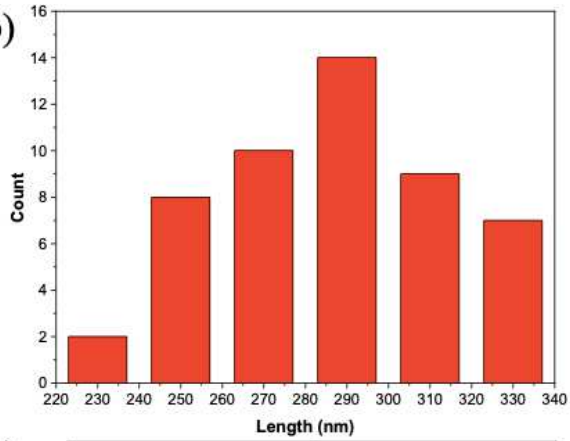

c)

N total	50
Mean (nm)	286
Stand. Dev.	28
Min. (nm)	220
Max. (nm)	337

d)

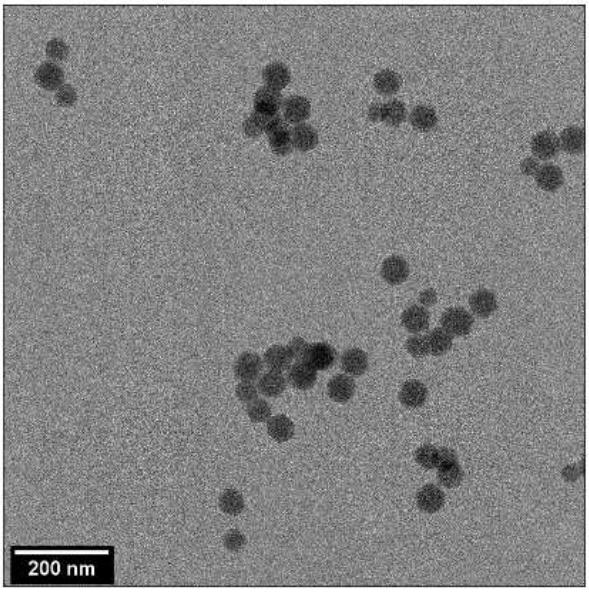

e)

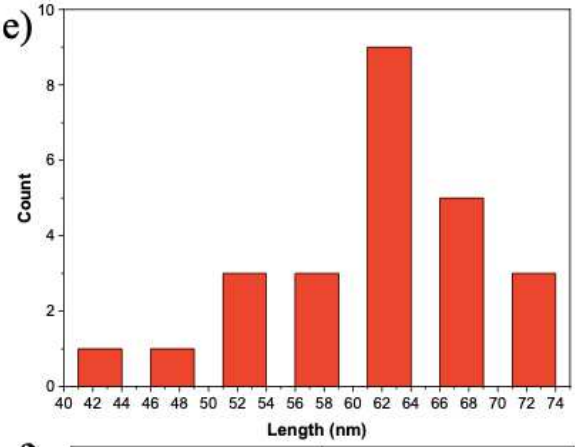

f)

N total	25
Mean (nm)	62
Stand. Dev.	8
Min. (nm)	41
Max. (nm)	73

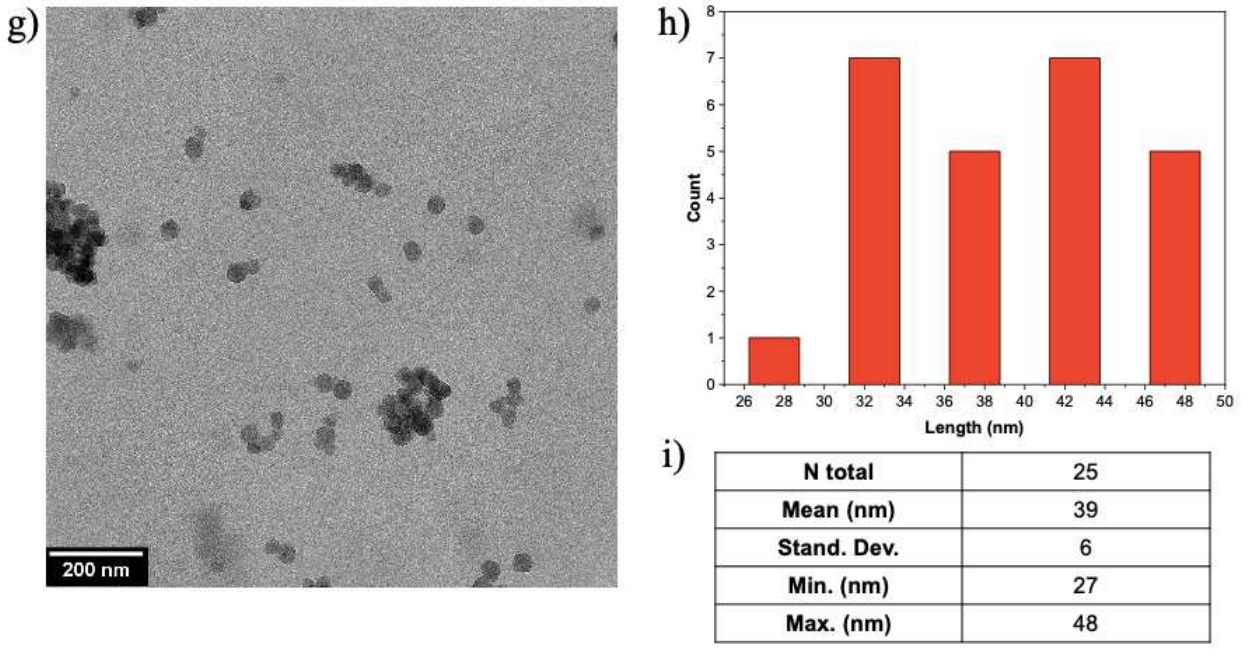

N total	25
Mean (nm)	39
Stand. Dev.	6
Min. (nm)	27
Max. (nm)	48

Figure A.1. Particle size analysis represented by; a), d), g) optical micrographs, b), e), h) statistical analyses of particle size distribution represented by histograms, and c), f), i) table of particle size statistics for MOF-808, UiO-66, and UiO-67, respectively.

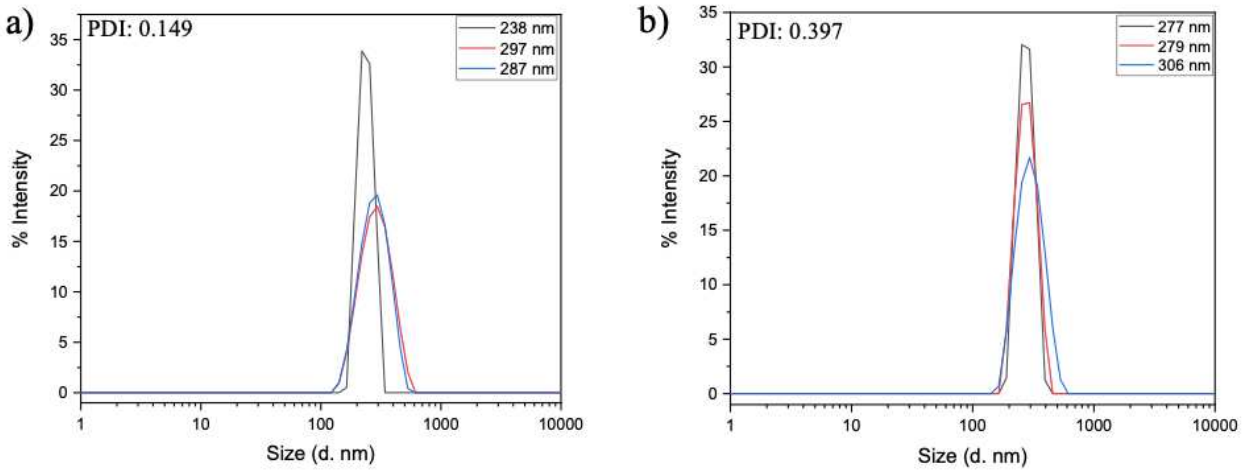

Figure A.2. DLS measurements for MOF-808 post SALI synthesis with a) thioglycolic acid and an average particle size of 274 nm, and b) mercaptoundecanoic acid and an average particle size of 287 nm.

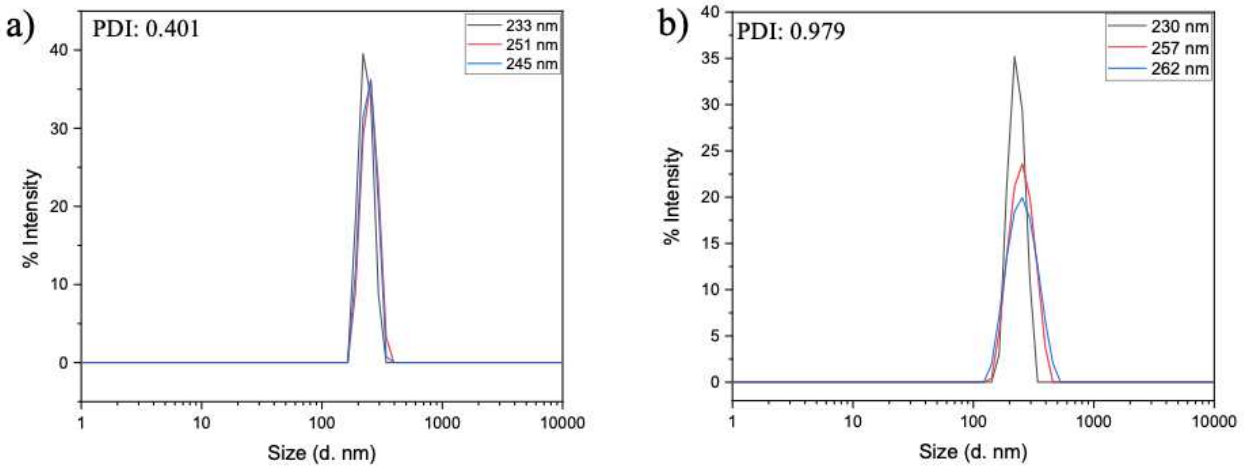

Figure A.3. DLS measurements for UiO-66 post SALI synthesis with a) thioglycolic acid and an average particle size of 243 nm, and b) mercaptoundecanoic acid and an average particle size of 250 nm.

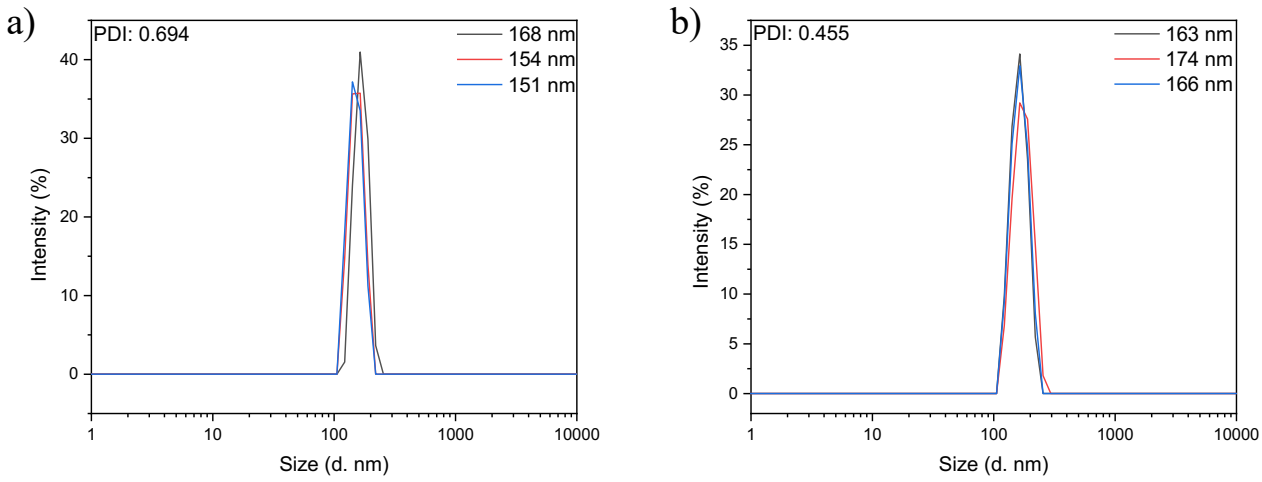

Figure A.4. DLS measurements for UiO-67 post SALI synthesis with a) thioglycolic acid and an average particle size of 158 nm, and b) mercaptoundecanoic acid and an average particle size of 168 nm.

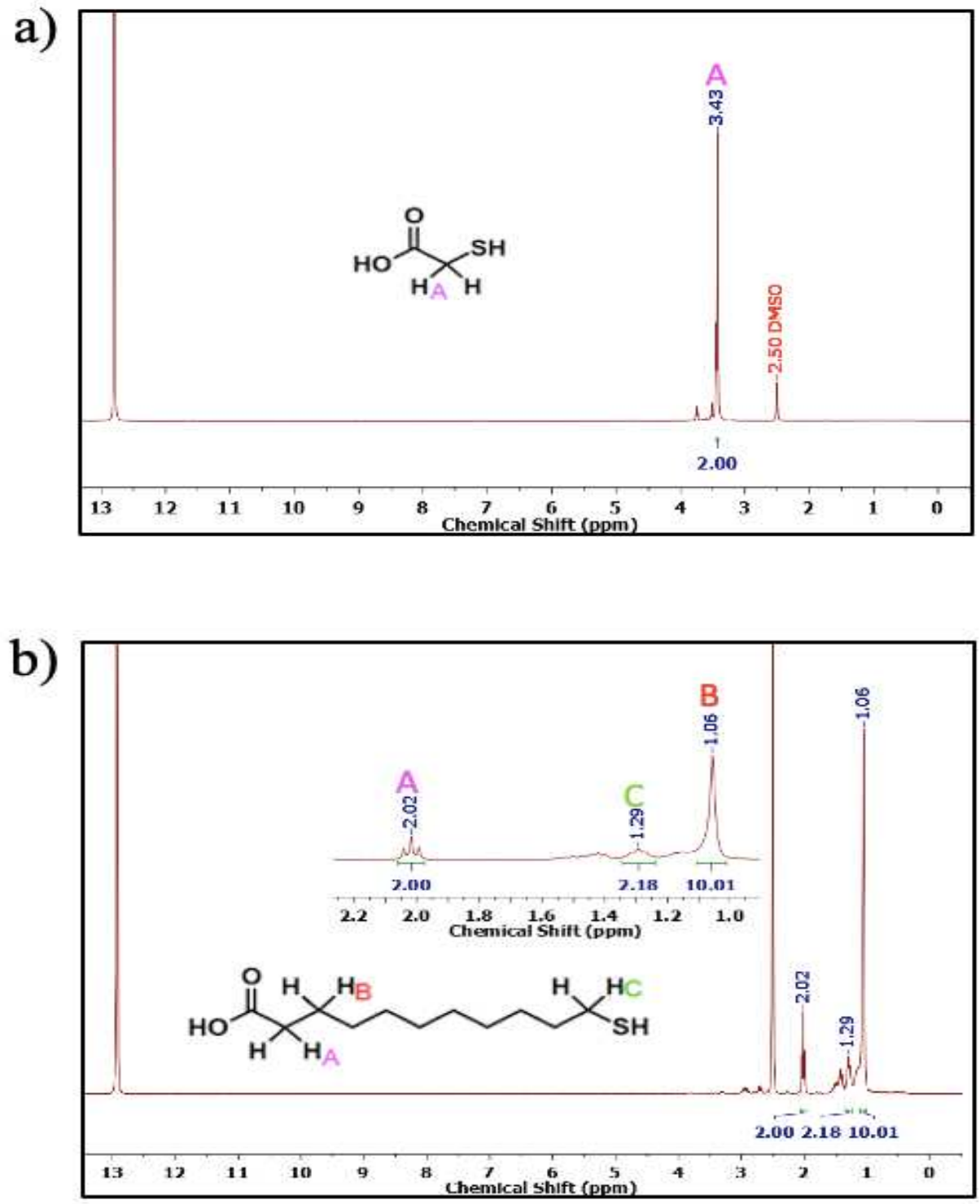

Figure A.5. ^{1}H-NMR spectra of a) thioglycolic acid and b) mercaptoundecanoic acid digested in 6 drops of deuterated sulfuric acid (D_2SO_4), and 600 μL of dimethyl sulfoxide (DMSO-d_6).

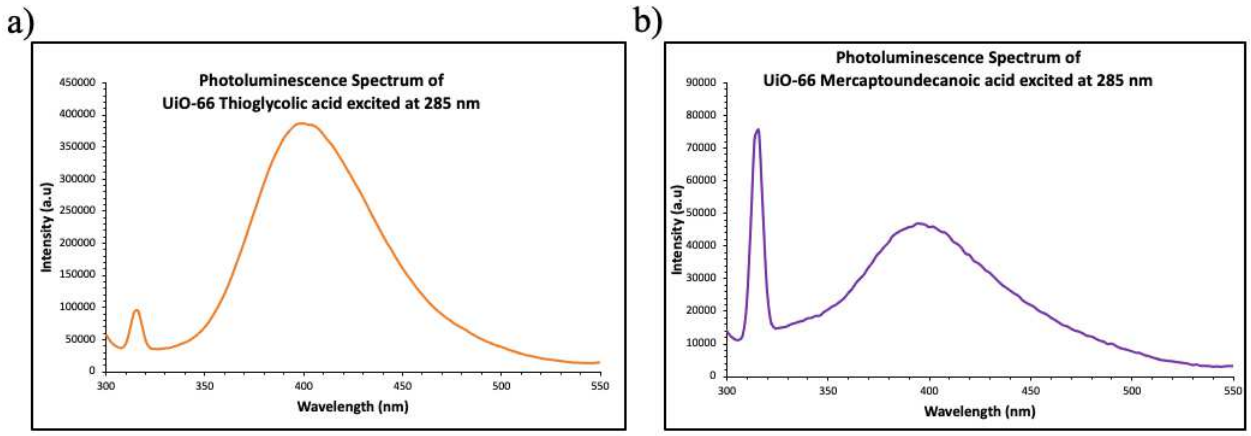

Figure A.6. Photoluminescence spectrum of UiO-66 with a) thioglycolic acid and b) mercaptoundecanoic acid excited both at 285 nm. 1.0 mg of each sample was incubated in MQ H_2O for 2 h prior to analysis.

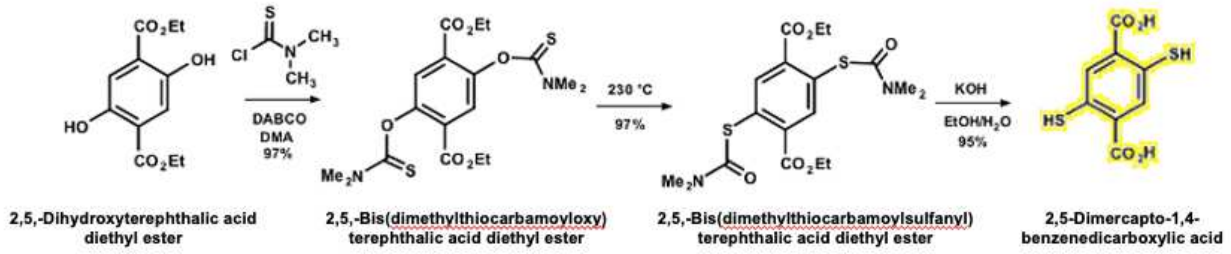

Figure A.7. Reaction Scheme for the synthesis of 2,5-Dimercapto-1,4-benzenedicarboxylic acid (H_2DMBD).

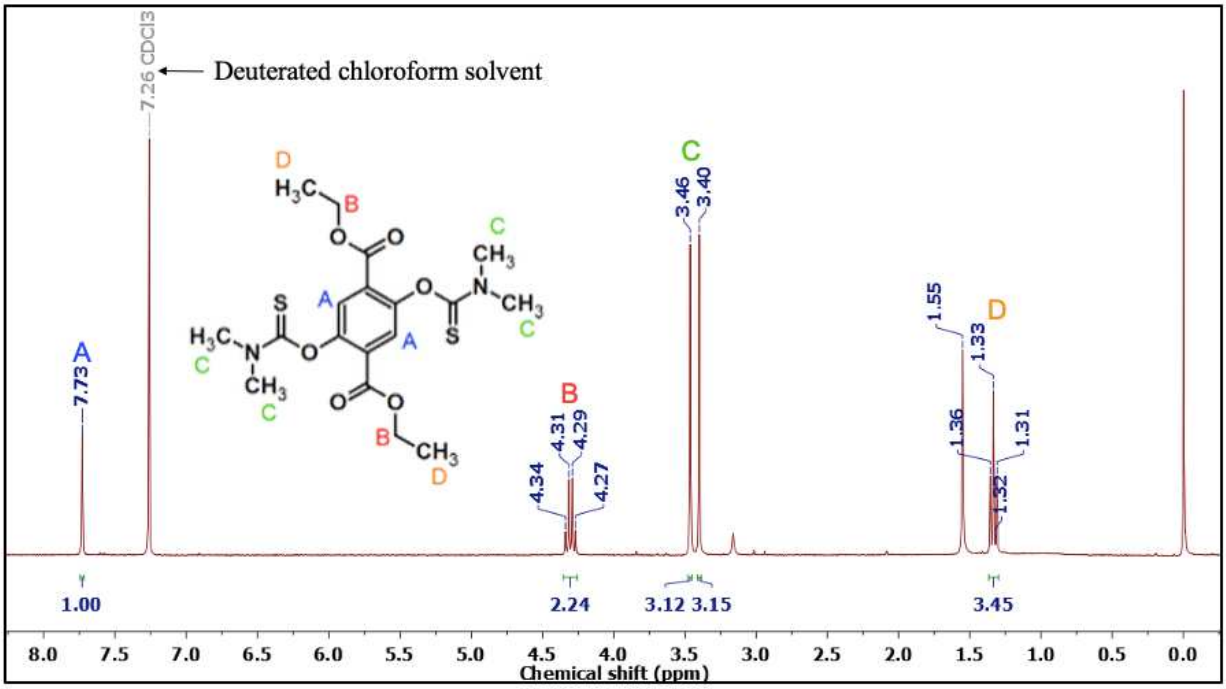

Figure A.8. [1]H-NMR spectra of 2,5-Bis(dimethylthiocarbamoyloxy)terephthalic acid diethyl ester in deuterated chloroform.

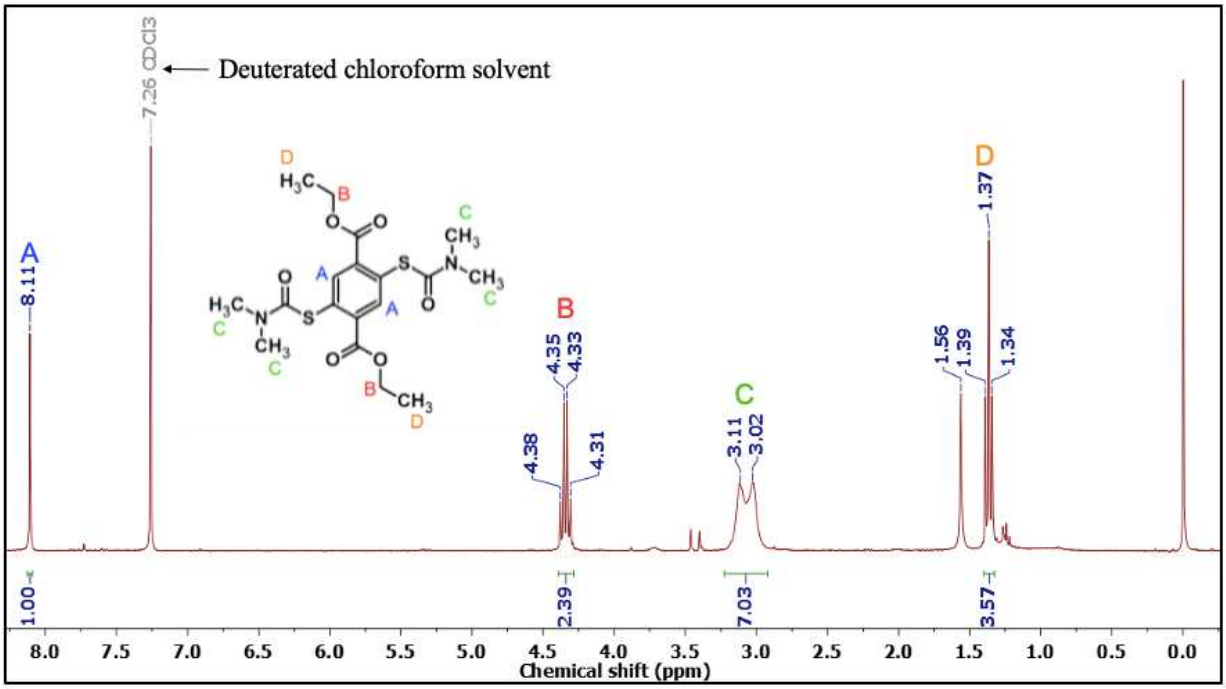

Figure A.9. [1]H-NMR spectra of 2,5-bis(dimethylthiocarbamoylsulfanyl)terephthalic acid diethyl ester in deuterated chloroform.

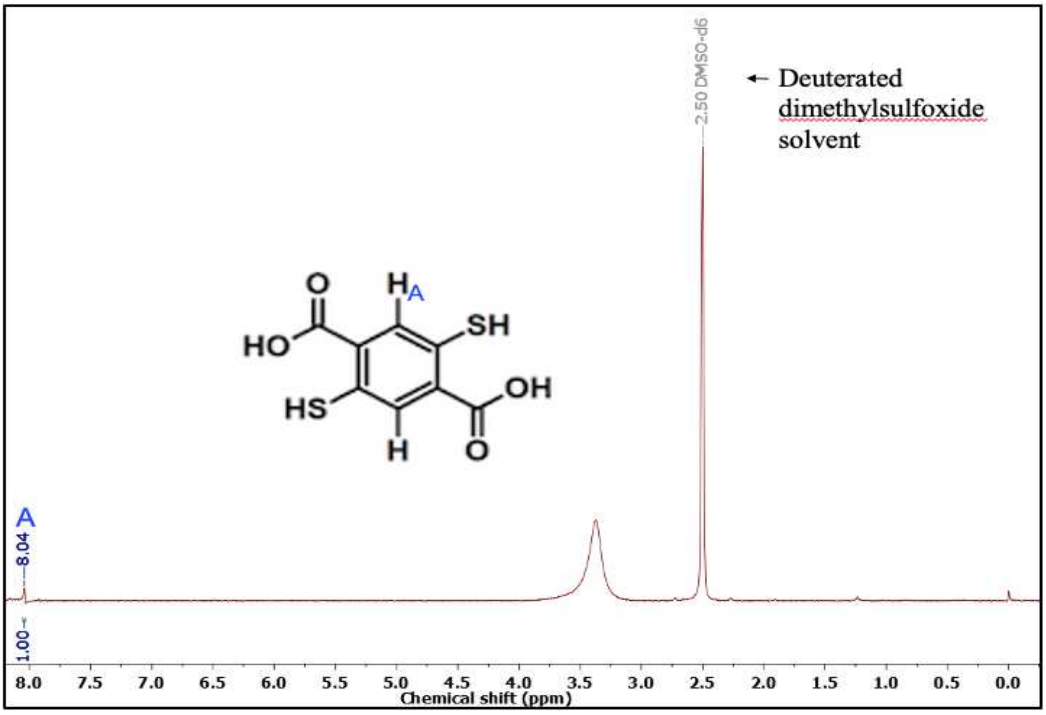

Figure A.10. ^{1}H-NMR spectra of 2,5-dimercaptoterephthalic acid in deuterated dimethylsulfoxide.

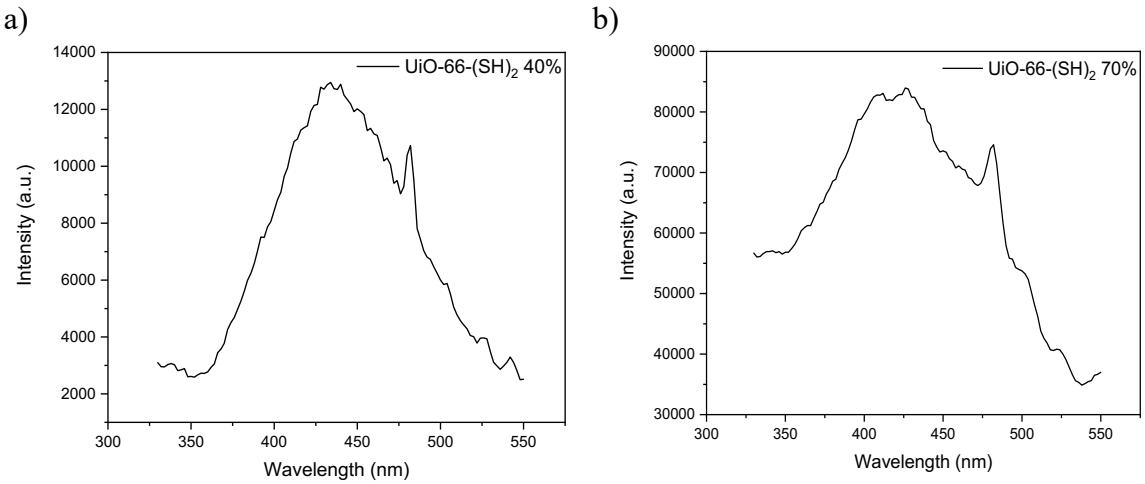

c)

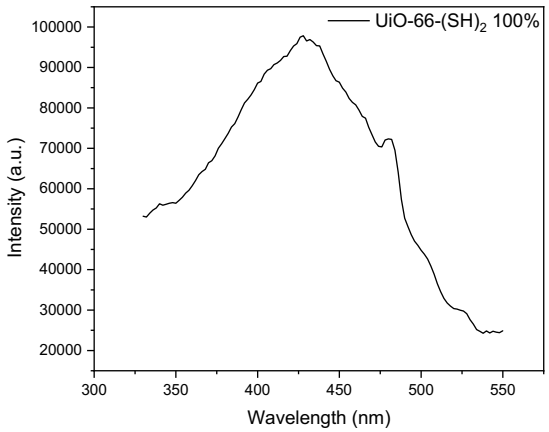

Figure A.11. Photoluminescence spectrum of mixed thiolated UiO-66-$(SH)_2$ for a) 40%, b) 70%, and c) 100%.